UNIVERSIDADE DE SÃO PAULO

ESCOLA POLITECNICA

JAVIER ALBERTO GUALDRON PLATA

Experimental Procedure To Evaluate Fatigue Crack Growth of Short Cracks in Girth Welds of Clad Line Pipes

SÃO PAULO

2024

JAVIER ALBERTO GUALDRON PLATA

Experimental Procedure To Evaluate Fatigue Crack Growth of Short Cracks in Girth Welds of Clad Line Pipes

Versão Corrigida

Tese apresentada à Escola Politécnica da Universidade de São Paulo para obtenção do título de Doutor em Ciências.

Área de Concentração: Engenharia Naval e Oceânica.

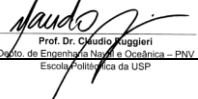Orientador: Prof. Dr. Claudio Ruggieri

São Paulo

2024

Este exemplar foi revisado e corrigido em relação à versão original, sob responsabilidade única do autor e com a anuência de seu orientador.

São Paulo, 27 de Junho de 2024

Assinatura do autor:

Assinatura do orientador:

Prof. Dr. Cláudio Ruggieri
Depto. de Engenharia Naval e Oceânica – PNV
Escola Politécnica da USP

Catalogação-na-publicação

ACKNOWLEDGEMENTS

RESUMO

Este trabalho aborda um procedimento mais elaborado de teste para mitigar os efeitos de fechamento de trinca sobre os valores experimentais do limiar de crecimento de trincas por fadiga, ΔK_{th}, baseado na técnica de pré-trincamento por carga de compressão. O método da pré-trinca por compressão induz tensões residuais de tração na região próxima à trinca, possibilitando, portanto, a obtenção de valores consistentes e confiáveis de ΔK_{th} concomitantemente a um melhor comportamento experimental da propagação cíclica da trinca. Um programa experimental abrangente sobre um aço inoxidável AISI 316L comparou diferentes técnicas de pré-trincamento por meio de testes de crescimento de trinca por fadiga (FCG). Foram testados corpos de prova padrão C(T) e corpos de prova SE(B) sob flexão de três pontos, ambos com razão tamanho da trinca sobre largura do corpos de prova, a/W=0.2. Adicionalmente, as geometrias SE(B) possuiam razões entre a distância entre apoios e largura, S/W = 4 e 8. Os resultados demonstram que a combinação da pré-trinca por compressão com corpos de prova de flexão 3P com S/W=8 melhora significativamente os dados da taxa de crescimento de trinca por fadiga próximo ao limiar para o aço AISI 316L, o que possibilita a determinação precisa de ΔK_{th}. Em sequência a estas estudos, as metodologias de pré-compressão são aplicadas em juntas soldadas de INCONEL 625 de tubos revestidos e cladeados, comprovando a versatilidade e relevância. Em conclusão, esta abordagem pioneira proporciona uma melhoria significativa para a avaliação dos valores experimentais do limiar de crecimento de trincas por fadiga, ΔK_{th}, avançando o conhecimento das falhas por fadiga a partir de pequenas imperfeições em materiais e componentes. Ela introduz um procedimento inovador para induzir tensões residuais benéficas nas pontas das trincas. Corpos de prova entalhados com aumento significativo em conjunto com pré-trincação por compressão melhoram substancialmente os dados de taxa de crescimento de trincas próximas ao limiar. As técnicas são versáteis para materiais uniformes e soldados. Ao avançar sobre a compreensão fundamental dos comportamentos das trincas, esta pesquisa possibilita uma melhor identificação de riscos provenientes de imperfeições inerentes e o desenvolvimento de estratégias de mitigação. Os métodos experimentais e resultados obtidos neste trabalho contribuem significativamente para os campos de ciência dos materiais e integridade estrutural.

Palavras-chave: Ensaios de fadiga, Crescimento de trincas por fadiga, Limiar de fadiga , Pré-trinca por compressão, Aço Inoxidável, Junda Soldada Inconel 625.

ABSTRACT

This work presents an elaborate testing procedure to mitigate the effects of crack closure on the experimental determination of the fatigue crack growth threshold, ΔK_{th}, based on the compression pre-cracking technique. The compression pre-cracking method induces beneficial residual tensile stresses near the crack tip region, enabling consistent and reliable ΔK_{th} values to be obtained, along with improved experimental behavior of cyclic crack propagation. An extensive experimental program was conducted on AISI 316L stainless steel, comparing different pre-cracking techniques through fatigue crack growth (FCG) tests. Standard C(T) specimens and three-point bend SE(B) specimens were tested, both with a crack length-to-width ratio, a/W=0.2. Additionally, the SE(B) geometries had span-to-width ratios, S/W = 4 and 8. The results demonstrate that the combination of compression pre-cracking with 3P bend specimens having S/W=8 significantly enhances the near-threshold fatigue crack growth rate data for AISI 316L steel, enabling accurate determination of ΔK_{th}. Following these studies, the compression pre-cracking methodologies were applied to girth-welded joints of clad and lined INCONEL 625 pipes, proving their versatility and relevance. In conclusion, this pioneering approach provides a significant improvement in the evaluation of experimental fatigue crack growth threshold values, ΔK_{th}, advancing the understanding of fatigue failures originating from small imperfections in materials and components. It introduces an innovative procedure to induce beneficial residual stresses at crack tips. Deeply notched specimens combined with compression pre-cracking substantially improve the near-threshold crack growth rate data. The techniques are versatile for both uniform and welded materials. By advancing the fundamental understanding of crack behaviors, this research enables better identification of risks arising from inherent imperfections and the development of mitigation strategies. The experimental methods and results obtained in this work contribute significantly to the field.

Keywords: Fatigue testing, Fatigue crack growth, Fatigue threshold, Compression pre-cracking, Stainless steel, Inconel 625 Girth Weld.

LIST OF FIGURES

LIST OF TABLES

CONTENTS

CHAPTER 1

1. INTRODUCTION

1.1. Introduction

This chapter serves as an introductory section to the fatigue assessment issue, with a particular emphasis on fatigue crack propagation. It elucidates the underlying reasons driving the present research, outlines its objectives and delineates potential areas of application. Furthermore, it provides an overview of the key themes that will be explored in-depth throughout this thesis.

The increasing demands for energy, transportation and other natural resources have influenced the design and operation of engineering structures, resulting in stricter safety margins, extended inspection intervals and prolonged repair schedules. In recent decades, several catastrophic accidents have highlighted the critical nature of the fatigue problem in modern society, as depicted in Fig. 1(a) and (b). The underlying cause of these damages and failures is the gradual propagation of cracks during cyclic loading. These cracks or defects may have been present in the components before undergoing cyclic loading (manufacturing defects) or could have emerged during service. When cyclic crack growth occurs, it can ultimately lead to structural collapse if the stresses on the remaining structure exceed the tensile strength of the material, resulting in an unstable crack propagation. One of the most well-known examples of fatigue failure in offshore platforms occurred in the North Sea in March 1980 when the Alexander L. Kielland platform collapsed and sank following the rupture of one of its tubular columns [1]. The tragedy, which resulted in the loss of 123 lives, commenced with the fatigue-induced propagation of pre-existing defects in a welded joint that linked a hydrophone to one of the tubular beams connecting the primary columns of the structure.

The repercussions and expenses associated with the untimely catastrophic failure of structures and components underscore the necessity for a rational and realistic analysis of structural fatigue. Such an assessment is of paramount importance to ensure the mechanical integrity of structural components. The selection of suitable materials for each engineering application typically involves a comparison of mechanical properties, including tensile strength, corrosion resistance, fracture toughness and fatigue, among others, of the candidate materials under consideration.

Among these properties, the fatigue crack propagation threshold, ΔK_{th}, plays a critical role in accurately predicting the fatigue life of components.

Fatigue crack growth in a material is typically assessed by considering the size of the crack and its propagation rate, denoted as da/dN. The rate at which a crack extends through a specific material is expressed as a function of the linear-elastic fracture mechanics parameter, ΔK, which represents the stress intensity factor range. This relationship was initially demonstrated to exhibit linearity over a substantial range of fatigue crack growth rates when plotted on a log-log scale [2]

The primary issue that needs to be tackled is directly related to the process of deploying and installing subsea pipelines through the reeling method. This method enables the welding and inspection of circumferential welded joints to take place in onshore manufacturing facilities [3], [4].

a   b

Figure 1: (a) Catastrophic wind turbine failure caused by propagation of a fatigue weld defect. (b) Accident on an oil platform caused by fatigue of the welded joint of one of its primary structural elements.

Within the context of the structural integrity of lined pipes with an internal CRA (Corrosion Resistant Alloy) layer, the most critical region in the process is the circumferential joint region created by welding, often referred to as the girth weld. This girth weld, specifically at the point where the weld reinforcement meets the base metal (referred to as Point A in Figure 2), is the preferred location for the initiation of fatigue cracks.

If the reinforcement is removed and properly finished, the potential point for fatigue crack initiation shifts to the interface between the weld root reinforcement and the filler layer.

However, the industry has grown increasingly concerned about fatigue failures that originate in the transition area from the line to the infill layer (Points C and D in Figure 2). Point C is particularly critical because it represents the transition between three different materials and its position makes it challenging to achieve an adequate finish to prevent crack initiation. Relatively large defects can be detected using non-destructive techniques and can be rectified before installation. Nevertheless, it's essential to assess the implications of naturally occurring crack nucleation and their propagation under cyclic loading conditions in this specific configuration.
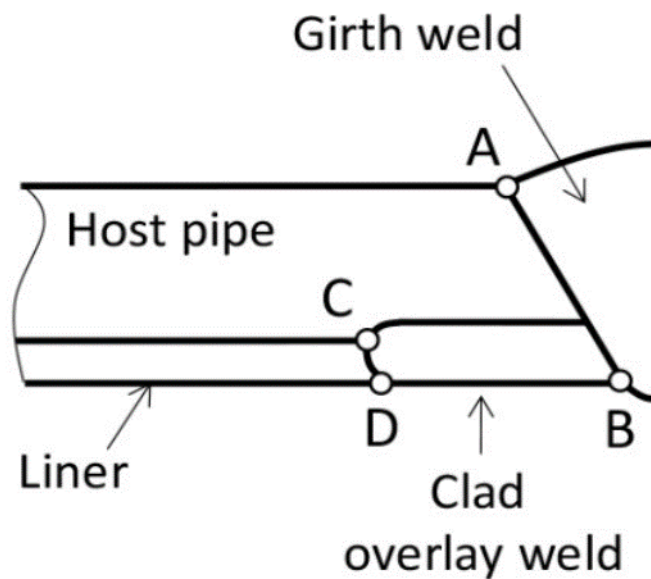
Figure 2: Illustration of a typical girth weld on lined pipes. [3]

Typical welding processes involve significant thermal cycling and induce non-uniform residual stresses in the weld metal and surrounding areas, including the heat-affected zone (HAZ). These effects often lead to a degradation in metallurgical quality and have the potential to reduce the fatigue life of the welded joint when compared to the base metal material [3].

As a result, inadequate fatigue performance of a welded joint significantly increases the risk of failure, primarily due to the propagation of undetected weld defects during routine inspections. Experimental observations consistently show the presence of various crack-like defects in the girth weld. These defects can take the form of planar configurations, such as hot and cold cracks, lack of penetration and undercuts, or volumetric defects like porosities and slag inclusions [4], [5]. This occurs even when

good construction practices and appropriate welding procedures and consumables are employed.

In fact, a review of the history of in-service failures of welded structural components over the past few decades, including the examples depicted in previous Figure 1, unmistakably demonstrates that the fatigue propagation of pre-existing defects is a major contributor to catastrophic failures in welded metal structures [6].

While the microstructural mechanisms associated with the propagation of fatigue cracks are not fully understood [7], some simplified methodologies based on fracture mechanics concepts have been well-established for analyzing this failure mode. In particular, the Paris model [5], [6], [7], [8], [9] allows for the introduction of a power relationship between the crack growth rate and the number of cycles, da/dN and the cyclic amplitude of the stress intensity factor, ΔK, in the form $da/dN = C(\Delta K)^m$. Here, C and m are constants that depend on the material and propagation conditions [7], [8] and they are typically determined through experimental tests conducted on standardized specimens containing long cracks (typically ranging from 10 to 40 mm in specimens of typical dimensions).

The Paris model has emerged as one of the most widely used approaches for engineering fatigue life analysis of structural components that contain pre-existing defects due to its simplicity and relative robustness [6], [7]. However, with a few exceptions or in cases of advanced degradation, most structural defects are superficial, extending only a few millimeters (or even fractions of millimeters) in depth. In such cases, numerous investigations, and experimental observations (as documented, for instance, by Suresh [7] indicate that the propagation rate of short cracks can be significantly higher than that of longer cracks when characterized in terms of the same stress intensity factor (ΔK). Consequently, directly applying fatigue curves da/dN obtained from conventional tests e.g., ASTM E647 [2] to assess the fatigue life of structural components with small pre-existing defects can lead to potentially significant overestimations of their remaining life, which could be unsafe.

Therefore, advanced, or more realistic methodologies for evaluating defect propagation under fatigue in structural components, particularly in welded joints, need to account for the influence of short crack behavior on the propagation rate and on the experimental da/dN curves.

1.2. Objectives

The primary objective of this research is twofold: first, to investigate and develop a specialized test procedure for inducing pre-cracks through compression loading, and second, to evaluate the fatigue threshold behavior within Region I, with a specific emphasis on AISI 316L stainless steel. Furthermore, the application of this methodology is extended to welded joints, specifically those fabricated with INCONEL 625 and extracted from cladded pipes. This will be accomplished by:

- Establishing an experimental program to refine a specialized compression pre-cracking test procedure employing Single Edge Bending (SEB) specimens to improve consistency.
- Determining Region I fatigue thresholds and applying findings to girth weld CRA pipelines for validation.
- Comparing results to prevalent ASTM E647 standards to identify methodology improvements.

The secondary objectives are:

- Generate a comprehensive fatigue crack growth test database tailored to oil and gas industry needs and share publicly to enable broader scientific advancement.
- Incorporate an innovative Compression Pre-Cracking Load Reduction (CPLR) technique into testing protocols to contribute to industry best practices.
- Disseminate valuable fatigue failure knowledge to the research community by disclosing refined experimental procedures and datasets.

In summary, this research aims to progress fatigue evaluation methods for a key oil industry structure by developing targeted datasets, improving technical procedures and freely disseminating the outcomes to benefit both real-world practices and fundamental research.

CHAPTER 2

2. LITERATURE REVIEW

2.1. Introduction

This chapter provides a review fatigue life concepts considering crack closure effects, with a focus on works studying homogeneous materials and plasticity-induced closure. The main advantages and disadvantages of prevalent methodological approaches are discussed. Key points covered include the impact of crack clousure on fatigue thresholds, the role of residual stresses, limitations of current standards and the need for improved consistency in measuring near-threshold growth rates. Refining testing procedures to address closure mechanics can ultimately enhance fatigue life predictions and risk assessments.

2.2. Structural integrity of the Oil and Gas production infrastructure

The structural integrity of the oil and gas production infrastructure is a critical aspect of the energy industry. It refers to the ability of various components, such as pipelines, drilling rigs, offshore platforms and storage facilities, to withstand operational stresses, environmental factors and potential hazards while maintaining safe and reliable operation over their intended lifespan.

Ensuring the structural integrity of these facilities is of paramount importance for several reasons. First, the oil and gas industry operates in challenging environments, including harsh weather conditions, corrosive substances and high-pressure systems. Any structural failure can lead to catastrophic consequences, including oil spills, gas leaks and environmental disasters. Secondly, these infrastructures are capital-intensive and have long service lives, often spanning several decades. Ensuring their integrity is essential for optimizing the return on investment and minimizing costly repairs or replacements.

To achieve structural integrity, rigorous engineering standards, regular inspections and maintenance protocols are employed. Advanced materials, corrosion-resistant coatings and cutting-edge monitoring technologies are utilized to prevent degradation and detect potential issues early. In summary, the structural integrity of oil and gas production infrastructure is a fundamental concern that encompasses safety, environmental protection and economic viability in the energy sector. It involves a multidisciplinary approach to design, construction, maintenance and monitoring to ensure the continued reliability and sustainability of these critical assets.

2.3. Clad Pipes (Bimetallic)

Clad pipes are known for combining the characteristics of mechanical strength, toughness and cost-effectiveness of carbon steels with the corrosion resistance of high-alloy materials, such as corrosion-resistant alloys. Pipes manufactured from clad materials meet requirements for durability, corrosion resistance and cost-efficiency. Their use is recommended in all areas where dynamic stresses, high pressures and aggressive transported media prevail [2].

The variety of available clad products allows for an entire project to be developed using clad steel through appropriate methods, ranging from reservoirs to export lines, including production pipelines, wellhead equipment, valves, transport lines, vessel piping and heat exchangers [10]. This results in effective and long-lasting performance in challenging industrial environments.

There are successful applications worldwide and extensive experience has been gained with the welding of clad steels [10]. One notable example is found in offshore projects, where the use of lighter products provides advantages to the facilities. The use of base metals with superior mechanical strengths compared to solid CRA allows for a reduction in the wall thickness of equipment and pipelines, consequently reducing the weight of these components and resulting in economic benefits.

To address the escalating global energy demand, there has been a notable surge in oil and gas exploration in fields characterized by elevated water content, H_2S, CO_2, as well as high pressures and temperatures as seen in Figure 3. Consequently, an increasingly prominent focus has emerged on the development of corrosion-resistant solutions. These solutions are essential for ensuring the long-term, dependable transportation of these resources while simultaneously upholding environmental preservation and cost-efficiency goals [11].

One pertinent example of this endeavor is the application of clad pipes in constructing Steel Catenary Risers (SCRs) meticulously engineered for deep-water environments. In such challenging settings marked by dynamic loads and elevated temperatures, these tubes play a pivotal role. They must demonstrate not only fatigue resistance but also exceptional mechanical properties and a robust resistance to corrosion, ensuring the integrity and longevity of critical infrastructure components [2].
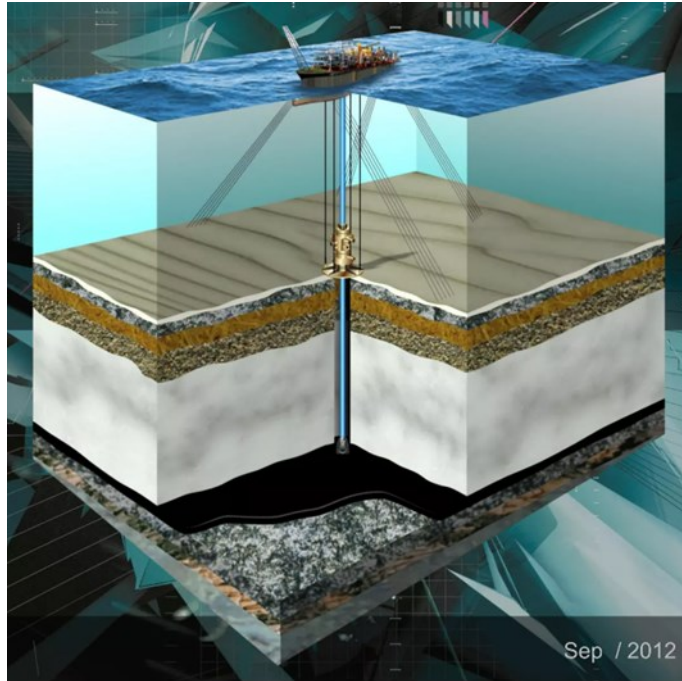
Figure 3: Presalt key structural Integrity issues [12].

2.3.1. Mechanically Clad Pipes (Lined Pipes)

Mechanically clad pipes are defined in the DNV OS F101 standard (2013) [13] as pipes with an inner lining (corrosion-resistant) where the connection between the base metal and the lining material is mechanical [10]. Clad pipes are defined as those that do not have a metallurgical bond between the liner and the base metal, except in small areas at the ends of the pipe or along its length describes them as double-walled pipes in which carbon steel provides structural capacity while a corrosion-resistant lining is placed inside the outer pipe, separating the outer pipe from direct contact with the corrosive product to be transported [14]. This lining provides corrosion protection.

To achieve a mechanical connection between the base metal and the corrosion-resistant alloy (CRA), there are two main manufacturing methods: expanded lined through hydraulic or thermohydraulic expansion and explosively lined [10]. As highlighted by Heigl G [15] the primary difference between the two lies in the magnitude of the bonding forces achieved between the CRA layer and the base metal as see in Figure 4.

Typical applications include straight pipes, pipelines and cold-formed sections. They are generally not used for top connections, likely due to concerns regarding the cutting and welding of sections of the pipes along their length [16] In cases where

circumferential welds are required, similar techniques to those used for repairing welds in pipelines are necessary. Additionally, there is a concern related to the potential collapse of the pipeline, either due to hydrogen permeation that may accumulate at the interface or due to differences in thermal expansion between the materials, especially when operating at high temperatures [16].
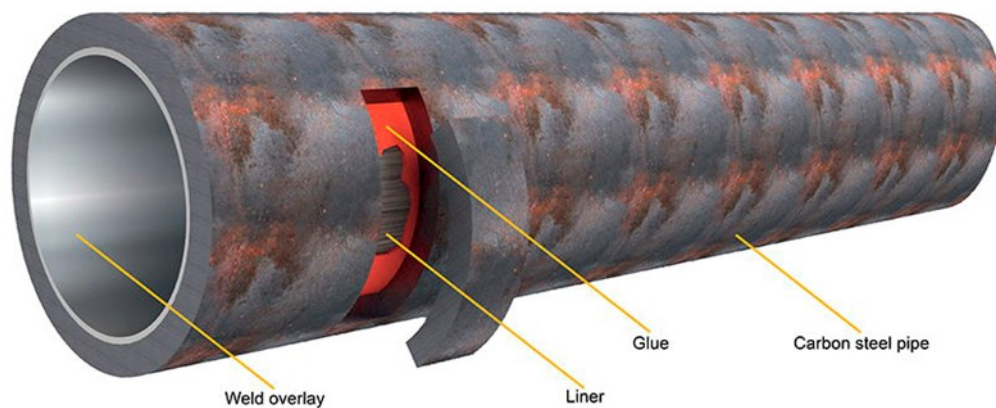
Figure 4: Mechanically Clad Line Pipe (adapted TWI) [17].

2.4. Triple-point failure

At the triple-point between the liner, weld overlay and carbon steel pipe, cracks may initiate from fabrication flaws and grow during installation or operation, posing significant structural integrity concerns. These cracks can compromise the integrity of the entire system, potentially leading to leaks, environmental hazards and costly maintenance or repair efforts. Therefore, meticulous inspection and quality control measures are essential during the fabrication and installation processes to detect and address any flaws or defects promptly. Additionally, ongoing monitoring and maintenance are critical to identifying and mitigating crack propagation and ensuring the long-term reliability of the pipeline or structure. This proactive approach helps prevent potential catastrophic failures and ensures the safe and efficient transportation of fluids or gases [18].
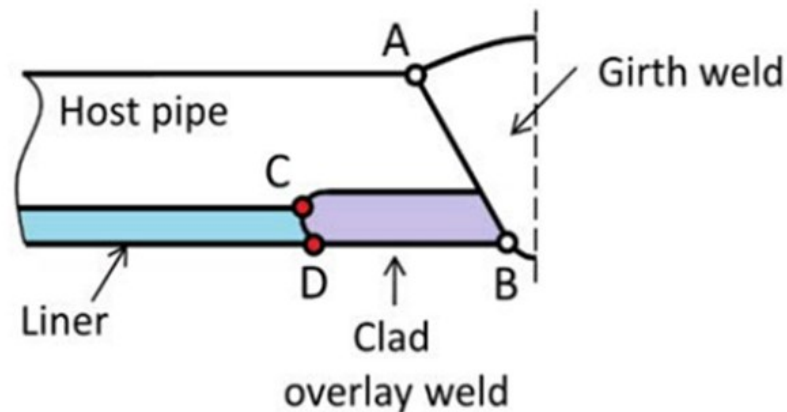
Figure 5: Potential fatigue crack initiation points in a mechanically clad pipe [17], [19].

The girth weld process is intricate due to several involved steps. Initially, a filler weld is performed using an additive metal that matches the same alloy as the inner liner (clad overlay weld). Subsequently, the pipes are joined through a top weld using corrosion-resistant metal as the girth weld. During the winding and unwinding process, the outer layer of the pipe is subjected to higher levels of stress compared to the inner layer.

Consequently, the critical point for the initiation of fatigue cracks is the region where the weld reinforcement joins the base metal, as indicated at point A in Figure 5. However, if the weld reinforcement is removed and properly finished, the potential site for fatigue crack initiation shifts to the interface between the root weld reinforcement and the filling layer, identified as point B in Figure 5.

The inner layers typically have a superior finish and are less susceptible to intrusions and geometric discontinuities. However, the industry has expressed growing concern regarding fatigue failures that originate in the transition between the liner and the filling layer, as illustrated at points C and D in Figure 5. Point C is particularly critical as it represents the transition between three distinct materials with significant variations in metallurgical characteristics, often referred to as the triple point region [17].

It is important to note that the triple point introduces additional challenges in terms of inspection and fault assessment, especially when utilizing non-destructive testing (NDT) methods, as conventional techniques may be insufficient to ensure accurate detection of crack-like defects in this highly complex region.

2.5. Fatigue

Fatigue in metallic materials is a highly complex phenomenon that is not yet fully understood. In the presence of a weld, the problem becomes even more complicated due to additional variables introduced during welding, such as changes in the microstructure in the fusion zone, differences in the mechanical strength of the filler material (weld), the creation of brittle zones, residual stresses, the appearance of defects in the form of cracks, the geometry of the welded joint and distortions.

Material fatigue is a process by which metallic materials gradually undergo failure due to the repeated application of cyclic loads, even when these loads are well below the material's static breaking load. This makes fatigue an insidious phenomenon because failure is not immediate but develops over time, often going unnoticed until catastrophic failure occurs.

In welded structures, the presence of a weld creates areas of potential vulnerability due to microstructural changes and residual stresses generated during the welding process. These areas become susceptible sites for the initiation and propagation of fatigue cracks. Furthermore, the complex geometry of welded joints, along with associated distortions, adds complexity to the fatigue problem in welded structures.

The history of material fatigue dates to the 19th century when engineers and scientists began to observe failures in metallic structures that broke under repeated loads, despite being able to withstand much higher static loads. The first study on fatigue in metallic materials was conducted around 1829 by the German researcher W. A. J. Albert [20]. However, it was A. Wöhler who first applied rotating bending loads to railway axles during the period from 1852 to 1871 in Berlin [7]. In addition to these two researchers, Table 1 provides an overview of the historical development of fatigue [21].

Table 1: Overview of the historical development of fatigue.

Data	Researcher	Research
1829	Albert (Germany)	Failure due to cyclic loading was documented.
1839	Poncelet (France)	The introduction of the term "fatigue".
1849	IEM (France)	Refuting the theory of "fatigue crystallization" in metals.
1864	Fairbain	First experiments with cyclic loading.
1871	Wöhler	Investigation of the fatigue behavior of railway axles, rotating bending tests, S-N curves, concept of "fatigue limit".
1886	Bauschinger	Observations of the change in the elastic limit due to cyclic loading, stress-strain hysteresis curves.

1903	Ewing e Humfrey	Microscopic study disproves the crystallization theory; fatigue deformation occurs by slip, similar to monotonic deformation.
1910	Bairstow	Concepts of cyclic softening and hardening.
1929	Haigh	Difference in cyclic behavior due to notches, concepts of strain analysis in notches and stress concentration.
1955	Coffin e Manson	(working independently) - thermal cycling, low-cycle fatigue, considerations on plastic deformation.
1963	Paris e Erdogran	Crack growth rate described using the stress intensity factor.

Throughout the 20th century, research in material fatigue advanced significantly. Methods for predicting the fatigue life of components under cyclic loads, such as the S-N (stress-cycle) diagram, were developed and industry standards and regulations were established.

A study of fatigue life, particularly in aerospace components, provides both theoretical and practical insights into the useful lifespan of metallic alloys. In other words, it determines how many cycles (loading and unloading) the material can endure before catastrophic failure occurs. Fatigue failures in mechanical components typically initiate at the most stressed points in the form of small pre-existing cracks, either due to material manufacturing or those that develop over time around stress concentrators. These cracks propagate through cyclic deformations, gradually reducing the cross-sectional strength of the component. When this cross-section can no longer withstand the applied load, it leads to final rupture due to the sudden propagation of the crack [22]. The gradual growth of a fatigue crack is illustrated in Figure 6.
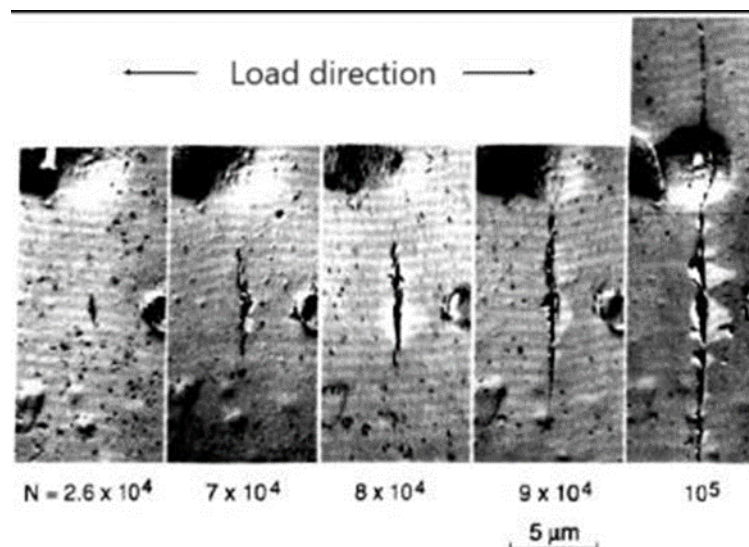
Figure 6: Gradual growth of a fatigue crack [19].

14

A crack can originate from an external (surface) or internal defect. When it is surface-related, it may arise due to machining irregularities, the geometry of the test specimen, or even from stress concentrators resulting from the method of component fixation. In rare instances, a fatigue crack may initiate within the material itself, where it involves a fragile microstructural interface, such as the interface between an inclusion and the base metal [6]. These inclusions can take various forms, depending on the material's manufacturing process and the chemical composition of these particles and they have a distinct impact on fatigue behavior, acting as crack nucleation sites. Furthermore, an internal crack can also arise due to phase changes in highly heterogeneous microstructures [9].

2.6. Fatigue Crack Nucleation

The initiation of a crack involves microstructural changes that lead to the nucleation of permanent damage, followed by the creation of microdefects that grow and coalesce into a dominant crack, often longer than the diameter of the grains forming the material's crystalline structure. The propagation of the dominant crack occurs in two phases, a subcritical growth phase characterized by stable growth, followed by growth to a critical size that results in structural instability or fracture. Suresh [7] emphasizes the significant influence of mechanical factors such as loading and residual stresses, as well as microstructural factors like crystalline arrangement and environmental factors such as acidic or alkaline environments, on the nucleation and defect growth rate.

In structures subjected to cyclic fatigue loading, it is common to find discontinuities located on the surface of components or near it. The nucleation mechanism of these discontinuities involves slip bands induced by cyclic plastic deformation. For plastic deformation to occur in metallic materials, it is essential for atomic planes known as slip planes, characterized by maximum atomic density, to move [23]. However, this movement would be impossible without the presence of a linear defect known as a dislocation. Figure 7 illustrates the theoretically natural sequence of dislocation movement in a wedge shape through the crystal lattice until it reaches the end of the crystal.
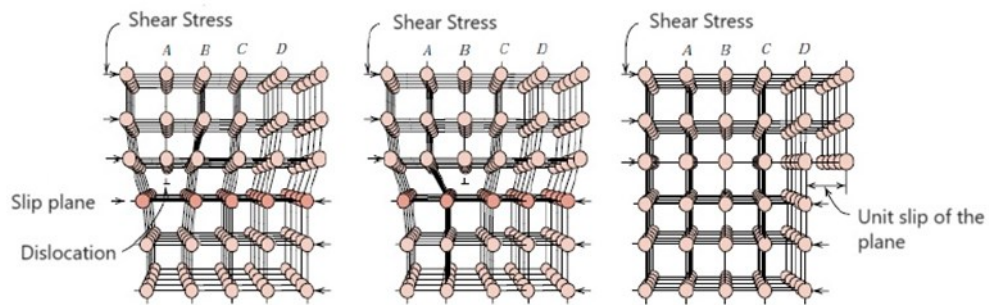
Figure 7: Illustration of the theoretical sequence of dislocation movement in the crystal lattice [23].

The movement of dislocations within the crystal lattice is driven by two factors: the lower amount of energy required for dislocations to move through a line within the lattice instead of displacing the entire plane over the same period and the presence of free electrons in metallic bonds, which facilitates the movement of dislocations. When multiple dislocations cross near-parallel slip planes, the crystal shifts, creating small cracks between the grain or phase boundaries and the discontinuities. The formation of dislocations is more likely to occur in areas with stress concentrations, such as cracks, inclusions and geometric changes in the material's cross-section. Even when the maximum stress is below the material's yield strength, fractures can occur if there are defects like cracks [19].

During the progression of fatigue, cyclic deformations occur, leading to an increase in surface roughness in various slip planes, resulting in the formation of extrusions and intrusions. These surface irregularities act as stress concentrators, contributing to the development of fatigue failures.

For a better understanding of fatigue crack nucleation due to geometric irregularities that develop on the metal surface, [23] proposed several models. These models are categorized based on the mode of sliding exhibited by the material and can be grouped into three main types:

- Models of simple slip systems.
- Models of alternate parallel slip systems.
- Models of slip line intersection.

16

According to Stephens [6], the preferential nucleation of fatigue cracks on or near the surface under cyclic loading can be explained by the fact that inelastic deformation occurs more readily at the surface. Additionally, the formation of slip steps (intrusions and extrusions, Figure 8 can occur in the surface region. In many cases, slip bands (parallel lines, Figure 8 are not the primary factors responsible for the formation of microcracks in metals, as fatigue cracks can nucleate at discontinuities or in regions close to them. These discontinuities may include inclusions, second-phase particles, corrosion pits, grain boundaries, twin boundaries, voids and pores. However, the development of microcracks is strongly influenced by the slip characteristics of crystallographic planes, grain size and the extent of plasticity near the crack tip.
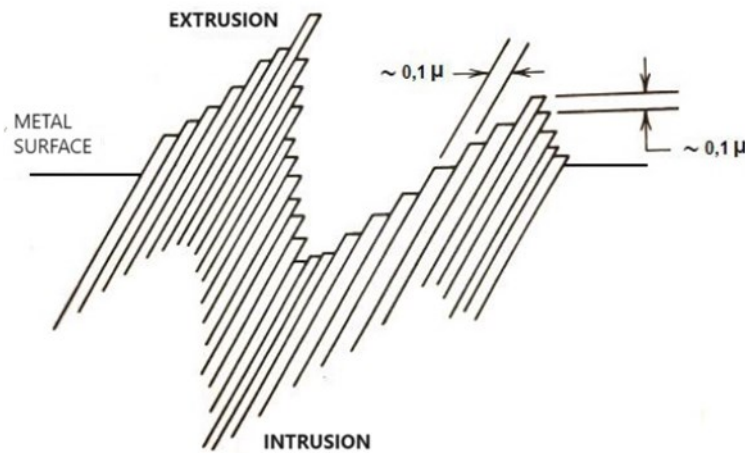
Figure 8: Slip scheme due to external loads in the stress cycle showing the formation of extrusion/intrusion [23].

2.7. Fatigue Crack Propagation

The propagation of fatigue cracks is often calculated using a methodology known as defect-tolerant. Most structures used or designed in engineering have some inherent defect due to the manufacturing or usage process. Therefore, the majority of the lifespan of these structures is spent propagating a pre-existing defect. This consideration is especially evident in the case of welded joints, which often represent the primary location for fatigue failures. The presence of macro or micro-discontinuities in the weld provides sites for the early nucleation of defects.

17

Residual tensile stresses, originating from high and non-uniform thermal gradients in the fusion zone, are another important factor that reduces the fatigue resistance of a welded joint.

An illustration of the fracture surface of a material that has failed due to fatigue is depicted in Figure 9. The key characteristics to be observed in such failures include a crack initiation point or site (typically on the surface), a region of crack propagation where "beach marks" are present and finally, a catastrophic rupture region that occurs when the crack reaches a critical size for the prevailing stress levels [24].

The duration of each phase depends on the testing conditions and the type of material. It is well-known that a fatigue crack can be initiated before ten percent of the material's total life has elapsed [9], [24], [25], [26].
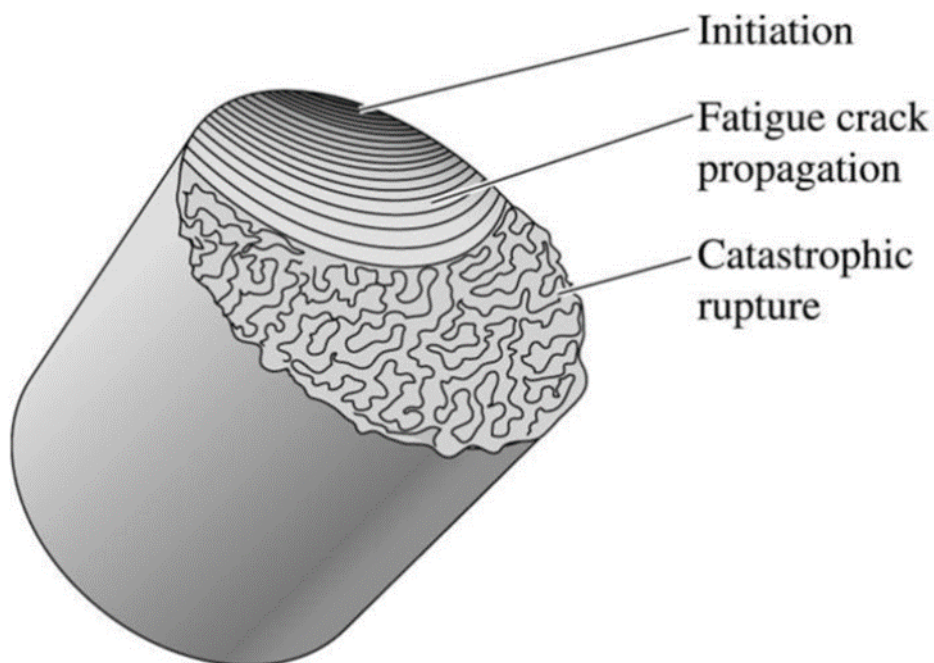
Figure 9: Representation of the characteristic surface of a fatigue fracture, distinguishing crack initiation, propagation and instability [27].

Macroscopically, two distinct regions can be observed on the fracture surface (Figure 9). The first region, with a smooth appearance containing the nucleation and propagation phases, exhibits characteristics of a brittle-type fracture, without signs of plastic deformation. Although plastic deformation is not evident at the macroscopic level, it can be observed microscopically through the formation of striations, which will be described in more detail in later sections. The second region has a coarse

18

appearance and corresponds to the final fracture of the component when the cross-section is no longer able to withstand the applied stress. The final failure can be either ductile (showing "dimples") or brittle (cleavage), depending on the level of applied stress. Figure 10 illustrates these two morphologies [25].

Thus, the fatigue life of a component should be analyzed differently for the crack initiation period and the propagation period, as the involved phenomena are distinct. The total number of cycles to failure, N_t, is obtained by summing these two stages: the nucleation life, N_n and the propagation life, N_p [24].
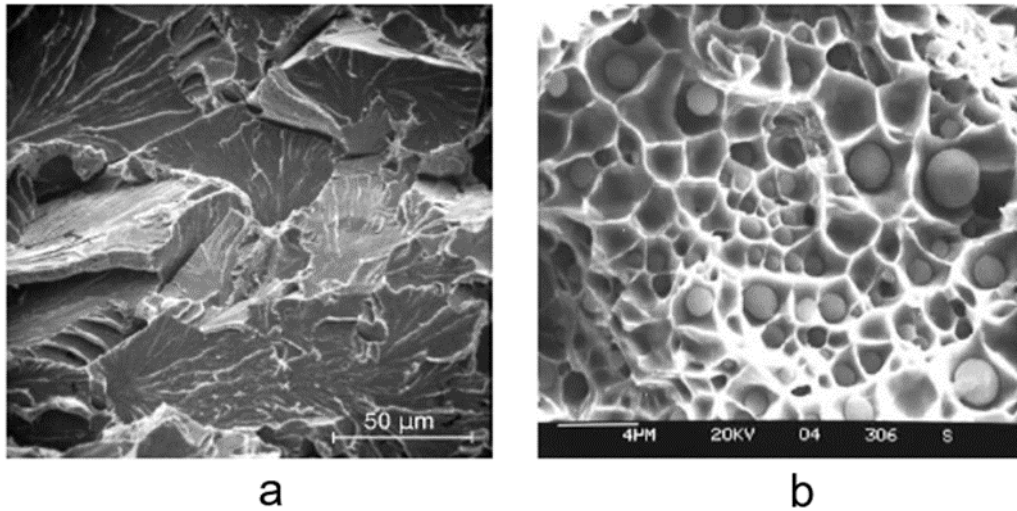
Figure 10: Typical characteristics of (a) brittle fracture, cleavage and (b) ductile fracture ("dimples") [28].

According to the ASM Handbook (1998) [29], once a crack of a few millimeters or more in length forms, the parameter that controls the fatigue crack propagation rate, da/dN, is the variation in the stress intensity factor, ΔK, provided that only a small amount of plastic deformation develops ahead of the crack. For a specific material and testing conditions, the crack propagation behavior can be described by a relationship between the fatigue crack propagation rate, da/dN and the variation in the stress intensity factor, ΔK. These test data are often represented on a graph in the form of a sigmoid curve, as shown in Figure 11 and in intermediate ranges of ΔK, it is common to find a linear relationship represented by Equation (1), which is known as the Paris-Erdogan Law.

$$\frac{da}{dN} = (C\Delta K)^n \quad (1)$$

According to Suresh [30], the constants C and m in the Paris-Erdogan equation are values influenced by various variables, including the material's microstructure, cyclic loading frequency, loading waveform, testing environment, temperature and the load

ratio, R. For ductile metallic alloys, the typical value of the constant m generally varies between 2 and 4.
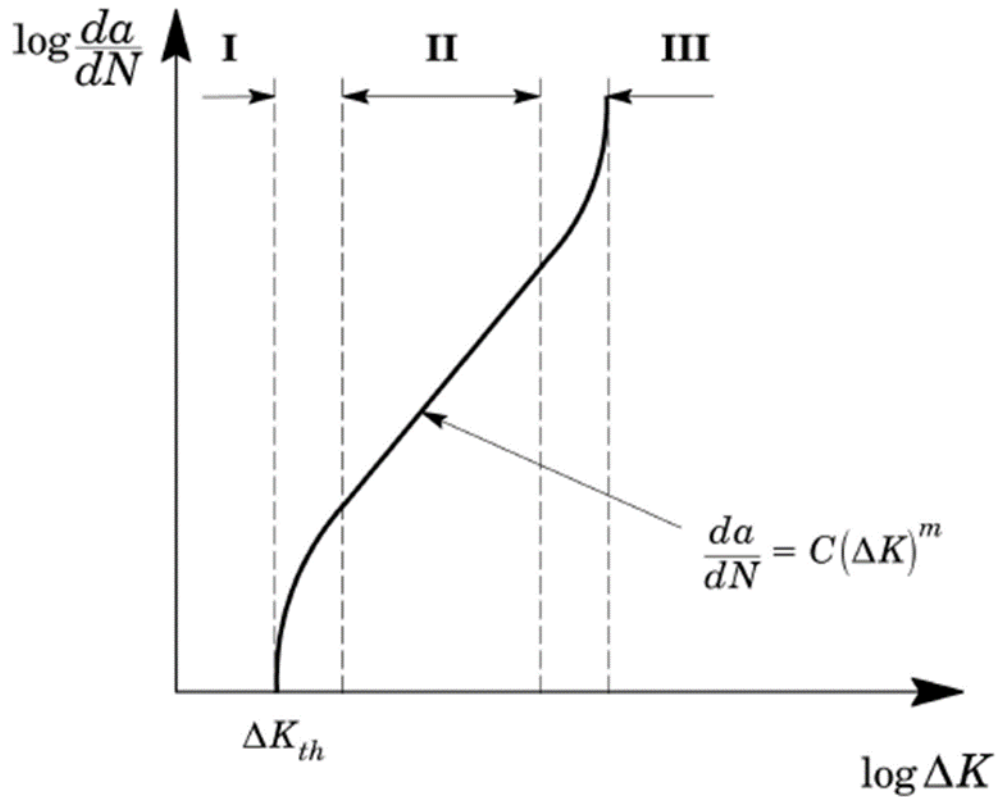
Figure 11: Variation of the crack growth rate with the number of cycles, da/dN, as a function of the cyclic variation of the stress intensity factor, ΔK_{th} [30].

Region I, depicted in Figure 11, is the primary focus of this study, as it represents the threshold region for crack propagation. In this zone, a highly nonlinear relationship between da/dN (crack growth rate) and ΔK (stress intensity factor range) is evident [7]. This nonlinearity is also observable as the crack approaches fracture [31]. ΔK_{th}, the limiting stress intensity variation for crack propagation, is suggested as the critical parameter when the propagation rate is equal to or less than 10^{-10} m/cycles (or 10^{-7} mm/cycles). This value is traditionally employed in damage-tolerant design principles [28], [32], where cracks are considered non-propagating if their stress intensity factor falls below the threshold value. It is essential to note that this property is determined based on a long crack that has previously propagated in a steady state and the stress fields following pre-crack growth can significantly impact fatigue crack propagation in Region I [34].

2.8. Effect of Crack Closure

A significant discovery for understanding the mechanisms of fatigue crack propagation was made by Elber in the 1960s. He observed differences in the compliance (C) of fatigue-tested specimens, as illustrated in Figure 12. The compliance of the specimen is defined by the ratio of displacement (ΔV) to load (ΔP). For high loads, compliance aligned with typical formulas from fracture mechanics, as found in ASTM E 647 [2], for example. However, for lower loads, the compliance of the specimen was similar to that of a defect-free body. Elber postulated that this variation in elastic compliance was caused by crack closure at lower, but non-zero, load levels.
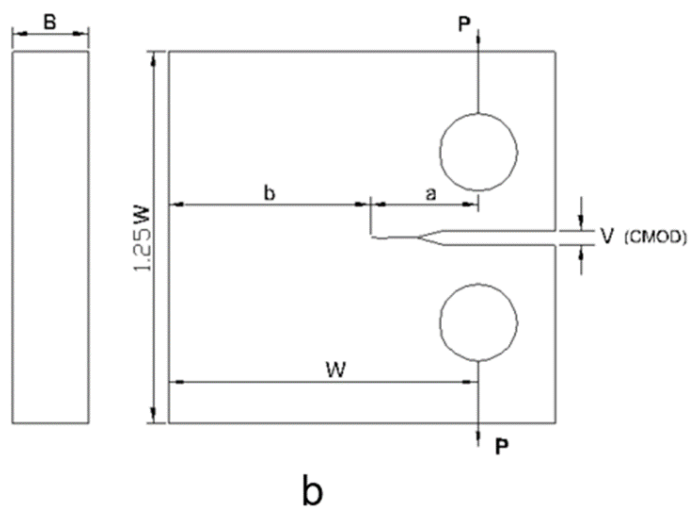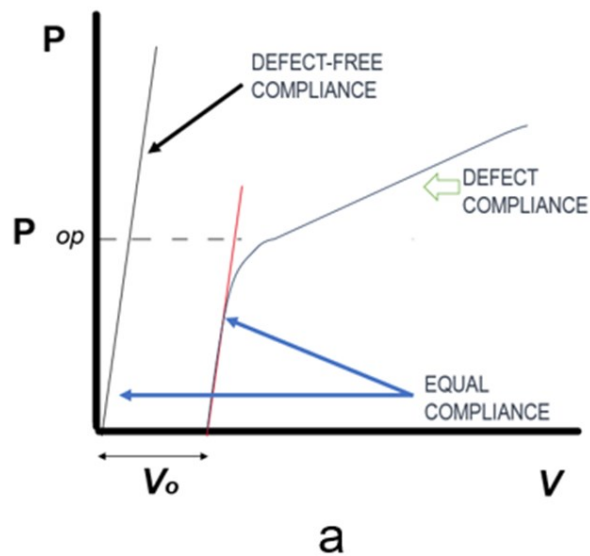
Figure 12: (a) Variation in flexibility due to crack closure, adapted from Anderson [9], (b) illustration of the displacement measurement point and the application of load on the C(T) specimen.

21

He argued that a zone of residual tensile deformation is left in the wake of a crack propagating due to fatigue. This deformed zone plastically, is responsible for the premature closure of the crack faces. This mechanism is known as plasticity-induced crack closure (PICC). In addition to PICC, other crack closure mechanisms have been identified in the literature, including closure caused by roughness, oxidation, viscous fluid, crack deflection, phase transformation and microcracks.

Crack closure is a phenomenon that slows down the crack growth rate, causing a delay in its progression. Elber [33] introduced the concept of $\Delta K_{eff} = K_{max} - K_{op}$ to account for the effect of crack closure on the propagation rate, where K_{op} corresponds to the stress intensity factor calculated at the point in the load cycle where the crack tip is fully open. This discovery was pivotal as it demonstrated that crack growth rates are influenced not only by conditions ahead of the crack but also by the nature of the crack faces. Therefore, to accurately predict fatigue crack growth rates, it is essential to consider loading history, crack length and stress states at the crack tip.

2.8.1. Significance of Closure

Using the $\Delta K_{th,eff}$ concept the influence of different external and internal parameters on the threshold values can be summarized as shown in Table 2. In this Table, a summary of various closure mechanisms explaining the threshold behavior is presented [34].

Table 2: ΔK_{th}-behavior related to external and internal parameters. [35].

Parameter	ΔK_{th}-behavior	Comments
External		
$R=K_{min}/K_{max}$	Max. values of ΔK_{th} at $R=0$ decresing ΔK_{th} –values with increasing positive and increasing negative R-values significant influence for coarse grained material; ΔK_{th} almost independent of R for fine grained material	Roughness induced closure: rough fracture surface at $R=0$ smooth fracture surface at higher R-values no R-dependency if $K_{min}>K_{cl}$
Tensile overload	Reduction of near threshold fatigue crack growth	Plasticity induced closure (crack has to transmit an enlarge plastic zone)
Compressive overload	Acceleration of near ΔK_{th} fatigue crack growth	Reduced crack closure due to flattening of the fracture surface asperities

Loading-mode	Higher ΔK_{th} in bending compared to tension-compression	Influence eliminated by closure (inhomogeneous plastic deformation)
Test-frequency	Minor increase of ΔK_{th} with increasing frequency	Formation of oxides on the crack surfaces
Test-temperature	ΔK_{th} increases with raising temperatures	Increased closure due to the formation of corrosion products (mainly oxides), predominantly roughness- and oxide induced closure
Environment	ΔK_{th} is to be almost independent of R in an inert environment compared to air increased ΔK_{th}, in oil compared to inert, gaseous environment	Lack of oxide induced closure, absence of roughness induced closure which is enhanced by fretting corrosion (loose particle), viscous induced closure

INTERNAL

Grain size	ΔK_{th} increases with increasing grain size	Coarser structures exhibit rougher fracture surfaces leading to pronounced roughness induced closure
Multi-phases	Higher ΔK_{th}-values compared to single-phase materials	Roughness induced closure and a meandering crack path (geometrical closure)
Metal-matrix composites	ΔK_{th} varies both with volume fraction and the average size of the reinforced hard particles	ΔK_{th} depends only on the mean particle size; there is no function of its volume fraction
Texture	ΔK_{th} depends on the angle between crack plane and crystallographic orientation	Fracture surface roughness caries with the crack-orientation (roughness-induced closure) large changes in crack path orientation cause geometrically induced closure

As reported in literature the most prominent external parameter affecting ΔK_{th} is the R-ratio, while external parameters also affect ΔK_{th} caused by different closure mechanisms [36]. However the use of the $\Delta K_{th,eff}$ concept reduces their influence (see Table 2).

2.9. Factors Influencing Fatigue Crack Propagation

Fatigue crack propagation is influenced by various factors, including the mean stress (σ_m), which typically varies in terms of the load ratio R, material anisotropy, microstructure and surface finish.

2.9.1. Effect of Stress Ratio or Loading

The load or stress ratio $R\ (= P_{min}/P_{max} = \sigma_{min}/\sigma_{max} = K_{min}/K_{max})$ is one of the key mechanical variables in fatigue and has a significant impact on the crack growth rate. The value of R affects the crack growth rate similarly to the observed effect in S-N curves for different R values and mean stress. For a given ΔK value, the higher the R value, the greater the crack growth rate and vice versa. Figure 13 illustrates the influence of the R ratio on the crack growth rate in an AISI 4340 steel.
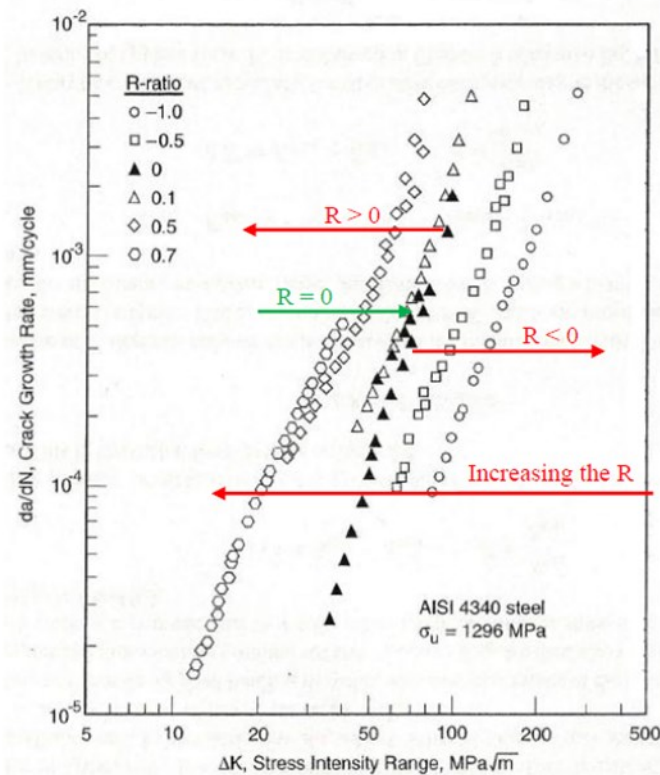
Figure 13: Influence of the R ratio on fatigue crack propagation rate [37].

2.9.2. Effect of Anisotropy

The effect of anisotropy is a significant phenomenon in certain materials, notably aluminum (Al) and titanium (Ti). Anisotropy refers to the material properties' dependency on the measurement direction, a crucial consideration in the design and analysis of components and structures composed of these materials. To identify anisotropy, a standardized notation outlined by ASTM E399 [38] is commonly

24

employed. This notation is vital for specifying the loading direction, fracture plane and crack propagation direction. Figure 14 visually illustrates the application of this notation, providing a valuable reference for engineers and researchers. Understanding the impact of anisotropy is essential for optimizing the performance and safety of products and structures constructed from materials such as aluminum and titanium, facilitating a more precise and efficient approach to the analysis and design of components subjected to various loading conditions and fracture scenarios.
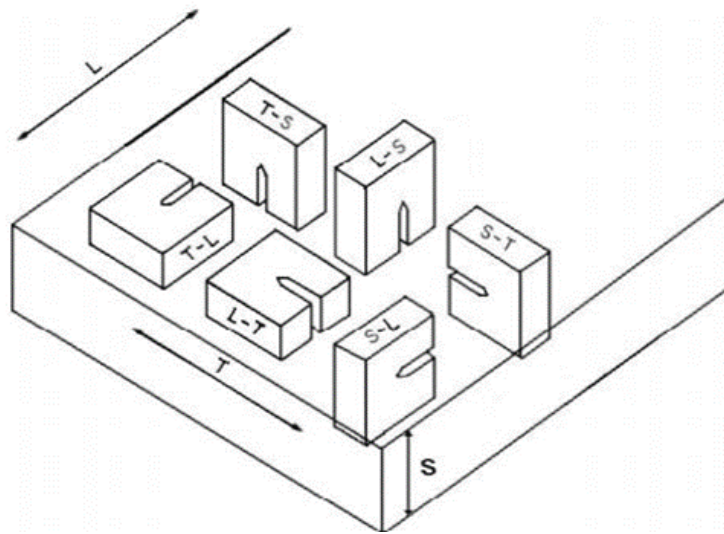
Figure 14: Code for crack plane orientation in rectangular sections [39].

The letters L, T and S are associated with the directions of length, width and thickness, respectively, with the L direction coinciding with the main direction of mechanical forming (rolling, extrusion, or forging). In the identification of test specimens, the first letter indicates the loading direction and the second letter indicates the crack propagation direction in the fracture plane. Figure 15 depicts fatigue crack growth curves for the Al-2090-T8E41 alloy obtained from test specimens oriented in different LT and SL directions [40]. Notice a significant influence of material orientation on fatigue behavior, particularly in the ΔK_{th} threshold region. This is attributed to the structure of elongated non-recrystallized grains.

Due to the structure of elongated, non-recrystallized grains perpendicular to the smallest transverse direction, crack extension in the plane of forming (SL, ST) occurs through an intergranular delamination mechanism, with minimal changes on the crack surfaces. In contrast, a significant alteration is observed for crack extension

perpendicular to the plane of forming (TL, TS), where growth is primarily crystallographic, featuring microscopic deflection and macroscopic branching [40].
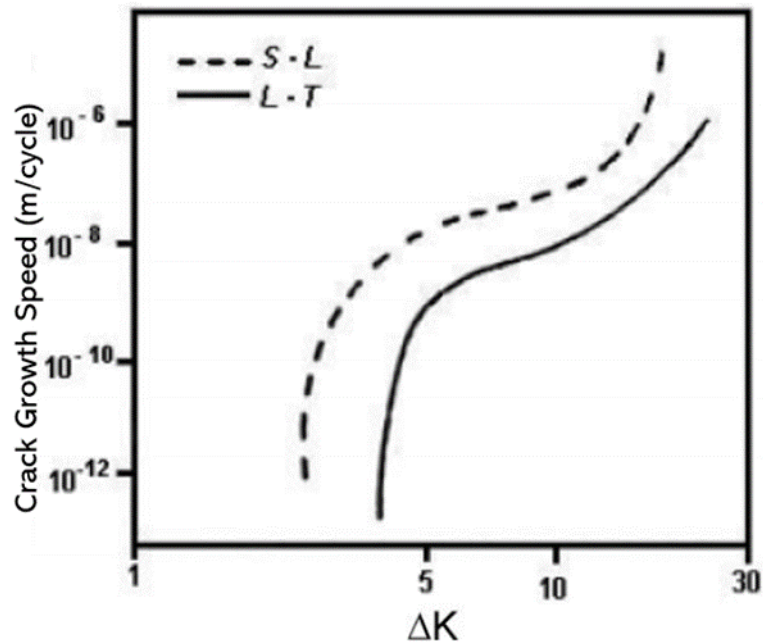
Figure 15: Influence of anisotropy on fatigue crack propagation in Alloy Al-2090-T8E4 [40].

2.9.3. Fracture Mechanics-Based Fatigue Crack Growth Theories

Three main categories of fracture mechanics-based models have been identified: (i) linear elastic, (ii) geometrical and (iii) plastic accumulation models [41]. Here, our emphasis will be on dislocation mechanism-based models. These models offer valuable insights into fatigue crack growth by examining dislocation behaviors at the microstructural level. A dislocation-based approach allows for a fundamental understanding of how plastic deformations impact crack tip stresses and growth.
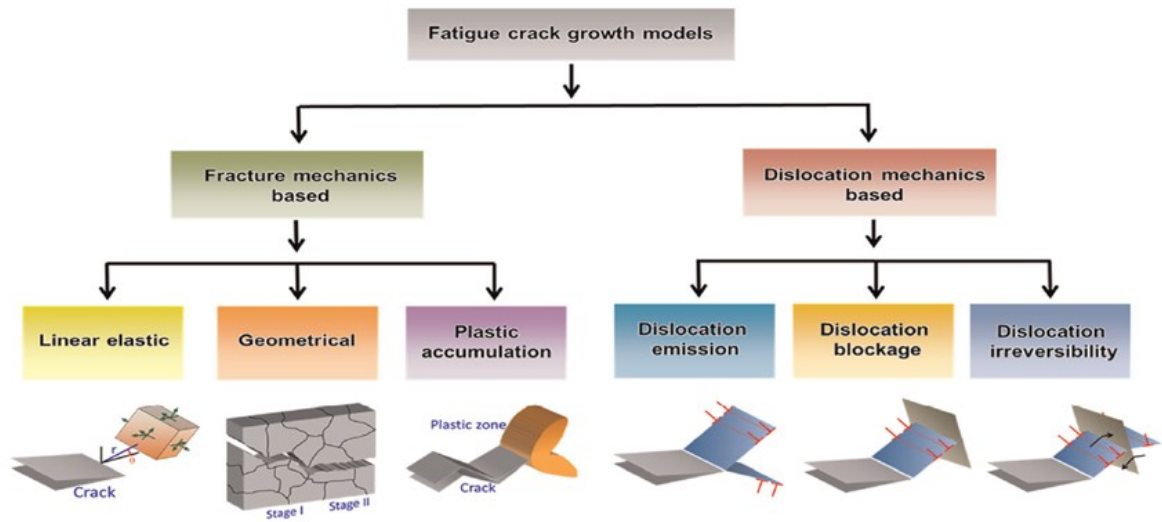
Figure 16: A systematic classification of the predictive fatigue crack growth models [41].

2.9.3.1.   Dislocation Mechanics-Based Fatigue Crack Growth theories.

Extensive experiments confirm that fatigue crack growth at the mesoscale is governed by ubiquitous slip phenomena. It is now accepted that based on the dislocation slip history (equivalent to the plastic zone size in a continuum context), an advancing crack will exhibit either microstructure-sensitive or insensitive behavior. Therefore, fatigue crack growth can be most accurately modeled by incorporating variables controlling dislocation characteristics at the mesoscale level.

Slip-based theories enable examining ductile versus brittle tendencies, interface roles and irreversible damage mechanisms. These models can be classified into three major categories (Figure 16): (i) dislocation emission, where new dislocations are generated at the crack tip; (ii) dislocation blockage, where dislocation motion is obstructed by microstructural barriers; and (iii) dislocation irreversibility, where non-recoverable plastic deformation occurs [41].

Incorporating fundamental dislocation dynamics and slip processes is key to improving fatigue predictions. Capturing crack tip dislocation interactions, slip localization and obstruction provides vital insights into microstructure-sensitivity. This approach relates measurable variables to crack growth on a fundamental level.

2.10. Small and Short Cracks Growth

Engineering definitions of small and long cracks at the fatigue limit under tensile mean stress and a prediction method for determining the fatigue limit of a cracked Mg alloy

27

have been extensively studied. Murakami [42] proposed the ΔKth prediction equation for small cracks, which is valid for materials where the area parameter (√area) is less than 1000 microns. This equation highlights the significant difference between the effects of small and long cracks on fatigue strength. Shigeru Hamada, Takuya Kinoshita, Kazunori Morishige, Komei Hayashi, Toshiyuki Ishina, and Hiroshi Noguchi [43] have contributed to the understanding of fatigue behavior in cracked Mg alloys by investigating the fatigue limit under tensile mean stress conditions. Their research aims to provide a comprehensive prediction method for determining the fatigue limit of cracked Mg alloys, taking into account the distinct behaviors of small and long cracks.

In Region I, it is observed that short or small cracks exhibit notably faster growth rates in comparison to those recorded in specimens featuring longer cracks [44], [45], [46]. Small cracks are characterized by having all their dimensions smaller than a specific characteristic dimension, which could be the average grain size (microstructural dimension), the size of the plastic zone (mechanical dimension), or the length of the crack faces that experience closure (physical dimension) [45].

For microstructurally small cracks that propagate in tests conducted with a constant force amplitude, the growth rate is considerably higher than what is observed for longer cracks, as depicted in Figure 17(a). As the crack advances, its rate gradually diminishes due to interactions with grain boundaries and grains with unfavorable orientations, eventually reaching a minimum when the crack size is approximately equal to the grain size. On the other hand, short cracks, which possess only one dimension smaller than a characteristic size, often originate from less sharp notches and surface defects. These cracks exhibit an anomalous behavior, as illustrated in Figure 17(b), which is primarily attributed to the absence of the closing effect [8], [47].
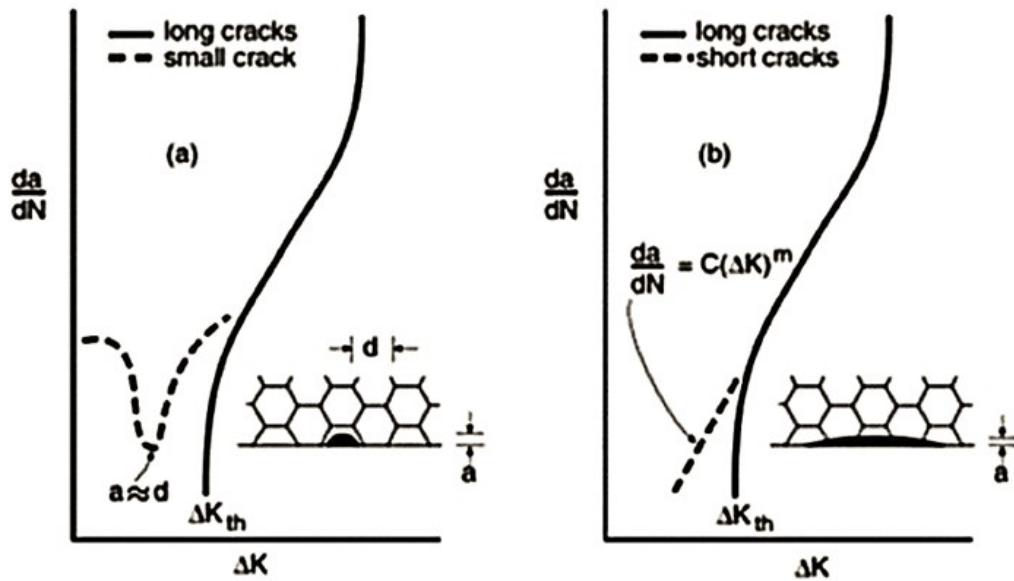
Figure 17: Behavior of cracks in propagation regime I: (a) small cracks; (b) short cracks [8].

Additionally, short cracks that originate from machined notches exhibit distinct behaviors [48]. In these instances, the crack interacts with the elastic and plastic stress fields induced by the notch creation process. The observed behavior within Region I can vary, as depicted in Figure 18. Newman and Yamada [49] found that this interaction can be mitigated when the pre-crack is initiated using compression-compression techniques, ensuring an experimental measurement of ΔK_{th} at the lower limit [49], [44].
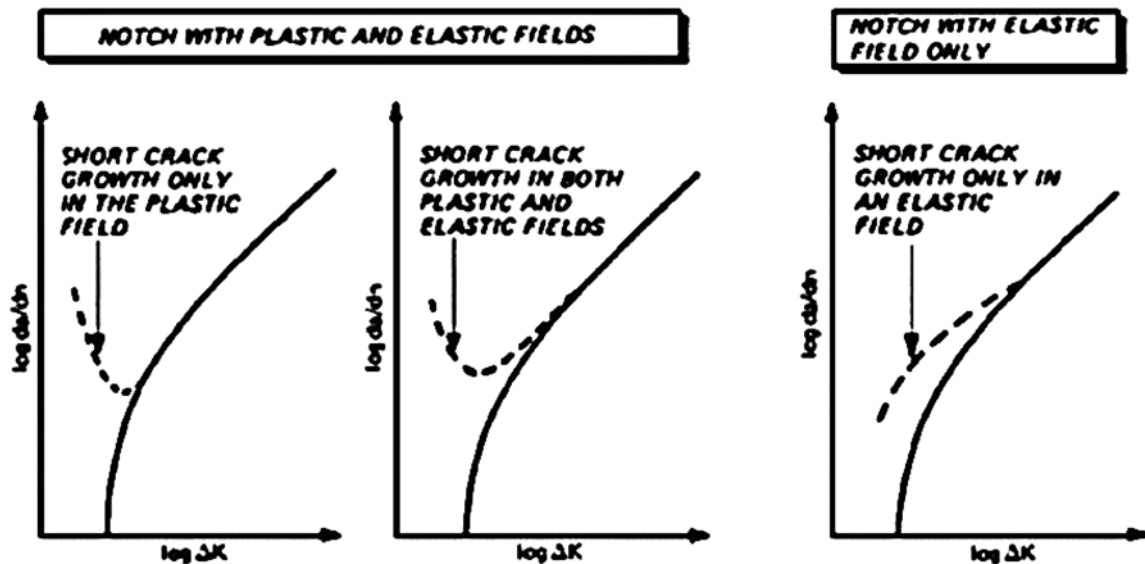
Figure 18: Effect of the crack propagation interaction with the elastic and plastic stress fields of the machined notch for the case of physically short cracks [8].

CHAPTER 3

3. OVERVIEW OF CURRENT FATIGUE THRESHOLD TEST PROCEDURES

3.1. Introduction

This chapter present an overview of testing methods employed to generate fatigue thresholds often involve compression-compression precracking techniques to induce beneficial tensile residual stresses at the crack tip, minimizing closure influences under constant amplitude loading. This enables natural development of realistic crack surface conditions and crack tip interactions, providing fatigue data tailored for damage tolerant design.

3.2. Testing Methods Employed to Generate Fatigue Thresholds

To generate near-threshold fatigue crack growth rate data without significant load history effects, a compression-compression precracking method was utilized. This technique was originally developed by Hubbard et al. [50], Topper and Au [51], Pippan et al. [52], [53], Forth et al. [54] and Newman et al. [49]. Compression precracking induces beneficial tensile residual stresses at the crack tip, minimizing closure influences under constant amplitude loading [55], [56].

This enables natural development of crack surface conditions, including oxide formation, fretting debris, roughness and plasticity-induced closure. Environmental and mechanical crack tip interactions proceed unaffected, representing realistic service behavior.

Some reasons why one would want to allow these conditions include:

- Oxide formation, roughness, and debris can impact crack tip stress fields and crack growth rates, so allowing them provides a more accurate depiction.
- Plasticity-induced crack closure is an important shielding mechanism that reduces the effective crack driving force. Allowing it captures this effect realistically.
- Studying crack growth with these conditions present allows understanding their synergistic interactions and developing models/predictions closer to real service performance.
- For very small cracks, these conditions can dominate the crack tip process zone behavior, so allowing them is essential for accurate short crack modeling.
- It enables validation of numerical models and experiments against the complexity of realistic service-like conditions.

Compression precracked thresholds exhibit higher validity and consistency compared to conventional methods. By limiting artifact-inducing load reversals during initiation, intrinsic growth rate drivers can be isolated near the threshold. The enhanced representation of service crack features and fields provides fatigue data tailored to directly inform damage tolerant design.

The conventional experimental procedures for establishing fatigue thresholds are detailed in ASTM E647 [2], known as the "Standard Test Method for Measurement of Fatigue Crack Growth Rates." To assess threshold and near-threshold conditions, Newman [49] employed three distinct methods. The initial approach adhered to the standard load-reduction (LR) test method outlined in ASTM E647 [2] for threshold determination. Careful consideration was given to the selection of initial starting load levels to ensure that crack growth rates, originating from the crack-starter notch, remained below 10^{-8} m/cycle at the outset of the LR test, as stipulated by the standard. A consistent load reduction rate of $C = -0.08\ mm^{-1}$ was maintained throughout all LR tests. As soon as the growth rates approached or reached the target value of 10^{-10} m/cycle, the test control protocol was modified to implement constant-amplitude loading at higher ΔK values. This adjustment allowed for the generation of data pertaining to the mid- and upper regions of the crack growth rate curve.

The second approach involved the utilization of compression precracking constant-amplitude (CPCA) loading. As depicted in Figure 20(a), this method entailed precracking the specimens under compression-compression loading conditions. To facilitate this, small metallic blocks were affixed to the upper and lower edges of the specimen. These blocks allowed the loading clevises to establish contact and transmit cyclic compressive loads at a frequency of 5 – 10 Hz to the specimen. To ensure safety, smaller pins were inserted to prevent inadvertent dislodging of the specimens from the clevis.

It's worth noting that the stress intensity factor solution for the compressive-loaded case remained consistent, deviating by no more than ±0.5% from the standard stress-intensity factor solution (0.2 < c/W < 0.8) for the compact specimen [49], [54]. In the CPCA method depicted in the accompanying figure, a small fatigue crack, which naturally ceases further growth, is initiated at the tip of the crack-starter notch through compression-compression load cycling. This unique loading scenario results in a

tensile residual-stress field enveloping the crack tip, contrary to the typical compressive residual stresses observed in tension see Figure 19.

In the broader context, when the crack ceases its progression, the crack surfaces fully separate, signifying that a threshold has been reached under compression-compression loading conditions [49], [56]. This is in stark contrast to the outcome observed under typical tension loading, where the crack surfaces come together upon reaching a threshold.
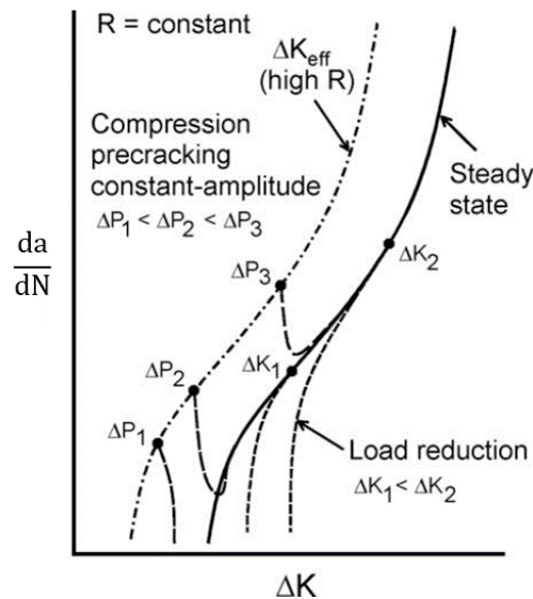
Figure 19: Typical fatigue-crack-growth data under constant amplitude load reduction (CPCA) [49].

(a) Compression loading

(b) Standard pin loading
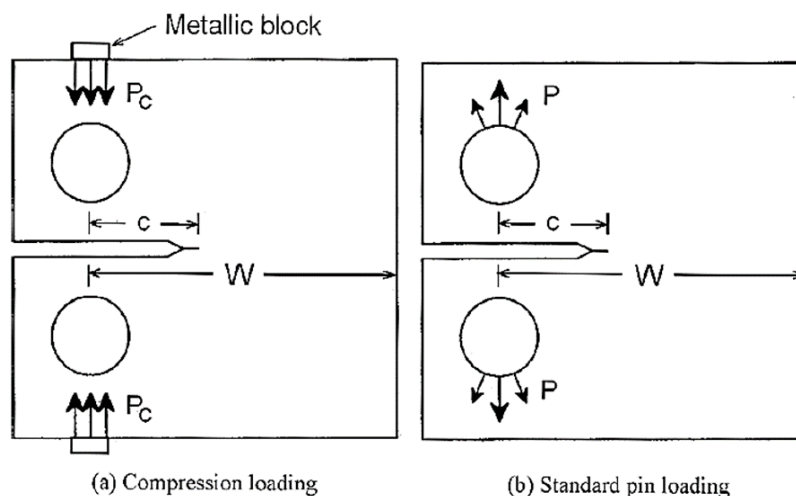
Figure 20: Method of loading applied to compact specimens (a). Compression loading. (b). Standard pin loading [49].

Subsequent to compression precracking, a constant-amplitude loading regimen (as illustrated in Figure 20(b) was executed, maintaining stress-intensity factors at or below the anticipated threshold range. This was continued until there was a noticeable, sustained increase in crack growth rates. In cases where minimal or negligible crack growth was observed after approximately one million cycles, the applied loads were incrementally raised by approximately 5 – 10% while maintaining a constant stress ratio (R). The specimens were subjected to another cycle to scrutinize for any discernible crack propagation.

The third method involved compression-compression precracking, followed by constant-amplitude loading and subsequently transitioning to a load-reduction phase following established ASTM E-647 procedures. Notably, the initial stress-intensity factor range and crack-growth rate at the commencement of the load-reduction test were significantly lower than the maximum values permissible by the current standard. This approach is referred to as compression precracking load-reduction (CPLR) threshold testing and the corresponding loading sequence is illustrated in Figure 21 [50].

While the technique for generating compression cracks has seen successful application by numerous researchers, it is evident that a standardized procedure with unrestricted accessibility is lacking. Such a procedure should offer clear instructions on calibrating and fine-tuning the test parameters, as well as conducting precise measurements of the key values of interest. Although some research outcomes are documented in the scientific literature, the absence of a comprehensive and widely disseminated protocol hinders the broader adoption and application of this valuable testing method.
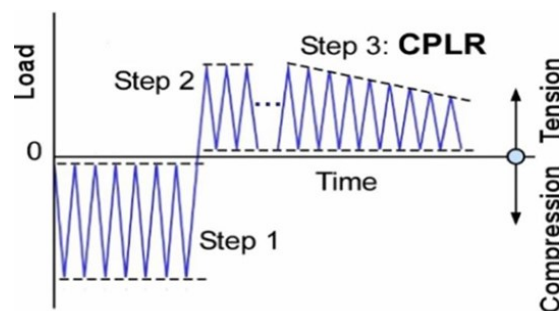
Figure 21: Determination of ΔK_{th} values after compression precracking: compression pre-cracking load reduction (CPLR) [56].

3.3. Load Shedding (K-Decreasing) Procedure

In the two most well-known standards regarding FCG tests, namely ASTM E647 [2] and ISO 12108 [57], ΔK_{th} is defined as the asymptotic value of stress intensity factor range, ΔK, at which the fatigue crack propagation rate, da/dN, approaches zero. These standards employ a load shedding procedure at constant load (stress) ratio, defined as the algebraic ratio of the minimum to maximum load (stress) in a cycle, given by $R = P_{min}/P_{max}$, with P_{min} and P_{max} representing the minimum and maximum applied load in a cycle. Figure 22 (a) displays a schematic sigmoidal variation of fatigue crack growth rate, da/dN, with alternating stress intensity factor, ΔK. The log-log plot of da/dN vs. ΔK depicted in this figure illustrates three distinct regions describing typical fatigue crack growth behavior in metals, in which the linear region (also referred to as region II) is most often described by a power law in terms of $da/dN = C(\Delta K)^m$, where C and m are material constants that are determined experimentally [9].
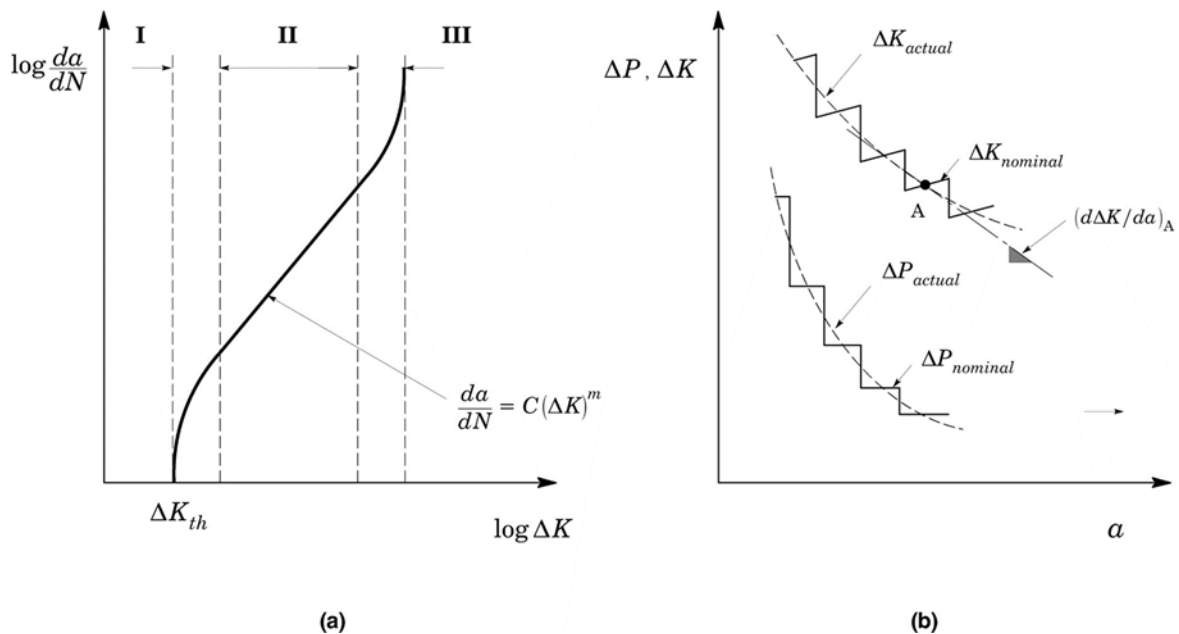
Figure 22: (a) Schematic sigmoidal variation of fatigue crack growth rate, da/dN, with alternating stress intensity factor, ΔK, in metals. (b) Typical K decreasing test procedure based on stepped load shedding [30].

Now, limiting attention to the threshold region (which is often referred to as Region I, threshold levels are approached using a K-decreasing test method involving a successive load reduction procedure followed by measurements of crack growth rate taken at each load level. Ideally, the threshold stress intensity factor, ΔK_{th}, should

represent the alternating value of ΔK corresponding to an infinitesimal growth rate. However, for the purposes of a more practical measurement, it is more useful to adopt an operational definition for ΔK_{th} in terms of a maximum growth rate in connection with the accuracy of the crack monitoring technique and the elapsed number of cycles.

Following ASTM E647 [2], the near-threshold regime is determined by first precracking the test specimen and slowly reducing the applied stress intensity factor, K, as defined by the *K-gradient* given by equation (2).

$$C_{th} = \frac{1}{K}\left(\frac{dK}{da}\right) \quad (2)$$

where $C_{th} \geq -0.08$ mm^{-1} to preclude anomalous results.

Testing starts at a level of K_{max} (or ΔK) equal to or greater than the final precracking values. Following crack extension, the applied load is decreased (shed) as the crack grows and test data are recorded until the lowest ΔK, or crack growth rate of interest is achieved. The *K-decreasing* test can be controlled by a stepped stress intensity factor following a selected crack extension at a constant ΔP, as schematically shown in Figure 22 (b).

3.4. Compression Precracking Method.

The Compression Precracking Method (CPM) has become an essential approach to minimize the confounding influence of crack closure on stress intensity factors and crack opening displacements during load reduction procedures. This is especially critical near the threshold regime (see at. [58], [59], [60], [61] for supporting experimental evidence). Accurately quantifying the crack closure phenomenon is imperative to comprehensively characterize near-threshold fatigue crack growth behavior, given the intricate nature of closure and numerous unresolved matters associated with it.

To tackle these research gaps, the Compression Precracking (CPC) technique presents an alternative methodology to obtain near-threshold fatigue crack growth data without substantial artifacts from crack closure and load history effects. The CPC approach has principally progressed along two related trajectories: the Compression Precracking Load Reduction (CPLR) method and the Compression Precracking Constant Amplitude (CPCA) protocol.

In both CPC routines, compressive maximum and minimum loads are applied, causing localized yielding at the crack tip and ensuing crack extension in the resulting tensile residual stress field [62]. The cyclic compressive loading perpetuates cracking through the residual stress zone until these stresses subside, arresting crack growth. Forth et al. [54] implemented a CPC procedure followed by CPCA testing to quantify Fatigue Crack Growth (FCG) kinetics devoid of any load shedding influences. After compression precracking, a constant loading amplitude is deployed to document near-threshold FCG trends.

More recently, Newman and Yamada [49] executed a CPC program, combining compression precracking with a load reduction scheme similar to ASTM E647 [2].

Figure 23 shows a schematic illustration of the compression precracking procedure adopted to generate a compressive stress on the crack plane for the tested specimens. However, the initial ΔK and crack growth rate values were smaller than the maxima enshrined in the code. Figure 24 outlines both the CPCA and CPLR compression precracking protocols to obtain near-threshold fatigue crack growth data.
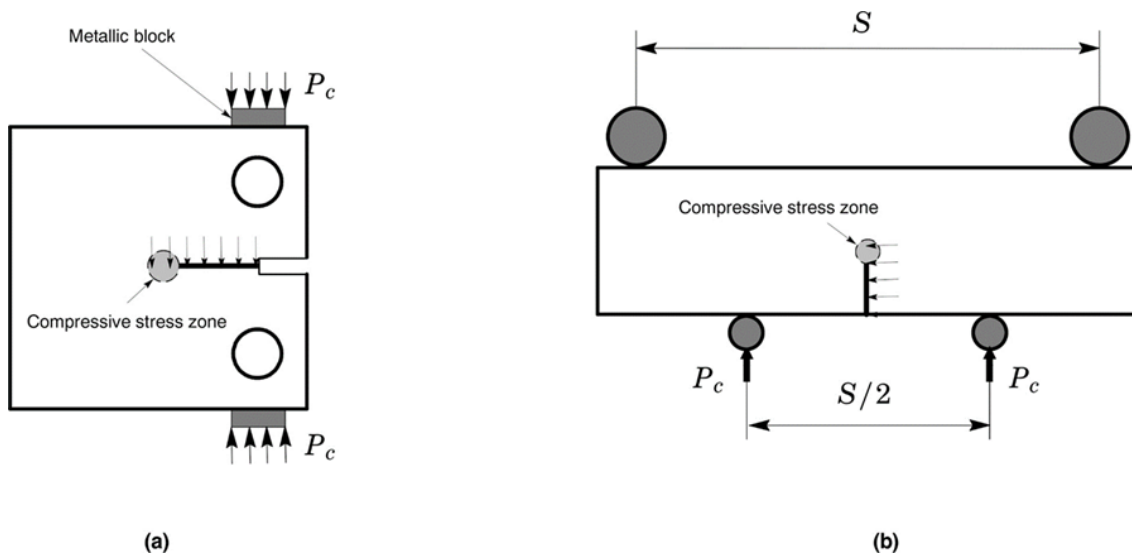
Figure 23: Schematic illustration of the compression precracking procedure adopted to generate a compressive stress on the crack plane for the tested specimens by applying a compressive load, P_c: (a) Compact tension, C(T), geometry [42]. (b) Single-edge notched bend, SE(B), specimen under four-point bending.
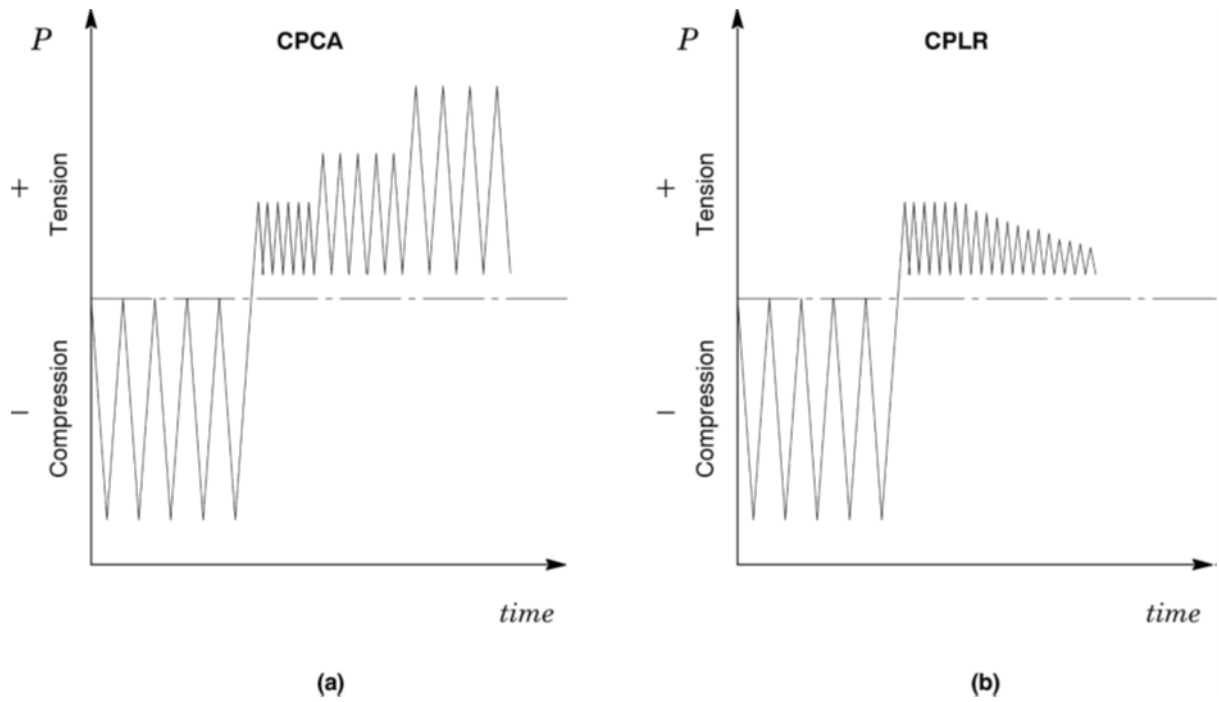
Figure 24: Typical compression precracking (CPC) schemes: (a) compression precracking constant amplitude (CPCA) procedure and (b) compression precracking load reduction (CPLR) technique [30].

CHAPTER 4

4. EXPERIMENTAL PROGRAM

4.1. Introduction

This section provides crucial insights into the experimental fracture tests performed on compact tension C(T) and single-edge bend SE(B) specimens. The following flowchart presents an experimental program outlining three different material types used to improve the methodologies employed for measuring the fatigue crack growth threshold. Additionally, it details the tests conducted to obtain the corresponding data results.
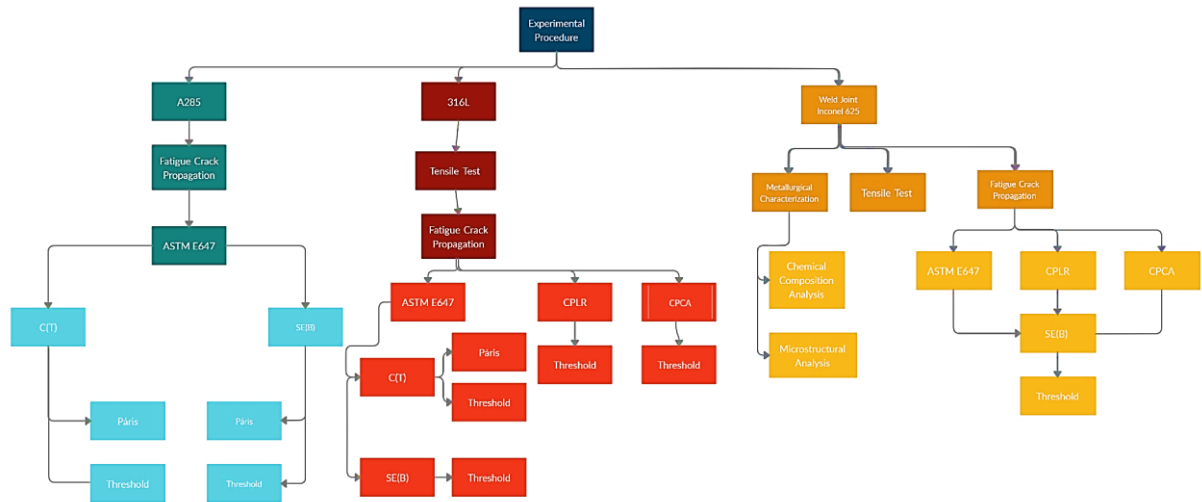
4.2. Experimental Procedure

The proposed experimental procedure involves two distinct stages. In the initial phase, pre-crack nucleation is achieved through fatigue by applying compressive loading in bending at four points. Once the pre-crack is established, resulting in practically insignificant residual plastic deformations ahead of the crack, the test transitions to its second stage. This phase aims to determine and evaluate the fatigue crack propagation threshold ΔK_{th}, with the specimen conventionally stressed in Mode I through three-point bending.

It is noteworthy that the initial parameters for the test, particularly the pre-crack opening in compression for the C(T) and SE(B) geometry, lack extensive documentation or publication in the existing literature and their definitions are not straightforward. Consequently, the experimental program will be meticulously executed to develop, test and validate routines for determining these test parameters. The establishment of test parameters will involve a thorough process of experimental steps, complemented by computational analyses. This approach is crucial for estimating fatigue pre-crack

growth in specimens with SE(B) geometry while mitigating the effects of loading history on the material.

The comprehensive nature of this experimental program underscores the need to address the current gaps in understanding and documentation of key parameters related to pre-crack initiation. Through a systematic approach, combining experimental procedures and computational analyses, this research aims to contribute valuable insights into the behavior of specimens subjected to compressive loading and subsequent fatigue crack propagation. Ultimately, this methodology will enhance the reliability and applicability of fatigue testing procedures, particularly for specimens with SE(B) geometry.

For the development of this experimental test procedure, three distinct steps will be established:

I. Threshold Tests: This phase involves conducting the "Threshold" test following the standardized procedure outlined in ASTM E647 [2].

II. Finite Element Method (FEM) Computational Analysis: Computational analysis using the Finite (FEM) will be employed to evaluate the evolution of stress/strain fields during the cyclic loading step for pre-crack nucleation in compression. This will be carried out using the SE(B) geometry and under compressive loading in 4-point bending. For detailed information on the computational analysis conducted to assess the stress/strain fields, please refer to Appendix A.

III. Exploratory Fatigue Crack Nucleation and Propagation Tests: This step involves several subtasks:

    a. Verification of Pre-crack Nucleation: Comparison of pre-crack nucleation by compression in 4-point bending with results obtained via FEM.

    b. Evaluation of Test Parameter Experimental Variation: Assessment of the impact of varying test parameters on pre-crack nucleation .

c. Testing on Homogeneous Base Materials and Girth Weld Clad Pipes: Conducting tests on homogeneous base material (steel 316L) and subsequently on girth weld clad pipes.

d. Complete Test: Performing a comprehensive test involving the nucleation of the pre-crack in compression by 4-point bending and determining the "Threshold" in 3-point bending.

The utilization of homogeneous materials in the initial exploratory tests is essential for assessing the fundamental parameters of the tests. This approach allows for the mastery of the compression-compression technique required for inducing fatigue crack nucleation in 4-point bending. The choice of homogeneous materials is particularly strategic because the assembly of girth weld is not only costly and challenging but also lacks the availability of surplus material. This initial phase with homogeneous materials provides a controlled environment to fine-tune the experimental procedures before progressing to more intricate and resource-intensive tests involving girth weld joint.

4.3. Finity Element Methods (FEM)

Since the MTS machine does not have the configuration for carrying out tests at four points, it is necessary to determine the relationship between the applied load (P) and the stress intensity factor (K_I). For this purpose, finite element analysis is used using the ABAQUS software, for a SE(B) geometry, a/W=0.3, material AISI 316L, loading mode by compression compression 4 points.

The starting point for the realization of this analysis FEM was based on the work [63] where the authors determined the relationship between P and K_I for the configuration shown in the Figure 28(a) in which D represents the inner span and S = 4W where the loads in front of the notch tip are of tractive magnitudes, therefore they generate crack opening.

For this job, it is necessary to carry out a pre-crack in loading by compression-compression and it is not yet standardized in fracture toughness test procedures the 4-point bend geometry [64], [65], [66], [34] displayed in Figure 28(b) shows the configuration to generate the crack closure which will be used as the initial stage to

42

determine the threshold in which the external span *S/W* = 8 and the internal span *S/W* = 4.
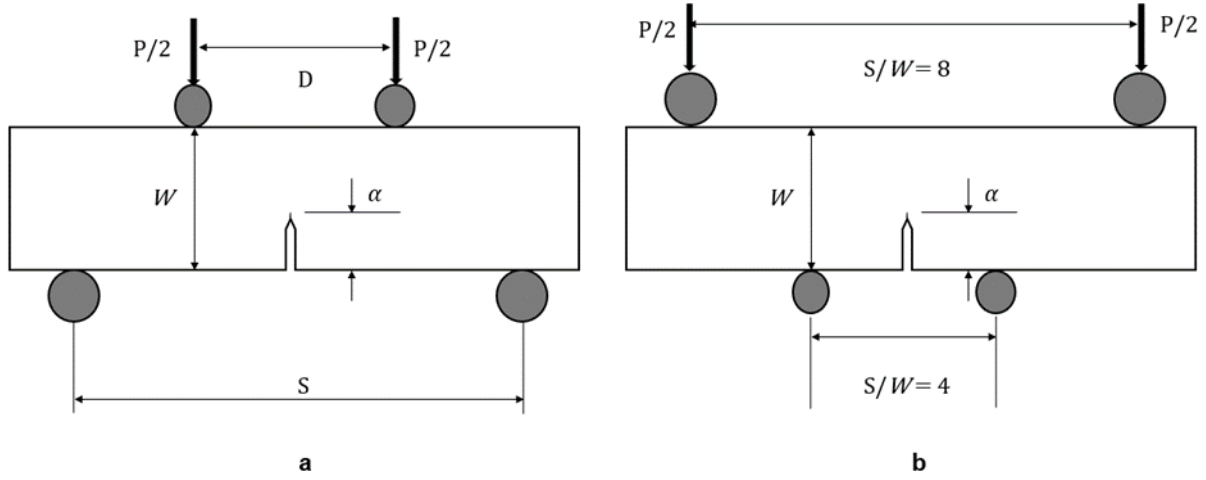
Figure 25: Conventional bending loading geometries adopted in the present work: (a) 4-point SE(B) specimen. (b) 4-point compression pre-crack opening process.

The stress intensity factor for a bend geometry is conveniently defined in the form [2].

$$K_I = \frac{PS}{B_N W^{3/2}} F(\frac{a}{W}) \quad (3)$$

Where $F_{(a/W)}$ defines a nondimensional stress intensity factor dependent upon specimen geometry and crack size. Here, *P* is the applied load, B_N denotes the net specimen thickness at the side groove roots *(B_N = B* if the specimen has no side grooves where *B* is the specimen gross thickness) and W is the specimen width.

An extensive series of linear finite element analyses for the 4P bend specimens considered in the present study was conducted to evaluate the nondimensional stress intensity factor, $F_{(a/W)}$, for different *a/W* and *S/W* - ratios.

The authors determined the equation (4) for nondimensional stress intensity factor with *a/W-ratio* for 4-point bend specimen with varying *a/W-ratios* [63].

$$F(a/W) = -0.2353 + 11.8397\frac{a}{W} - 69.7773(\frac{a}{W})^2 + 216.0468(\frac{a}{W})^3 - 306.6905(\frac{a}{W})^4 + 170.5374(\frac{a}{W})^5 \quad (4)$$

Similarly, by finite elements, it was determined that this expression is also valid for configuration 29(b) since the analysis carried out considers only stresses in the elastic regime. In this way it can be concluded that the relationship between P and K_I for both configurations are the same.

From equations 1 and 2 it is possible to determine the relationship between P and K_I for differents a/W.

4.4. Materials details

4.4.1. AISI 316L

The exploratory tests will initially be conducted on specimens made from AISI 316L stainless steel (ASTM A240 Grade S31603) [67], a typical chromium-nickel austenitic stainless steel supplied as 19 mm thick hot rolled plate see Figure 29. Table 3 lists the chemical composition of the tested 316L steel, with alloying elements well within the specifications of ASTM A240 [67].

Fatigue crack growth tests were performed, following the guidelines of ASTM E647 [2]. Figures 23, 24 and 25 illustrate, respectively, the specimens C(T), SE(B) with $S/W=4$, while Figure 25 shows the SE(B) with $S/W=8$ of 316L stainless steel, positioned in the testing machine MTS (Measure Test Simulate).
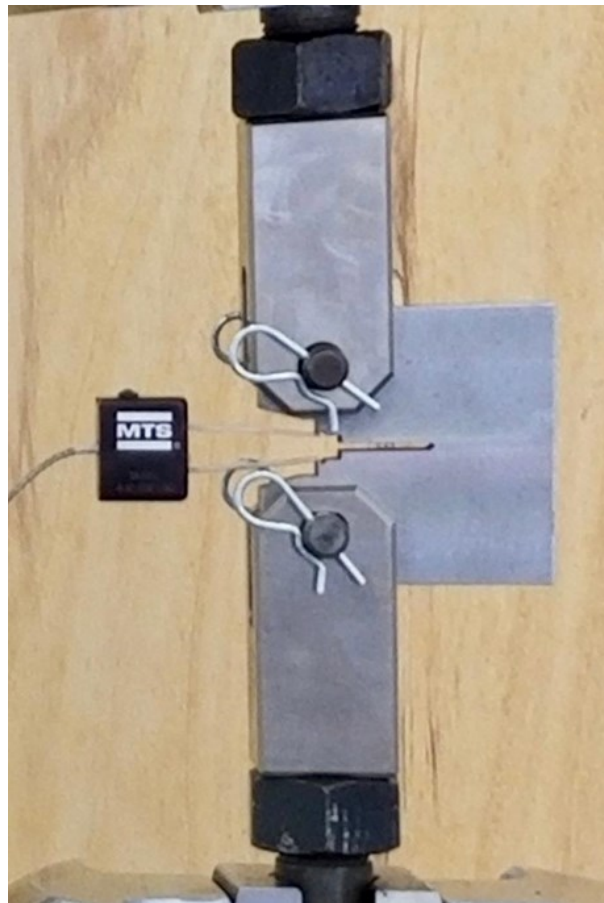
Figure 26: C(T) Specimen of AISI 316L material in the MTS machine during the fatigue crack propagation test.

Figure 27: SE(B) Specimen of AISI 316L material in the MTS machine during the fatigue crack propagation test with S/W=4.

Figure 28: SE(B) specimen of 316L stainless material in the MTS machine during the fatigue crack propagation test.

Tests were performed using a frequency of 20 Hz, load ratio, R equal to 0.1 and TL direction (the crack will propagate in the longitudinal direction). For tests on SE(B) specimens, the *S/W* ratio was equal to 4 and was to follow the methodologies presented in the chapter 3. Before the tests, according to ASTM E647 [2]. A fatigue pre-crack was performed. Its extension was 1 mm in specimens C(T) and 0.75 mm for specimens SE(B). For all C(T) specimens tested, the determination of the threshold, ΔK_{th}, (Region I) and the Paris region (Region II) of the curve *da/dN* vs ΔK, was carried out in the same specimen.

As for the SE(B) specimens, due to the low ligament, these same two regions were determined in different specimens. For the 316L stainless steel and SE(B) geometry, three (3) specimens were used, all of which were used to determine the threshold.

To calculate the loads and the voltage intensity factor, the equations of the ASTM E647 [2] standards for the C(T) specimen and the SE(B) specimen were used as reference ASMT E1820 standard [39].

Finally, it is important to note that for the determination of the "Threshold" the decreasing ΔK mode (ΔK control) was used, while for Region II (Paris) [2] the methodology used was the constant load (constant ΔP - Constant Amplitude Load).
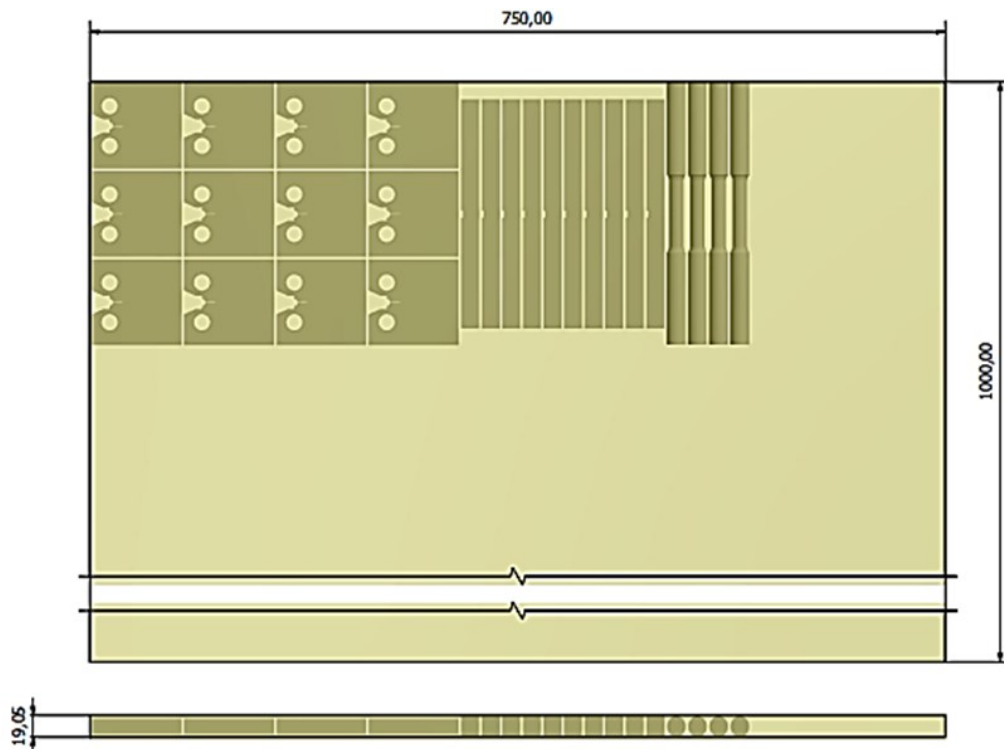
Figure 29: Plate from which the test specimens were extracted.

46

Table 3: Chemical Composition of Tested AISI 316L Stainless Steel (% weight)

C	Mn	Cr	Ni	Mo	N	Cu	Nb	V	W	Si	P	S
0.019	1.33	16.6	10.0	2.1	0.038	0.245	0.021	0.054	0.036	0.44	0.039	0.002

Metallographic analysis of the etched surface of the tested 316L austenitic stainless steel, shown in Figure 30 (a), revealed an expected microstructure consisting of equiaxed austenite grains with annealing twins. The annealing twins formed from transformations in the crystal system during cooling.
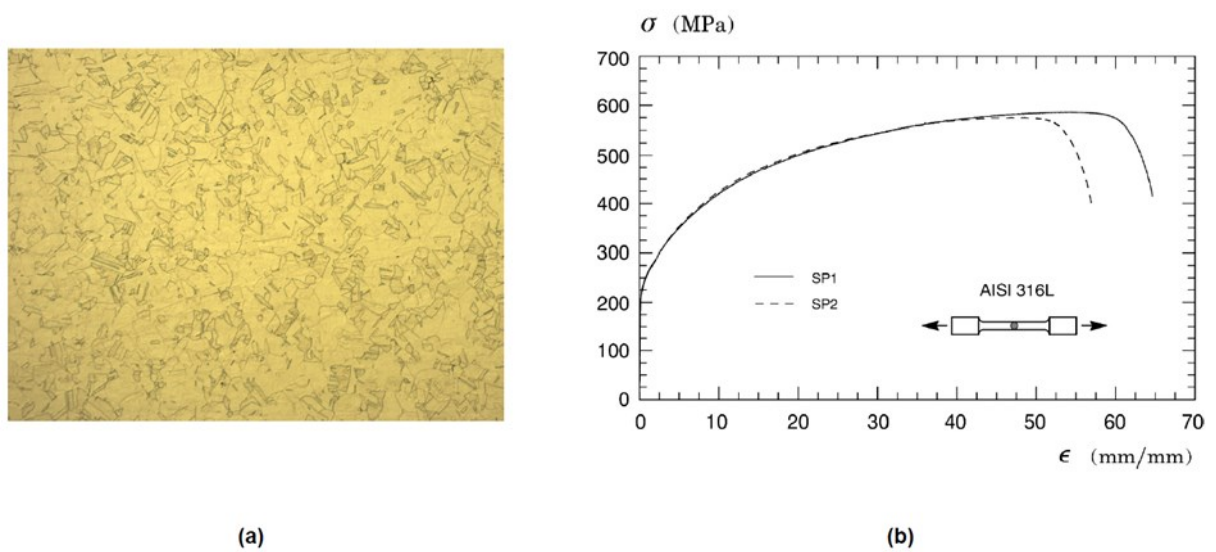
Figure 30: (a) Representative microstructure of the tested AISI 316L chromium-nickel austenitic stainless steel (Etching: Nital 2%. Magnification: 50x). (b) Engineering stress-strain curves measured at room temperature for the tested material [30].

Mechanical tension tests at room temperature (20°C) per ASTM E8M [68] utilized transverse round specimens (diameter 12.5 mm) extracted from the plate. The 316L steel displays a yield strength σ_{ys} = 228 MPa and ultimate tensile strength σ_{uts} = 584 MPa (average of two tests), evidencing high strain hardening given the σ_{uts}/σ_{ys} ratio ~2.6. Fitting the true stress-true strain curve to the Ramberg-Osgood power law per API 579 [69] gives exponent n = 4.1.(see Figure 30 (b)).

4.4.1.1.   Specimen Geometries

Fatigue crack growth (FCG) tests were conducted at room temperature on standard compact tension C(T) specimens, as shown in Figure 34 (a), to characterize near-threshold fatigue crack growth rate (da/dN) and corresponding stress intensity factor

range ΔK_{th}. The C(T) specimens have width W = 63 mm, thickness B = 12 mm and an initial crack length to width ratio (a0/W) of 0.2. Additional FCG tests utilized single edge notched bend SE(B) specimens with (a_0/W) = 0.2, B = 16 mm, W = 16 mm and two span lengths S: a standard 4W span and a non-standard 8W span previously used in fracture toughness tests [63], [70]. The increased 8W span provides higher crack tip constraint, mitigating effects of crack tip plasticity often encountered in smaller specimens.

Figures 31, 32 and 33 depict the geometry and dimensions of the 316L stainless steel specimens intended for use in both tensile and fatigue crack propagation tests.
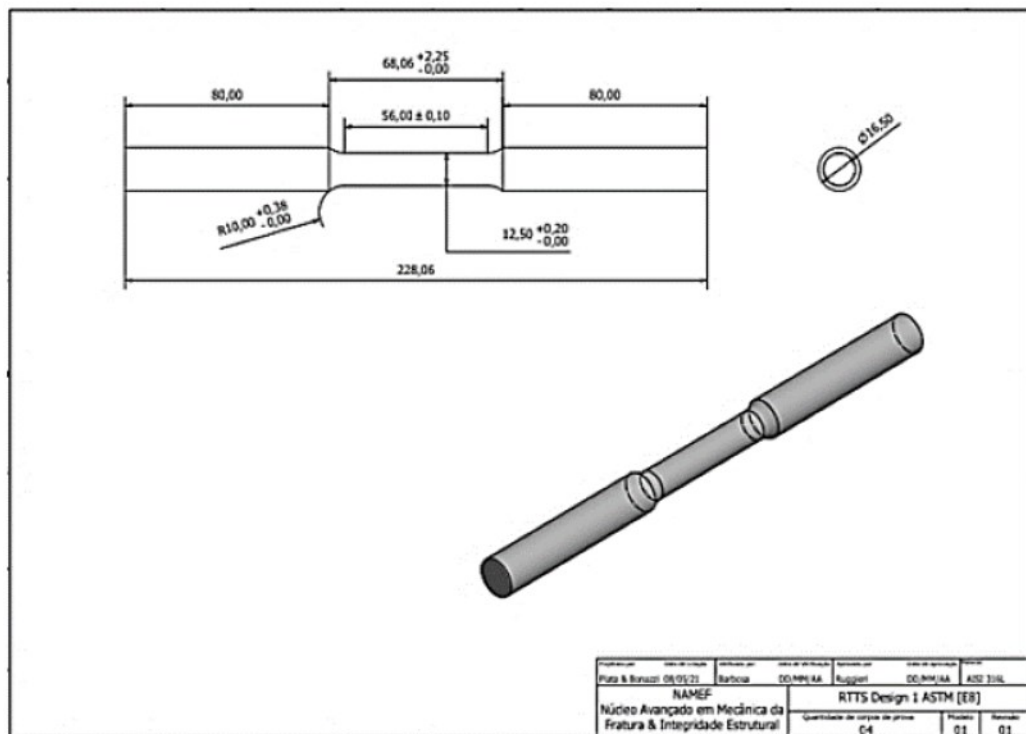
Figure 31: Geometry and dimensions of the 316L stainless steel material tensile test specimen.
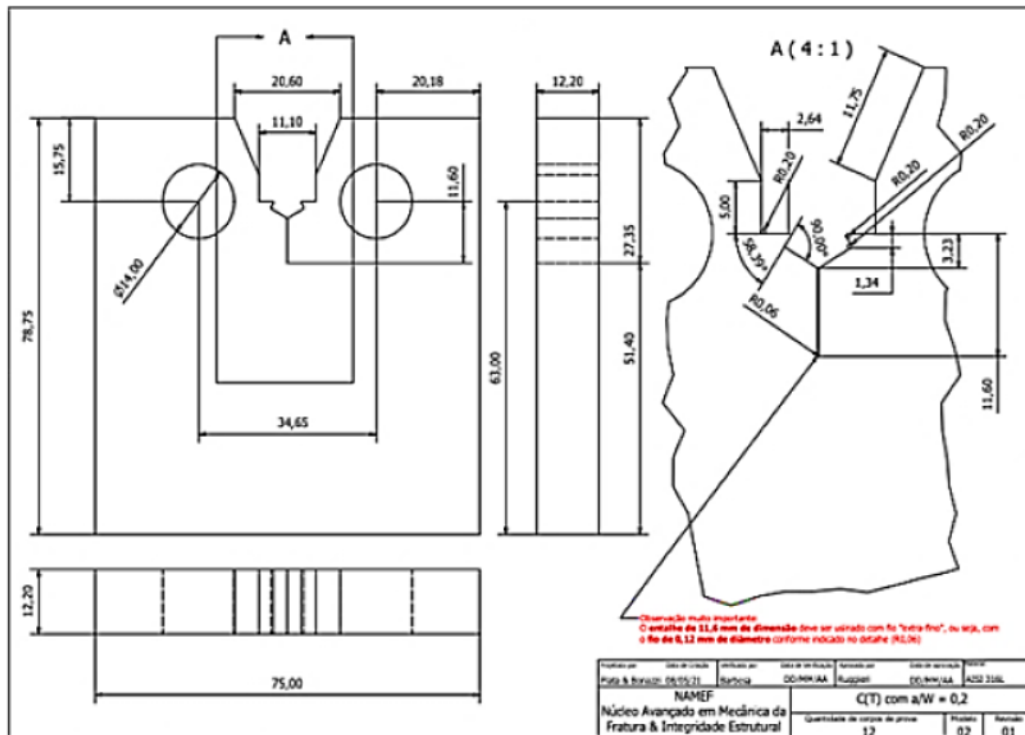
Figure 32: Geometry and dimensions of the specimen C(T) of 316L stainless steel material.
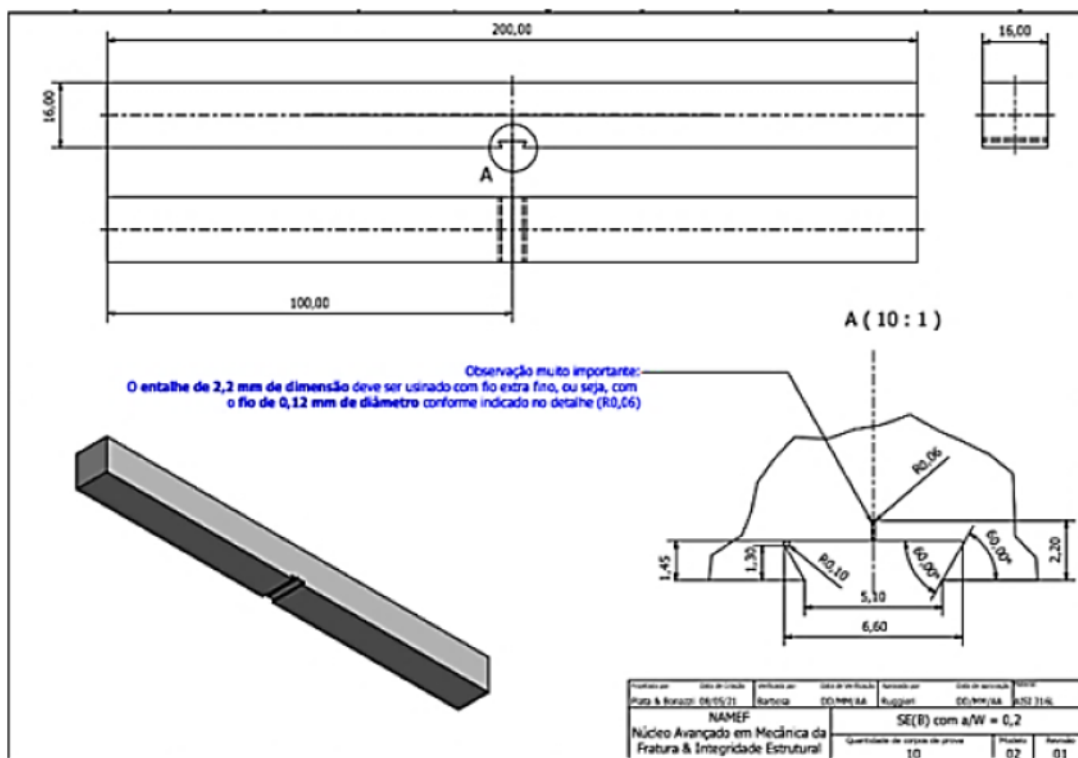
Figure 33: Geometry and dimensions of the SE(B) specimen of stainless steel 316L material.

Figure 34 (a, b) schematically illustrates the arrangement of rollers for the execution of experimental tests. Given the development of a specific testing procedure, there are non-standard steps incorporated into the proposed experimental approach. However, certain guidelines outlined in the ASTM E647 standard [2] served as a foundational reference for the tests.

(a)   (b)
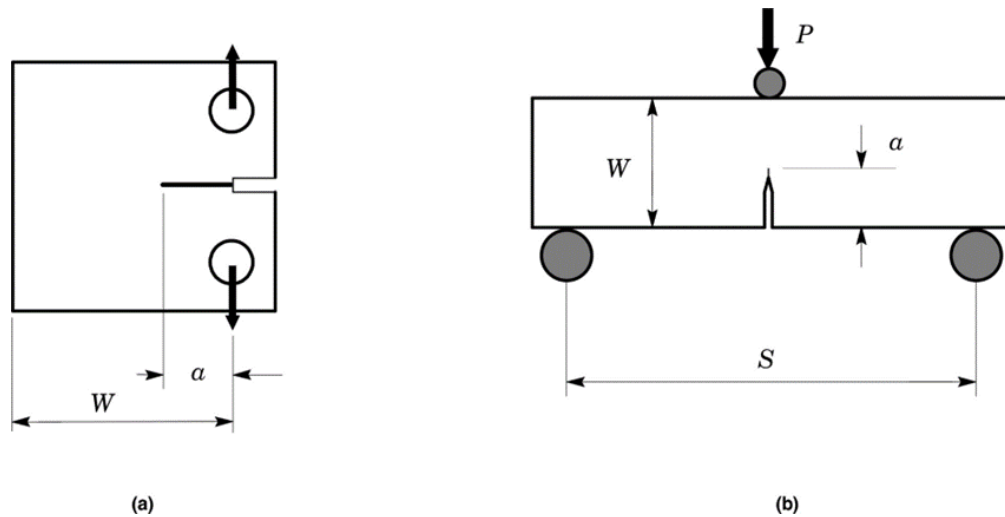
Figure 34: (a) C(T) geometry and (b) SE(B) schematic drawing of the positioning of the rollers for carrying out the tests in 3 points.

4.4.2. INCONEL 625 Girth Weld

Following the completion of tests on stainless steel, we proceeded to extract test specimens featuring SE(B) geometry from a clad-welded pipe as see in Figure 35. The utilization of this specific geometry enables the machining of test specimens with a primary focus on the weld region. Notably, the notches are strategically positioned at the reinforcement to the root and from the root to the reinforcement. This approach is adopted to implement methodologies that have been previously validated with the 316L material.
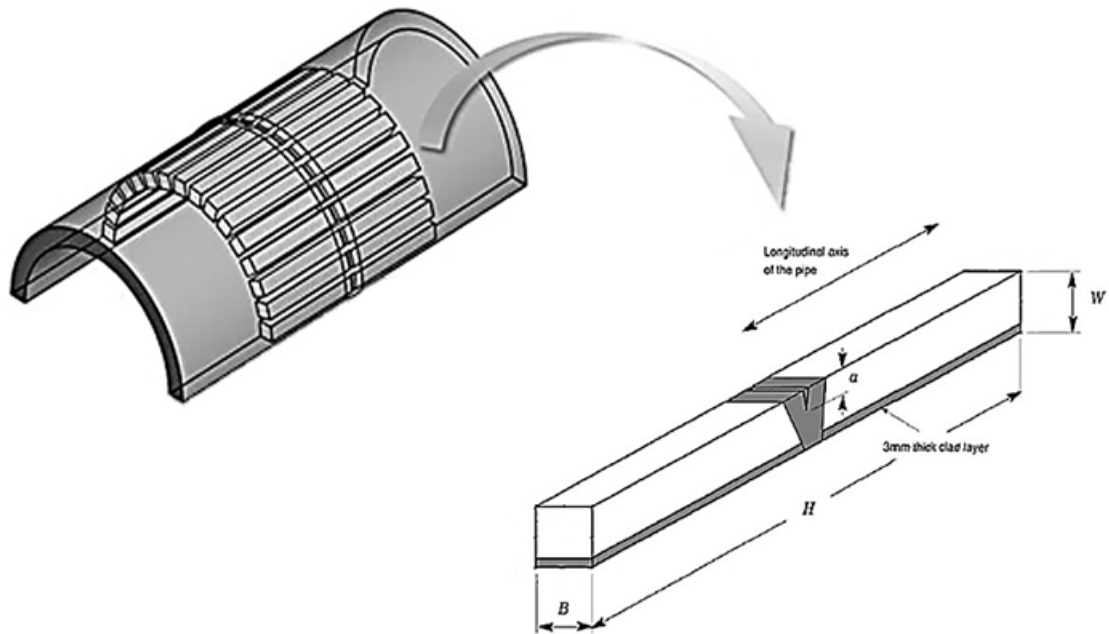
Figure 35: SE(B) specimen extracted from the bimetallic pipe.

The final material examined in this study was a girth weld from an 8-inch (203 mm outside diameter), API 5L Grade X65 pipe. The pipe had a total wall thickness (tw) of 17 mm, including a 3 mm thick internal cladding of ASTM UNS N06625 alloy 625 per ASTM B443 [71] and ASTM B444 [72]. The pipe's girth weld was made using gas metal arc welding (GMAW) in a single V-groove configuration. Table 2 provides the key GMAW parameters used to produce the multi-pass test weld. Five passes filled the groove.

Table 4: Welding Procedure Specification.

Parameter Control of Pulsed MIG/MAG Passes							
Weld Pass	Peak Current (A)	Time (s)	Background Current (A)	Time (s)	Welding Speed (cm/min)	Heat Input (kJ/min)	Depth of Pass
Root	300	2.2	90	4.4	48	0.49	15
P2	300	2.2	90	4.4	40	0.59	12.7
P3	300	2.2	90	4.4	35	0.67	9.6

P4	300	2.2	90	4.4	30	0.78	4.0
P5	300	2.2	90	4.4	25	0.94	2.3

The nickel-chromium alloy corresponding to ASTM UNS N06625 alloy 625 [ASTM B443 (2019) [71] and ASTM B444 (2018) [72] was used to make the girth weld to match the mechanical properties of the internal cladding and join the two materials.

Tables 5, 6 and 7 show, respectively, the chemical composition of the base metal, liner and weld. It is worth noting that the chemical analysis was performed via ICP-OES (Inductively Coupled Plasma - Optical Emission Spectrometry). Figure 36 shows the regions/locations where the chemical and metallographic analyses were performed.
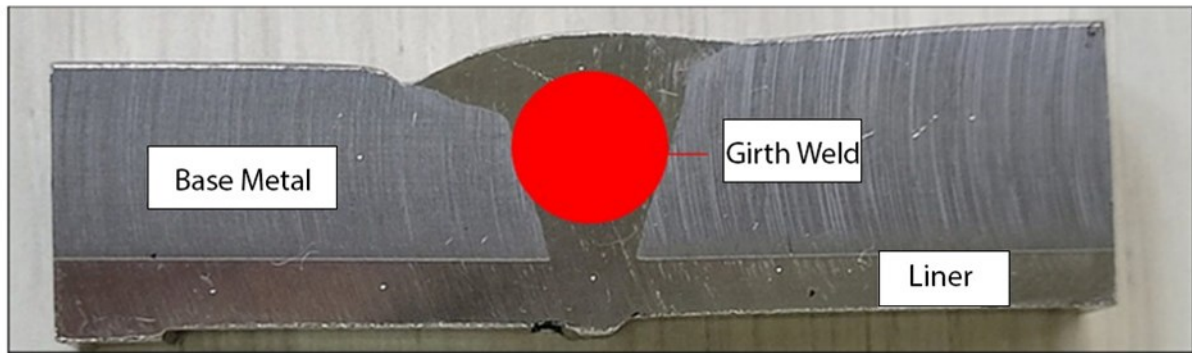
Figure 36: Weld region where the sample extractions were performed for the tensile test specimens.

C	Mn	Si	Al	Cu	V	Mo	Cr	Ni	P	S	Fe	CE
0.111	1.329	0.432	0.025	0.146	0.056	0.080	0.023	0.253	0.013	0.0028	Bal.	0.391

The carbon equivalent calculation was performed using Equation (5).

$$CE = \%C + \frac{\%Mn}{6} + \frac{\%Cr + \%Mo + \%V}{5} + \frac{\%Ni + \%Cu}{15} \quad (5)$$

Table 5: Chemical composition of tested ASTM UNS N06625 alloy 625 liner (% by weight).

C	Mn	Si	Cr	Nb+Ta	Co	Mo	Fe	Al	Ti	Ni	P	S
0.020	0.057	0.075	22.53	3.790	0.012	7.772	2.598	0.161	0.203	62.32	0.0032	<0.0050

Metallographic analysis confirmed the pipe's base metal was normalized and tempered API 5L Grade X65 low carbon steel. As Figure 37(a-c) shows, the etched base metal microstructure contained elongated ferrite grains with precipitated carbides, as expected.

The chemical composition analysis verified the liner was ASTM UNS N06625 alloy 625 nickel superalloy, with all elemental concentrations within specifications. The weld filler material was also identified as the nickel superalloy alloy 625.

(a)

53
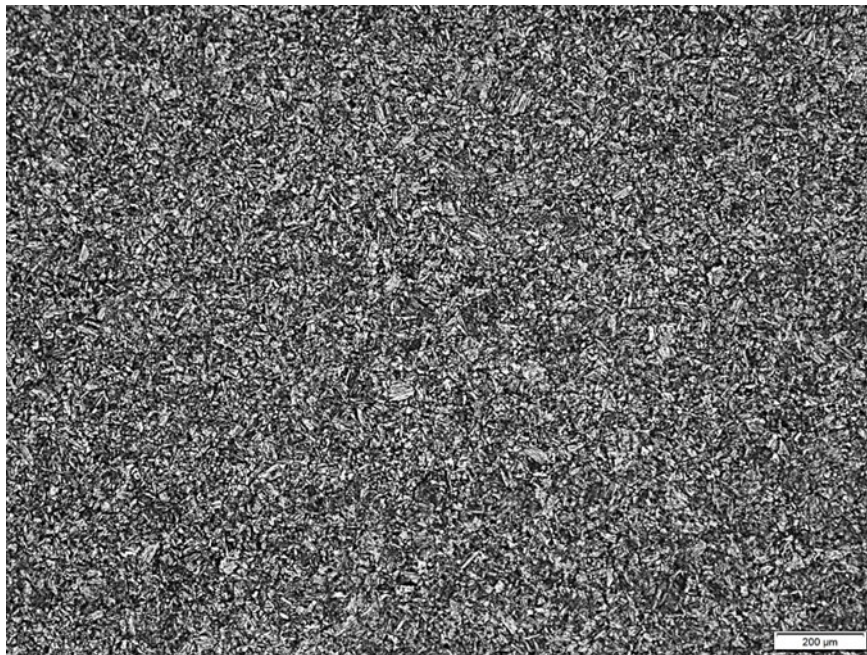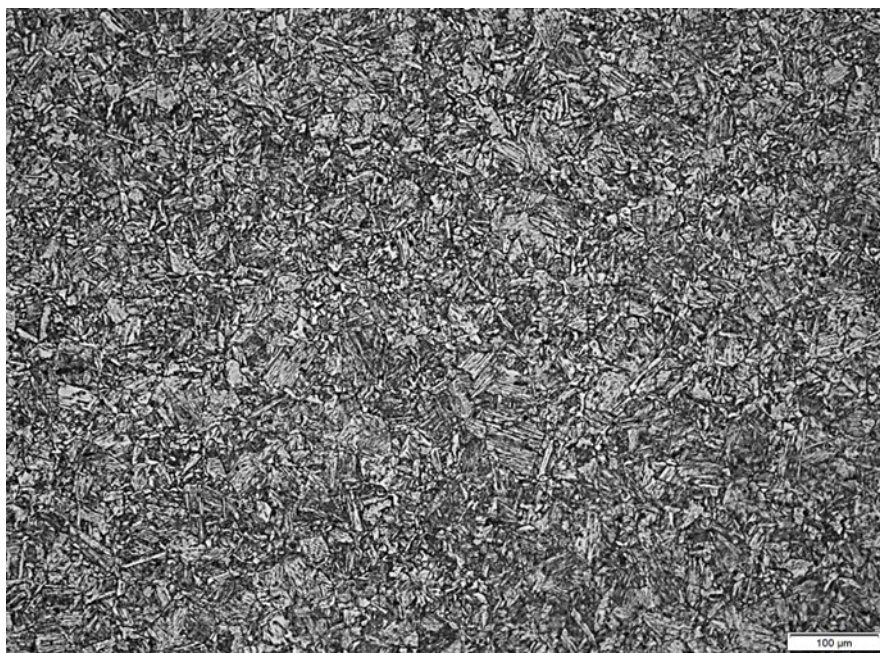
(b)

(c)

Figure 37: Representative microstructure of API 5L Grade X65 base metal (Etchant: 5% Nital). Magnification: (a) 100x, (b) 200x and (c) 500x.

Figure 38 (a-i) shows the metallographic analysis of the etched surface of the heat-affected zone (HAZ) at various magnifications. The images reveal both the transition area between the base metal (BM) and the HAZ and the interface between the HAZ and the fused weld metal zone. Observing these allows examination of the microstructural changes that occur across these regions due to the thermal cycle of the welding process.
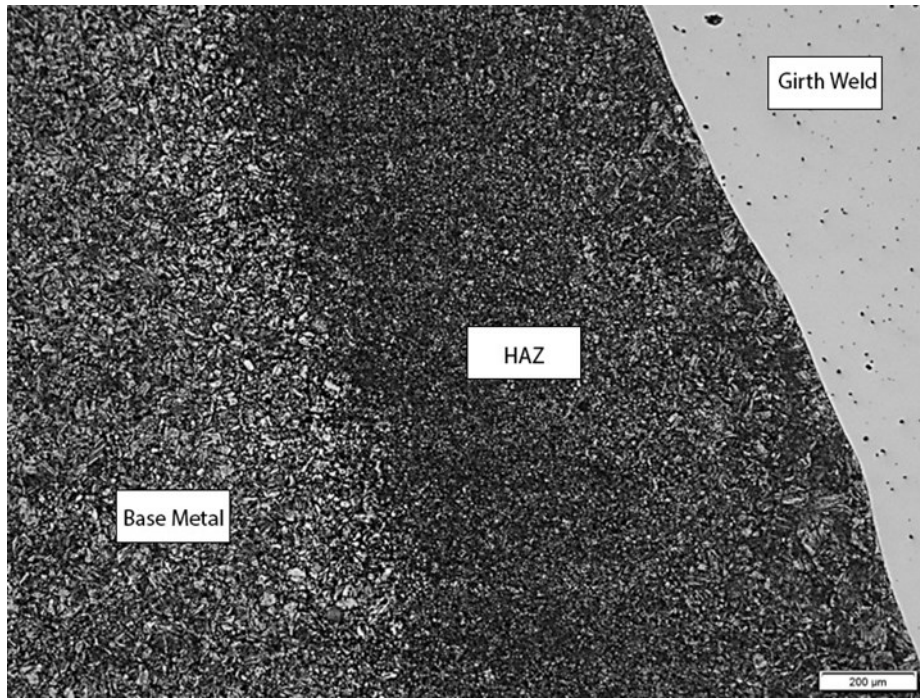
(a)
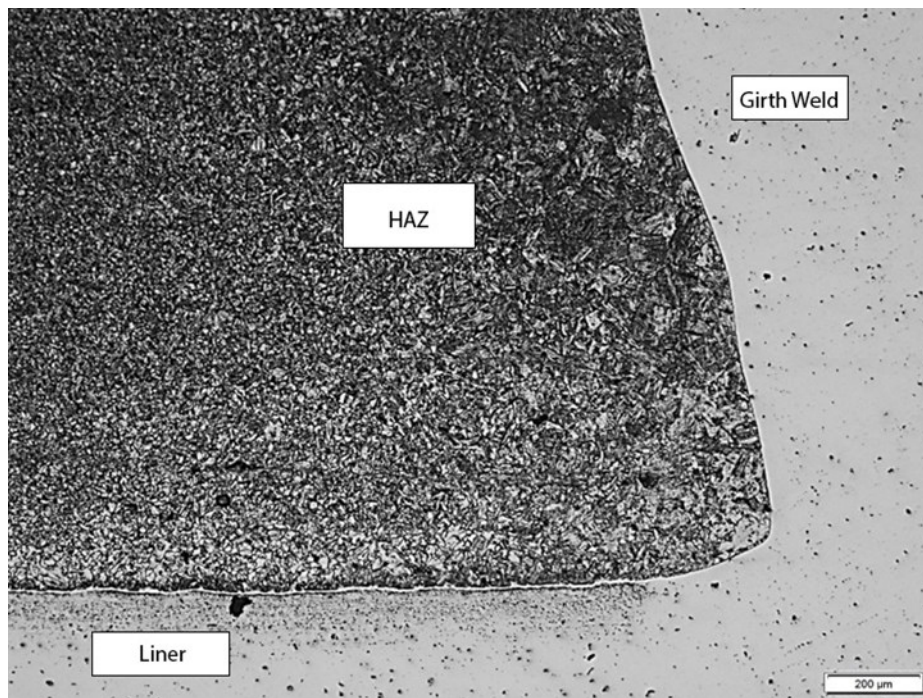
(b)
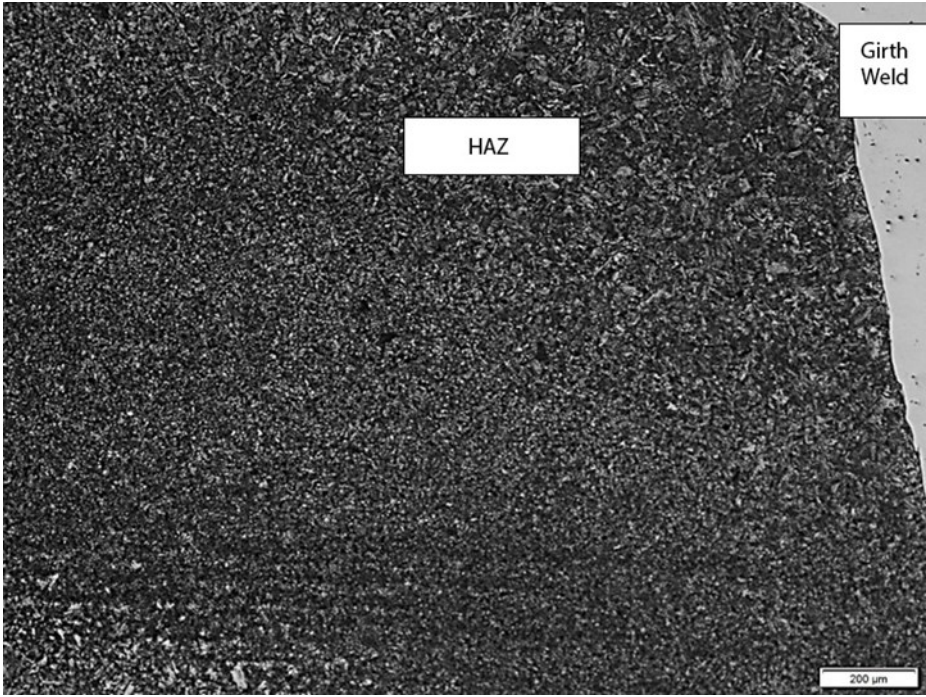
(c)
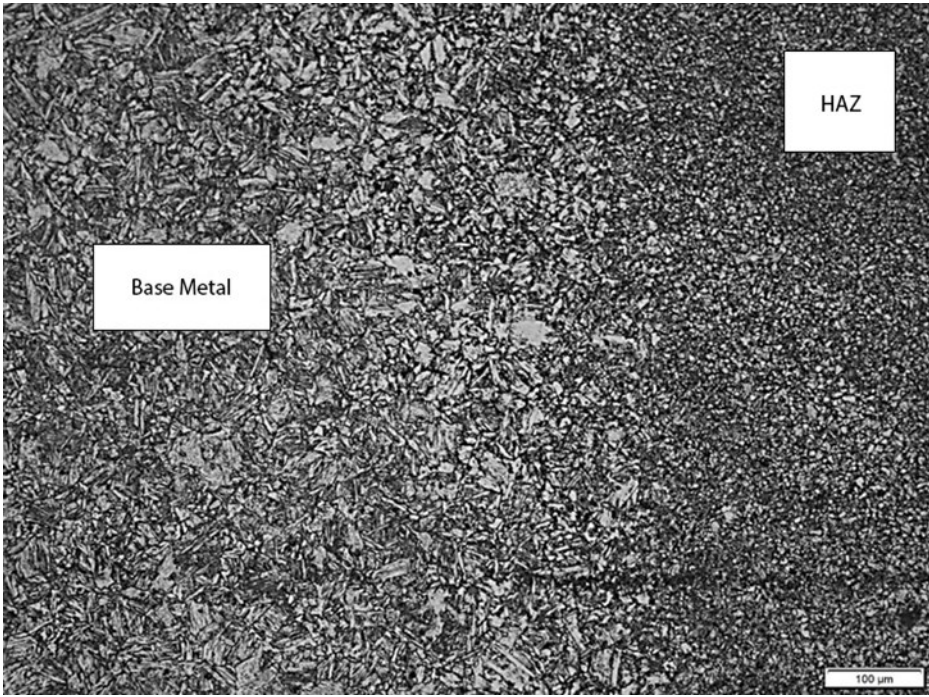
(d)
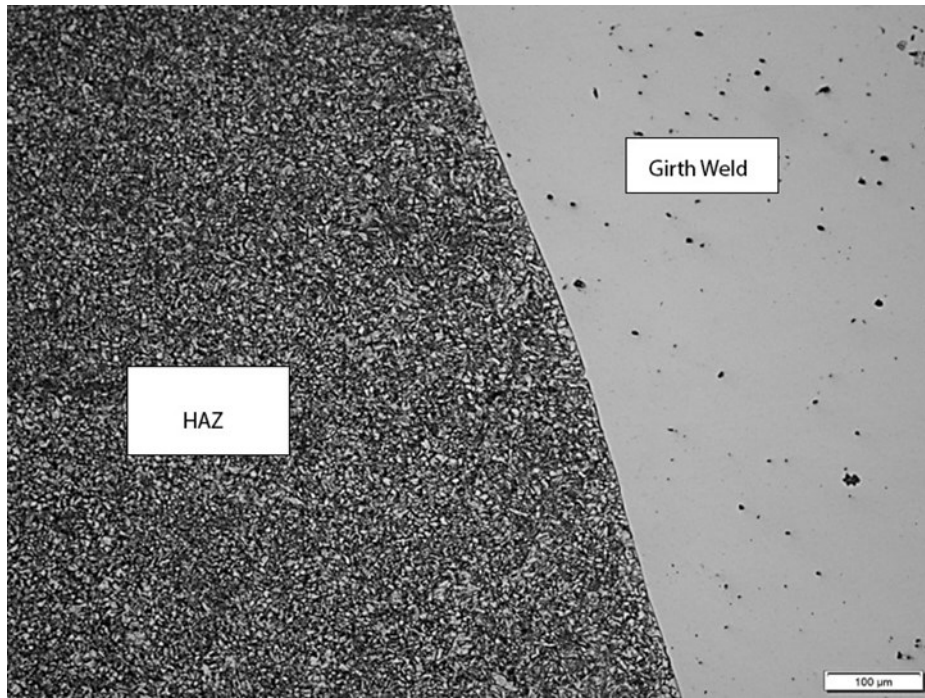
(e)
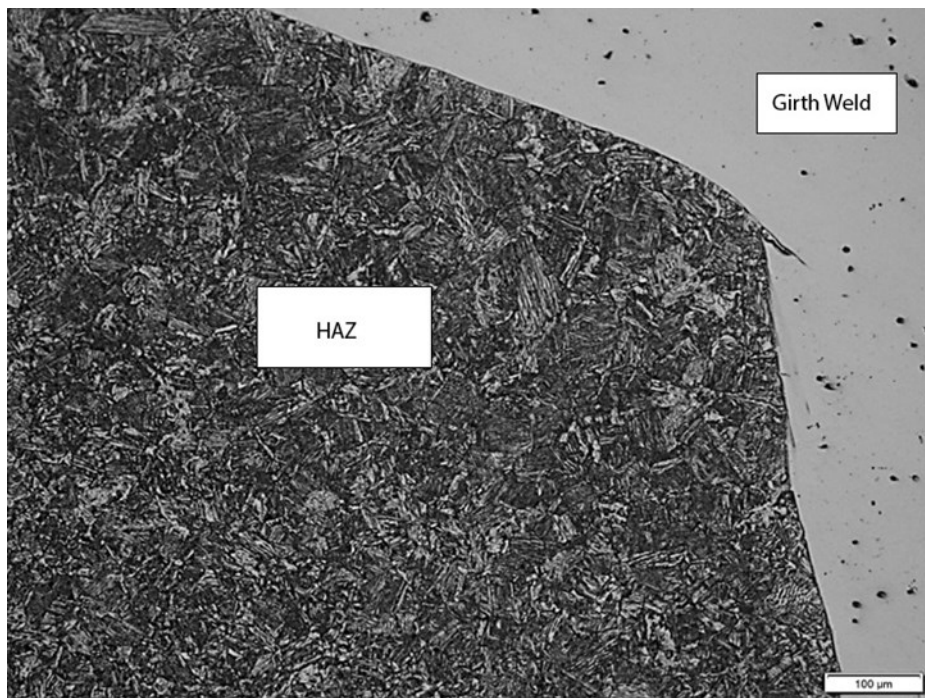
(f)
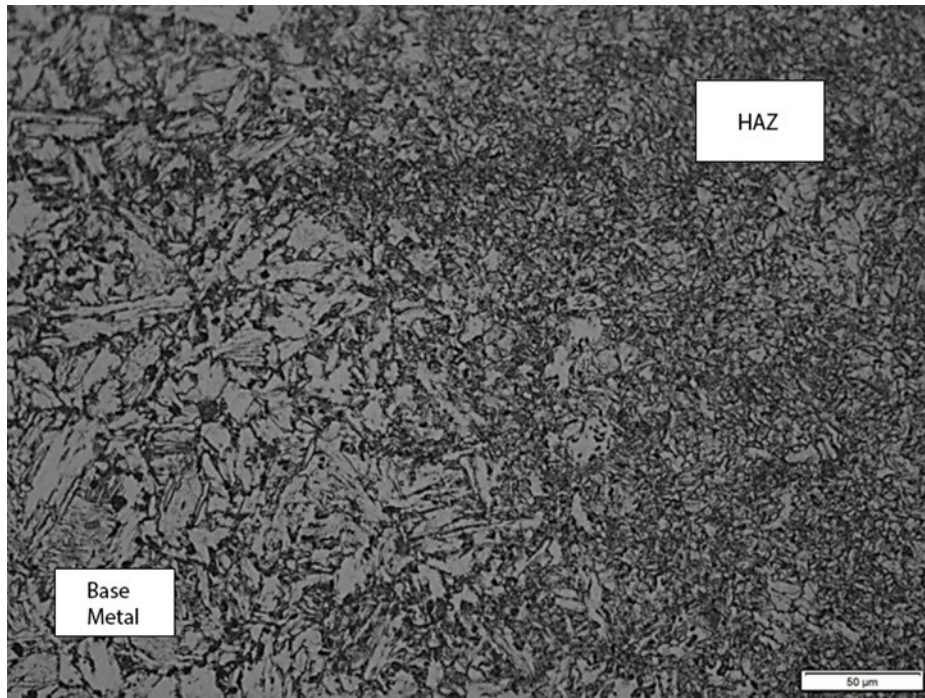
(g)
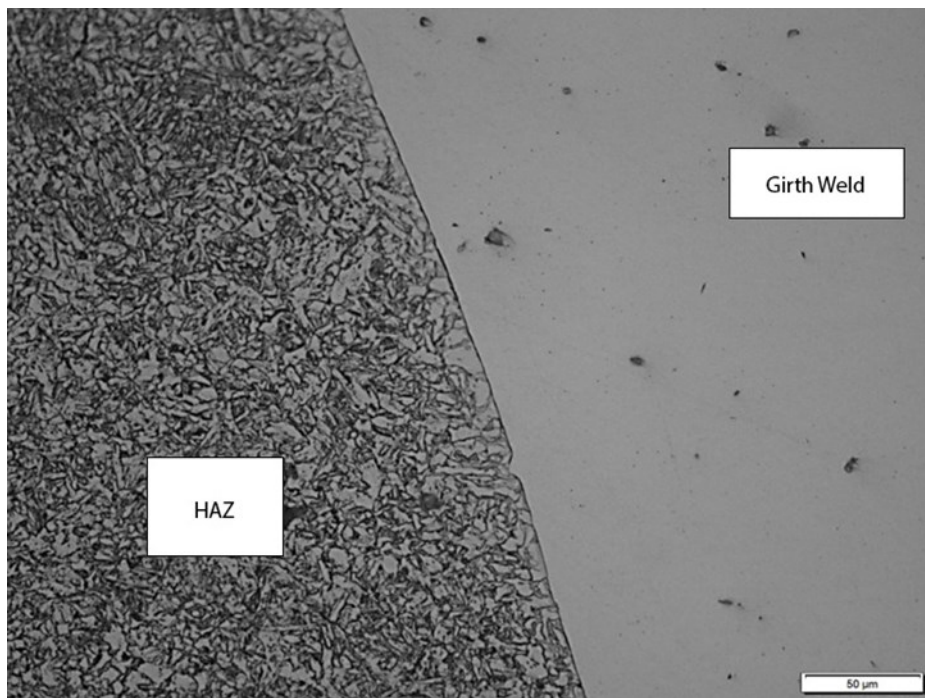
(h)
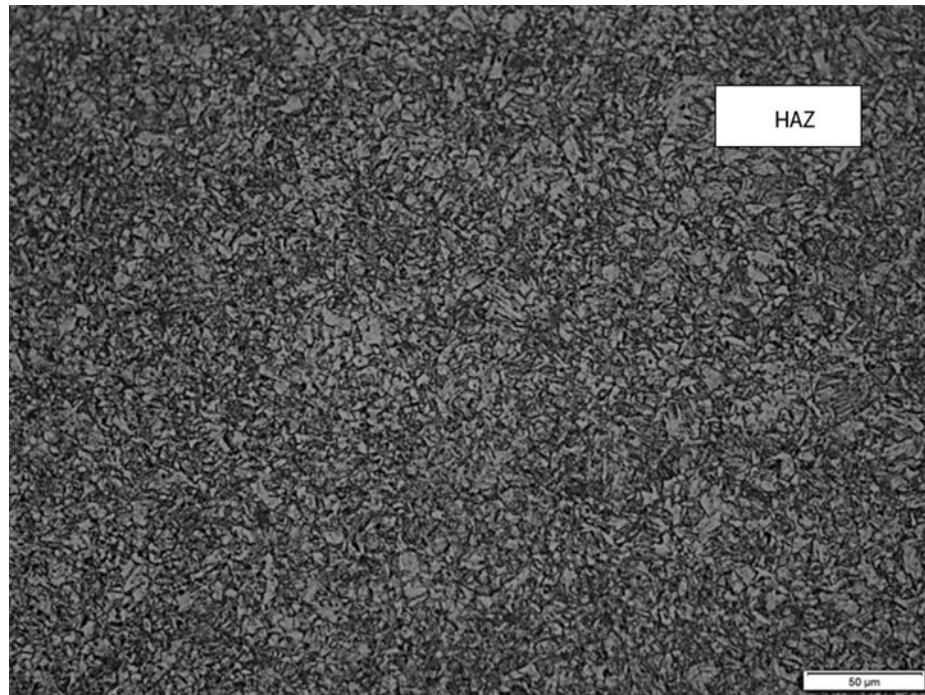
(i)

Figure 38: Representative microstructure of the HAZ (Etchant: 5% Nital). Magnifications: (a), (b) and (c) 100x, (d), (e) and (f) 200x and (g), (h) and (i) 500x

From Figure 38 reveals that the metallographic analysis of the etched ZTA surface showed a more refined microstructure, still consisting of an elongated ferrite phase with internal carbide precipitation.

Figure 39 (a-e) displays the metallographic analysis of the etched weld region surface at different magnifications.
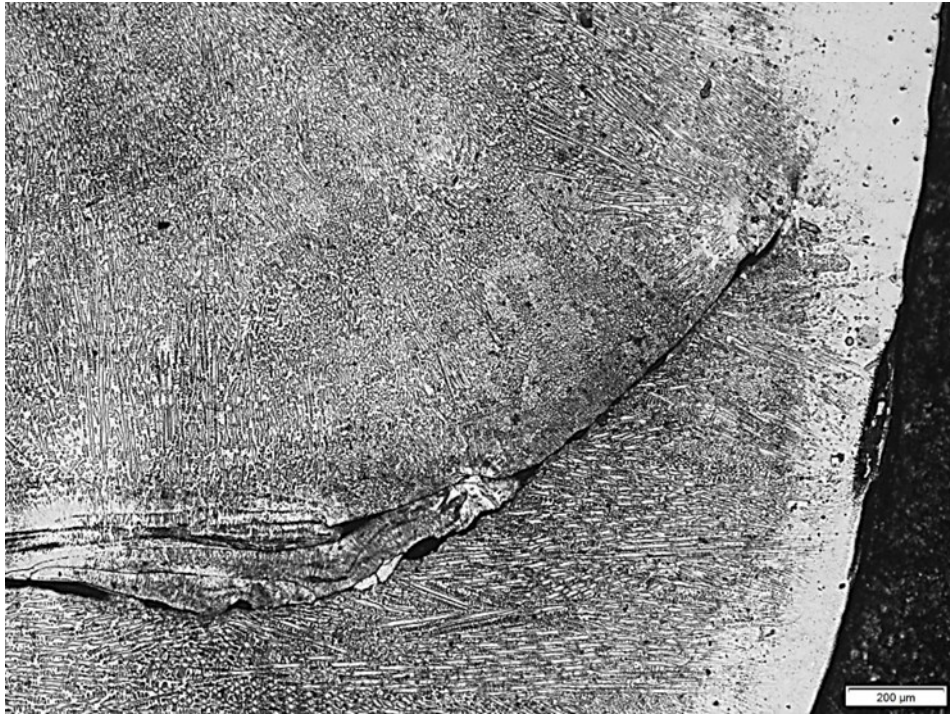
(a)
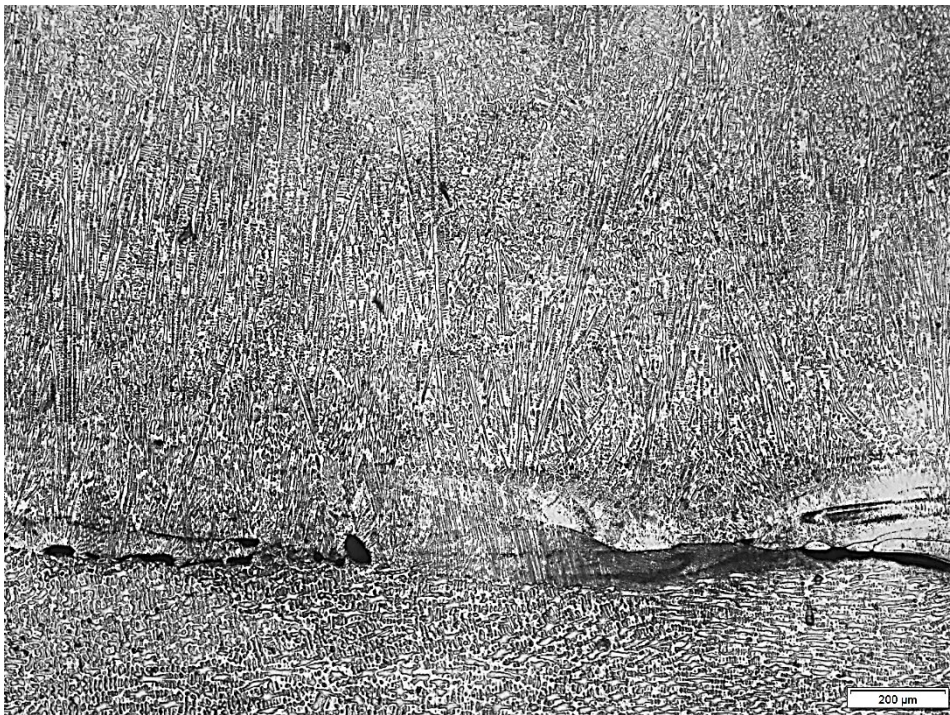
(b)
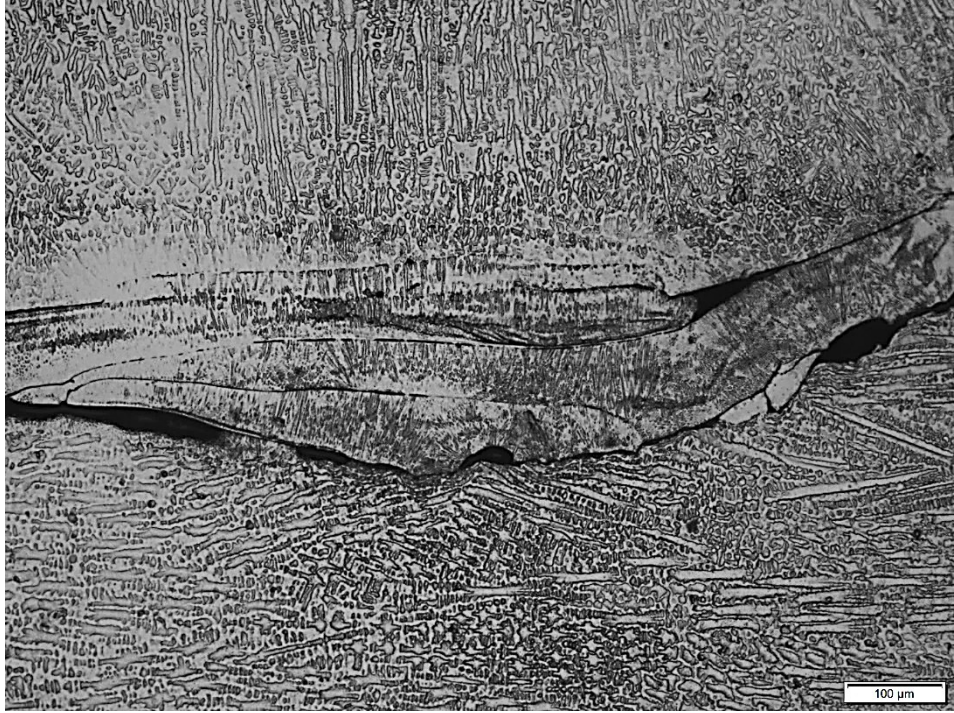
(c)
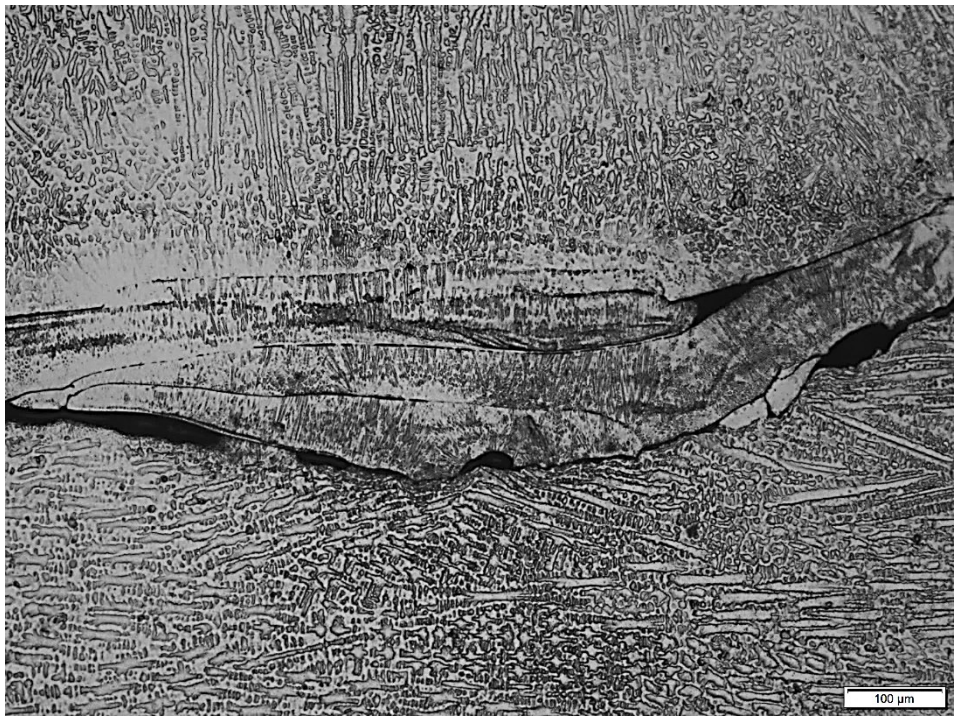
(d)
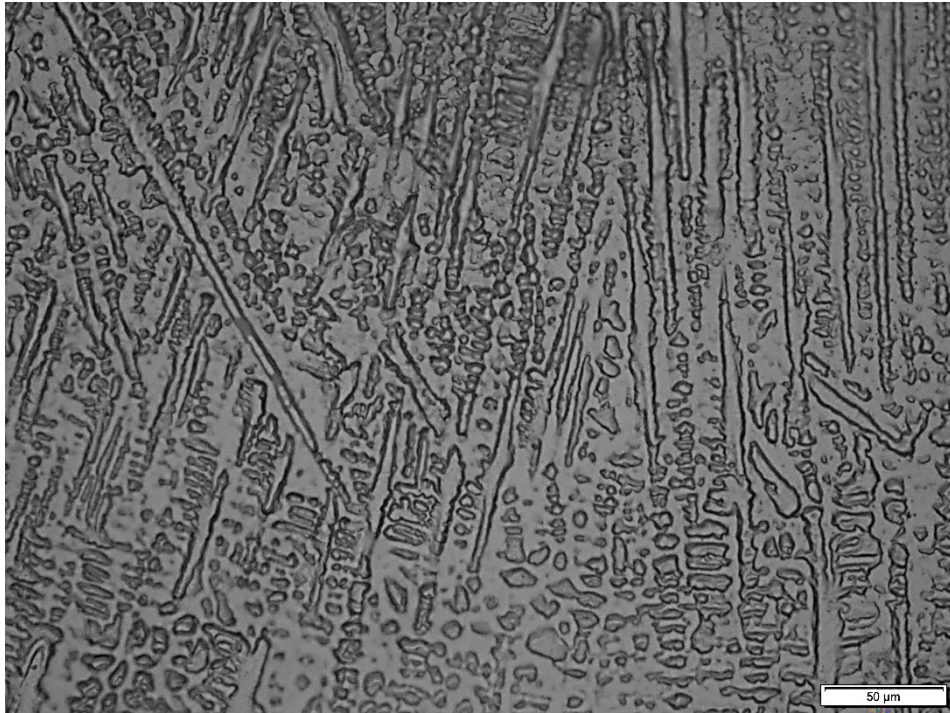
(e)

Figure 39: Representative microstructure of the weld region (Etchant: Aqua Regia). Magnification: (a) and (b) 100x, (c) and (d) 200x and (e) 500x.

Figure 39's metallographic analysis of the etched weld surface reveals a characteristic dendritic weld microstructure, consisting of austenite dendrites formed by rapid cooling. Notably, an identical microstructure was observed in the weld root. It is also possible to see fusion defects in this micrograph.

Finally, Figures 40 (a-b) exhibit the base metal and liner interface microstructure.
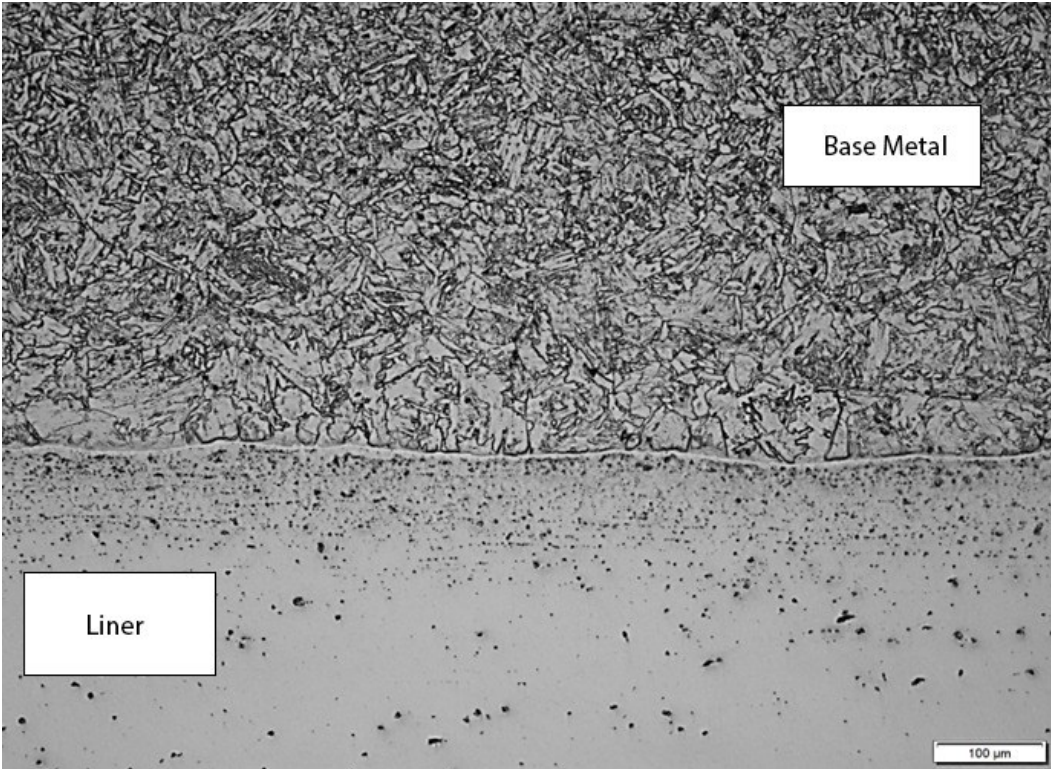
(a)
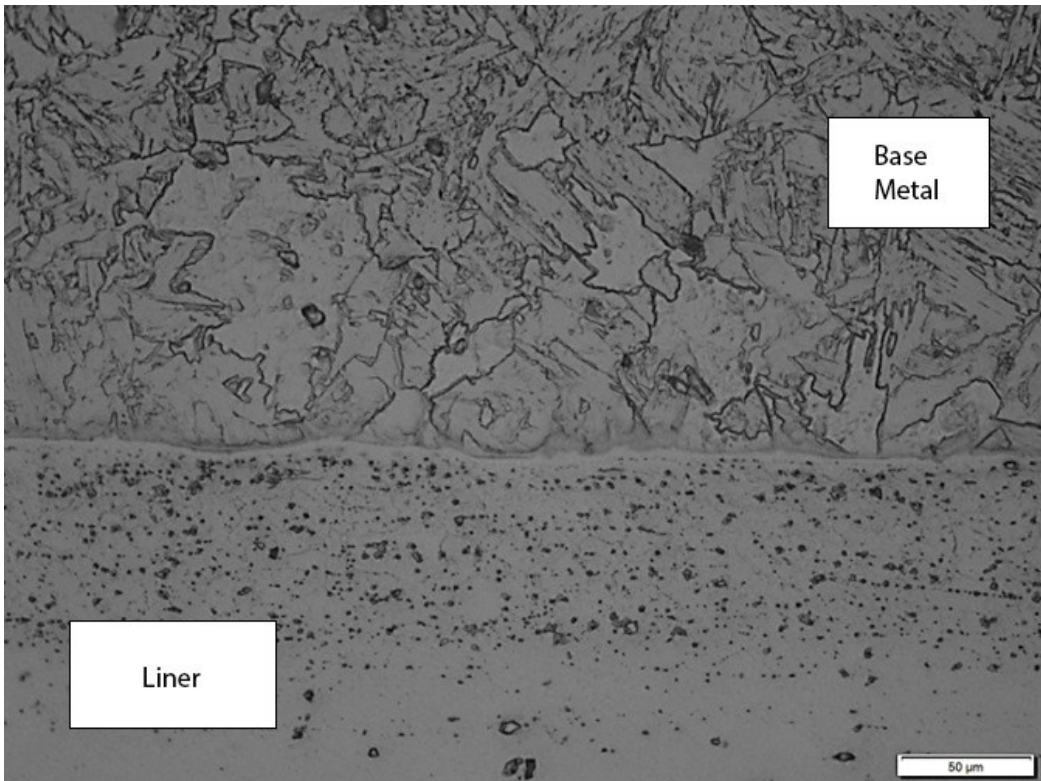
(b)

Figure 40: Representative microstructure of the interface between the liner region and the base metal (Etchant: 5% Nital). Magnification: (a) 200x and (b) 500x.

Figure 40 reveals the base metal microstructure at the interface consists of ferrite and carbide precipitates. However, the ferrite exhibits a coarser morphology, possibly due to temperature exposure. Although unetched, the Inconel liner region would display an austenitic structure with some dispersed carbide precipitates.

Per ASTM E8M [68], room temperature tensile tests were conducted on standardized transverse base metal specimens (9.0 mm diameter). The average base metal yield and tensile strengths over four tests were σ_{ys} = 625 MPa and σ_{uts} = 716 MPa, respectively, with a 0.87 elastic ratio (Figure 41).

Figure 42 presents the engineering stress-strain curves for the three weld specimens, while Table 6 summarizes their mechanical properties.
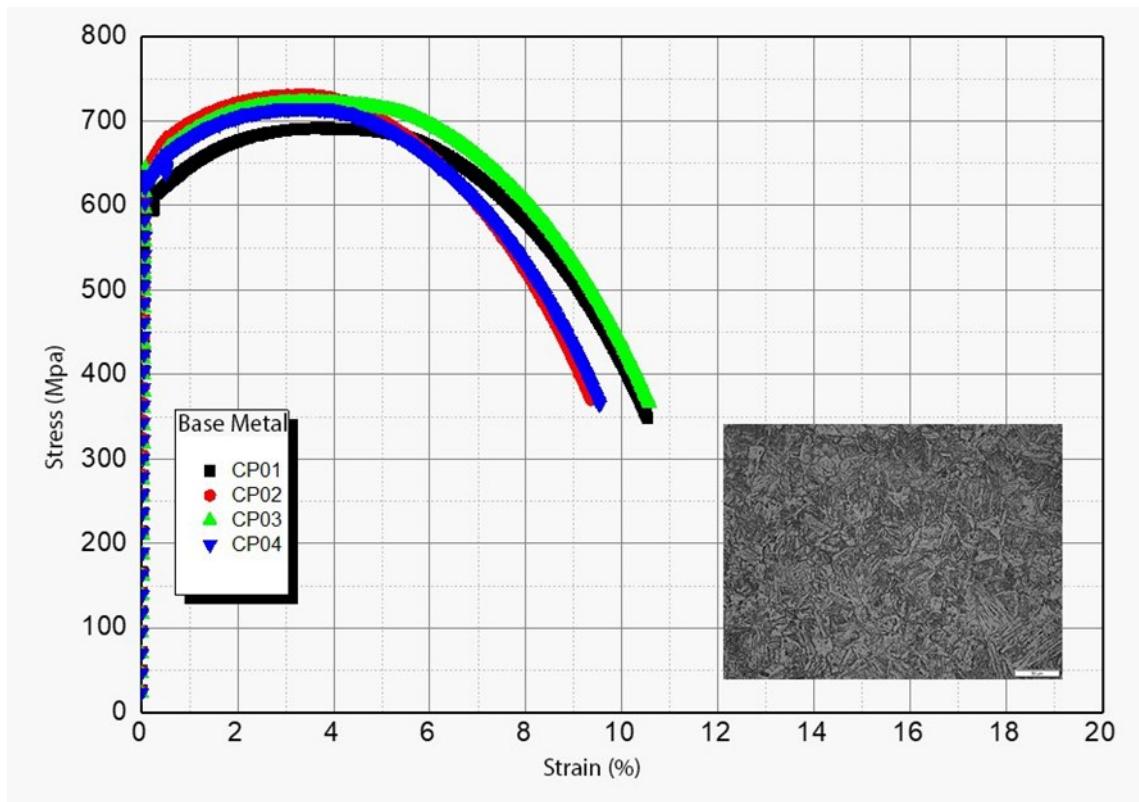
Figure 41: Engineering stress-strain curves measured at room temperature for the API 5L Grade X65 base metal.
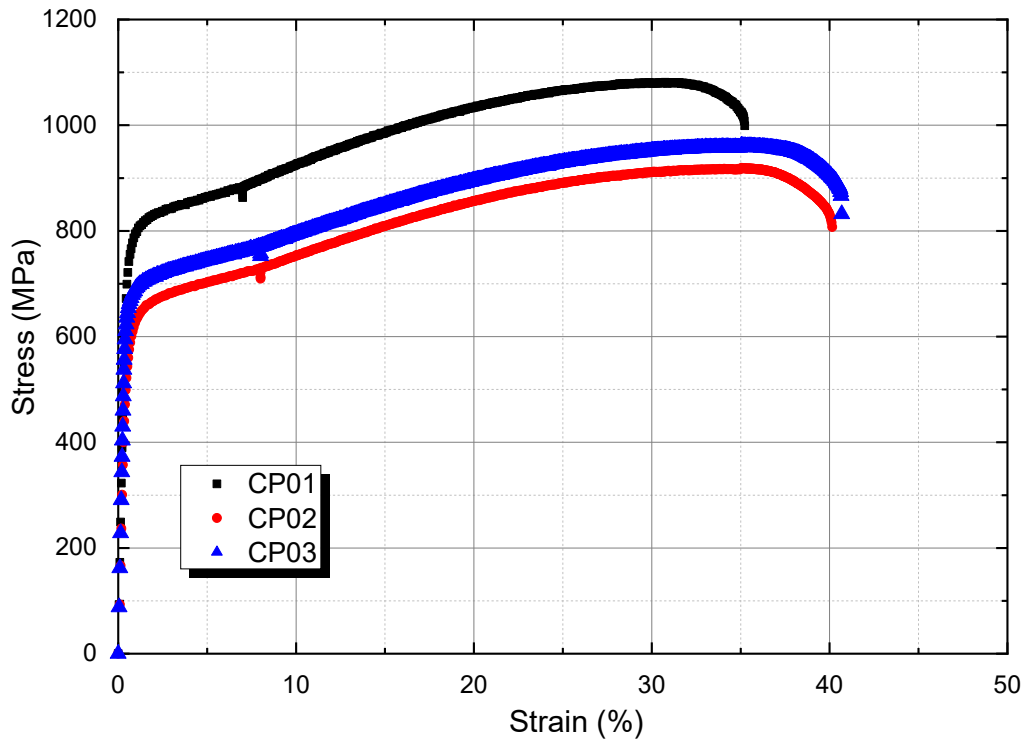
Figure 42: Engineering stress-strain curves measured at room temperature for the weld material, INCONEL 625.

Table 6: Weld Mechanical Properties.

Specimen Identification	Mechanical Properties		
	Tensile Strength (MPa)	Yield Strength (MPa)	Elongation (%)
CP01	1081.11	≈ 750.00	35.72
CP02	919.31	≈ 595.0	40.15
CP03	961.34	≈ 660.00	40.69
Mean	**987.25**	**668.33**	**38.85**
Standard deviation	**83.95**	**77.84**	**2.73**

4.4.2.1. Specimen Geometries

In this set of tests, were machined 10 SE(B) specimens with notches positioned at the reinforcement, 6 SE(B) specimens with notches located at the root and an additional 4 specimens specifically designated for conducting tensile tests see Figure 44. In Figure 43 (a), it is possible to observe the semicircular pipe from which the test specimens were extracted.
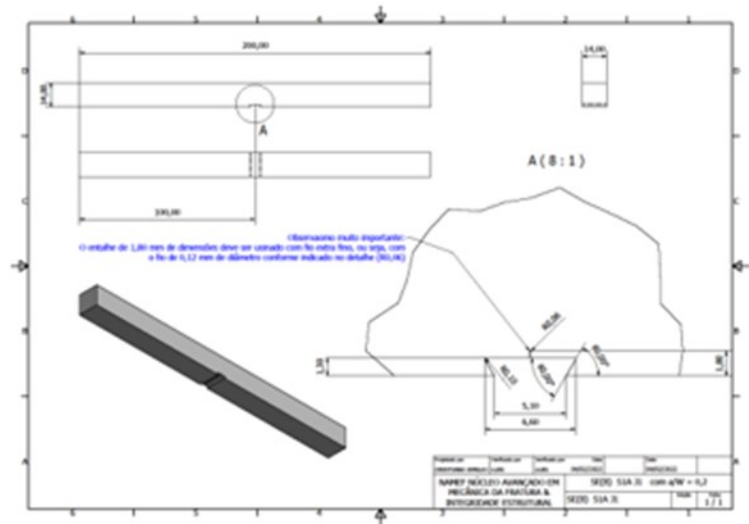
Figure 43: (a) Pipe from which the SE(B) test specimens were extracted and their (b) respective dimensions.

For mechanical tension tests, the machining of specimens was carried out with the dimensions depicted in Figure 43 (b) exhibit width W = 14 mm, thickness B = 14 mm and an initial crack length, a_0, for width ratio defined by a_0/W = 0.2. Due to its complexity, the machining was done with smaller dimensions compared to those made with the 316L material. Figure 45 illustrates the specific shape from which the test specimens were extracted.
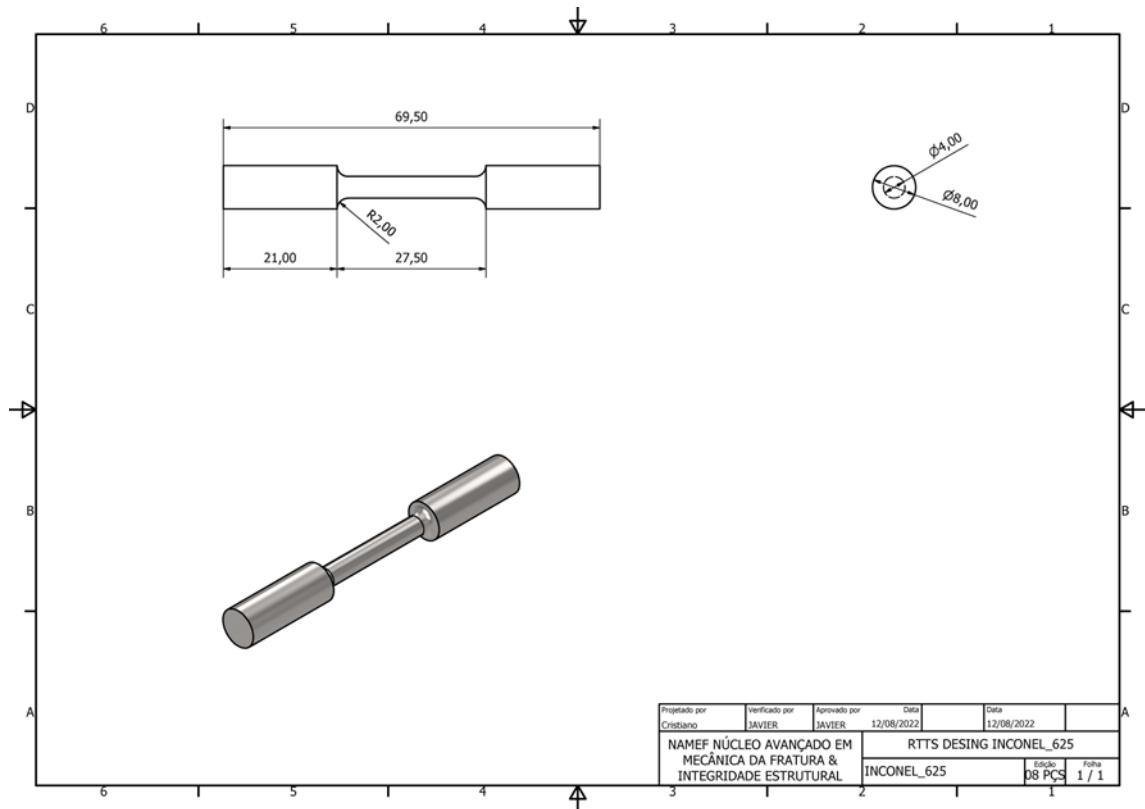
Figure 44: Geometry dimensions INCONEL 625 designated for conducting tensile tests.

Figure 45: Specific shape where were machined the specimens for tensile tests.

Table 7 consolidates essential information pertaining to the origin and geometric dimensions of specimens utilized in the exploratory tests. This includes details such as section geometry, thickness and the dimensionless length of cracks.

Table 7: Details about geometric dimensions of bimetallic pipe.

Origin	Geometry	Section (mm)	a/W	Number of spms	Determined Region/Technique
Bimetallic Pipe (API X65, CRA)	SE(B)	(BXB) 14 x 14	0.2	10	*Threshold – E647 (S/W=8) – R = 0.5*
	SE(B)	(BXB) 14 x 14	0.2	10	*Threshold –CPLR(S/W=8) – R = 0.5*

Based on the extensive experimental data available for AISI 316L stainless steel, it was determined that fatigue crack propagation testing of the joint material should be conducted under select conditions considered most relevant to the current study. Specifically, FCG tests were performed per ASTM E647 [2] using only the pre-compression procedure termed CPLR. For the SE(B) specimen geometry, characterization was limited to Region I only, aligning with the primary objective of this work. Notably, for SE(B) specimens, only a single span length given by S = 8W and load ratio of R = 0.5 were utilized. In summary, selective constraints on test conditions and specimens were imposed to focus the experimental campaign on generating FCG data for Region I cracking most applicable to the research aims. Careful control and limitation of variables will facilitate analyzing the salient fatigue phenomena governing crack propagation in the joint material.

4.5. Fatigue Crack Growth Test

4.5.1. AISI 316L

Exploratory fatigue crack propagation tests on machined specimens were performed on the austenitic stainless steel material AISI 316L. For this material, the methodologies of the ASTM E647.standard [2] were used, as well as the two compression procedures: CPLR and CPCA.

Fatigue crack propagation and near-threshold testing were conducted using a 100 kN MTS servo-hydraulic test machine under laboratory ambient temperature and air conditions.

Figures 46, 47,48 and 49 illustrate the C(T) and SE(B) specimens, the latter for $S = 4W$ and $S = 8W$, respectively, mounted in the MTS test machine.

Crack length measurements during testing were performed using a compliance procedure, whereby the current crack length is assessed from the change in compliance of the specimen with increasing cycles. For these tests, load versus displacement records were obtained using clip gages, which defined the compliance of the C(T) specimen in terms of load-line displacement (LLD) or crack mouth opening displacement (CMOD) for the SE(B) sample. All tests were performed at a frequency of 15 Hz, load ratios of R = 0.1 and 0.5 and in the TL orientation (crack propagating longitudinally). For the SE(B) specimens, two different span lengths were utilized, given by $S = 4W$ and $S = 8W$.

Figure 46: C(T) specimens machined from AISI 316L stainless steel mounted in MTS test machine during fatigue crack propagation testing.
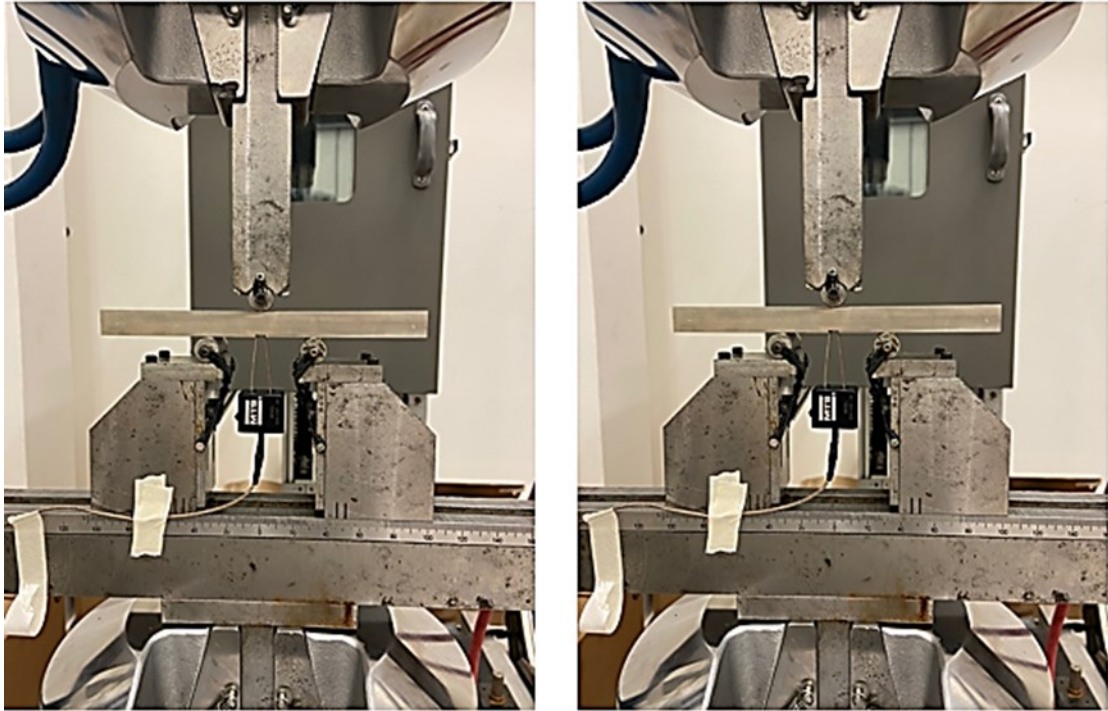
Figure 47: SE(B) specimens machined from AISI 316L stainless steel mounted in MTS test machine during fatigue crack propagation testing, with S/W = 4.

Figure 48: SE(B) specimen machined from AISI 316L stainless steel mounted in MTS test machine during fatigue crack propagation testing for S/W = 8.

Figure 49: SE(B) specimen of 316L stainless material in the MTS machine during the fatigue crack propagation test.

The final four-point bend configuration with a larger span is a non-standard specimen previously employed by Barbosa and Ruggieri [70] in fracture toughness testing of a C−Mn structural steel. As increasing the bend span of the specimen results in greater crack tip constraint for this bend configuration, see Barbosa and Ruggieri [63], the use of S/W = 8 mitigates effects of plastic deformation on fracture behavior that typically arise when testing smaller cracked specimens.

Prior to testing, fatigue pre-cracking of the test specimens is a critical step for determining near-threshold FCG behavior. For FCG testing using the conventional load reduction method, the fatigue precracking procedure closely followed the requirements provided in ASTM E647 [2] in conjunction with those also specified in ASTM E1820 [39] using a load ratio of R = 0.1. After precracking, the crack extension was 1 mm in the C(T) specimens and 0.75 - 1.00 mm for the SE(B) specimens.

In the case of FCG testing using the pre-compression method, the fatigue precracking procedure was performed by applying a compressive load, Pc, at a constant stress

ratio of R = 0.1 with P_{min} and P_{max} assuming negative (compressive) values and carefully selected such that the crack extension after 2×10^6 cycles were approximately 0.3 ~ 0.4 mm.

For the C(T) specimen, the maximum compressive load, P_{max}, was taken as 85% of the load defined by Eq. (A2.1) provided in ASTM E1820 [39]. In this case, the compressive loading was applied using small metallic blocks glued at the bottom and top edges of the specimen, in an arrangement similar to that described in Newman and Yamada [49], in order to ensure proper loading contact and transmission of the compressive loads to the specimen.

For the SE(B) specimens, the maximum compressive load, P_{max}, was first evaluated from the numerical analysis described in the Appendix B of this report and then the compressive load was applied using a four-point bend scheme similar to that employed by Barbosa and Ruggieri [63], [70], in which the inner span is half of the outer span, as can be seen in Figure 50.

Since the four-point bend specimen has a constant bending moment and thus zero shear stress at the crack plane, adopting a four-point pre-compression precracking procedure facilitates generating the required compressive load in the crack plane, which otherwise would not be possible using a three-point bend scheme. Figure 50 shows a schematic illustration of the pre-compression precracking procedure adopted to generate a compressive stress at the crack plane for the tested specimens.

For calculation of the loads and stress intensity factor, the equations from the ASTM E647 [2] and ASTM E1820 [39] standards were used as reference for the C(T) and SE(B) specimens, respectively.

Finally, it is important to note that the $\mathit{\Delta K}$ decreasing method ($\mathit{\Delta K}$ control) was used for determining the threshold, while the constant amplitude load method ($\mathit{\Delta P}$ constant) was used for the Paris region (Region II).

Figure 50: SE(B) specimen machined from AISI 316L stainless steel mounted in MTS test machine during four-point bend compressive precracking.

4.5.2. INCONEL 625 Girth Weld

Similar to the AISI 316L, fatigue crack propagation tests on machined specimens were conducted for the girth weld material of a typical API 5L Grade X65 pipe internally cladded with a nickel-chromium corrosion resistant alloy (CRA). For this weld joint, the ASTM E647 [2] standard methodologies and only the CPLR compression procedure were utilized.

The fatigue crack propagation and near-threshold testing were performed using a 100 kN MTS servo-hydraulic test machine under laboratory ambient temperature and air conditions.

Figure 51 illustrates the SE(B) specimens, for $S = 8W$, mounted in the MTS test machine.
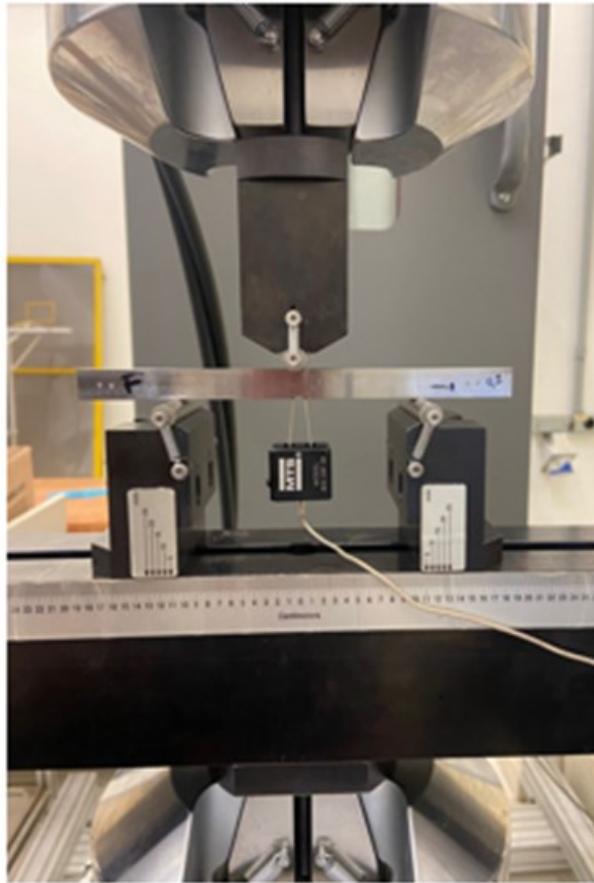
Figure 51: SE(B) specimens machined from weld joint material mounted in MTS test machine during fatigue crack propagation testing for S/W = 8.

Crack length measurements during testing were performed using a compliance procedure, in which the current crack length is assessed from the change in compliance of the specimen measured with increasing cycles. For these tests, load versus displacement records were obtained using clip gages, which defined the crack mouth opening displacement (CMOD) for the SE(B) sample. For fatigue threshold determination, all tests were conducted at a frequency of 15 Hz, load ratio of R = 0.5, with the crack propagating from the weld reinforcement to the weld root. For the SE(B) specimens, only a single span length given by S = $8W$ was utilized. The rationale for using a non-standard span has already been mentioned for the AISI 316L material.

For the SE(B) specimens, the maximum compressive load, Pmax, was utilized based on evaluation of the test results for the AISI 316L material. To perform the four-point bend pre-compression, the same scheme and procedure as the AISI 316L material was used. Thus, Figure 52 displays the SE(B) specimens mounted in the MTS test

machine, illustrating the pre-compression precracking procedure adopted to generate a compressive stress in the crack plane for the tested specimens.

For the tests in this project, after fatigue precracking of the specimens, the experimental measurements of near-threshold crack propagation rates and determination of ΔK_{th} values proceeded according to two of the three procedures described in section 3.2. Specifically, the standard load reduction procedure outlined in ASTM E647 [2] was followed, along with the CPLR method.

Figure 52: SE(B) specimen machined girth weld mounted in MTS test machine during four-point bend compressive precracking.

Finally, it is important to note that the ΔK decreasing method (ΔK control) was used for determining the threshold.

4.6. Scanning Electron Microscopy (SEM)

SEM is an instrument that can rapidly provide information on morphology and identification of chemical elements, being one of the most versatile tools available for observing and analyzing microstructural characteristics of solid objects in a sample. Its

use is common in biology, dentistry, pharmacy, engineering, chemistry, metallurgy, physics, medicine and geology.

The operating principle of a scanning electron microscope (SEM) is to use a small-diameter electron beam to scan the sample surface, point-by-point in successive lines and transmit the detector signal to a cathode ray display that is perfectly synchronized with the incident beam scanning. Meanwhile, energy dispersive X-ray spectroscopy (EDS) is an analysis performed that allows qualitative and semi-quantitative chemical evaluation of samples.

Thus, scanning electron microscopy was utilized with the objective of performing fracture type analysis (ductile, brittle, or mixed), as well as analyzing the sample surface, verifying crack initiation, propagation and failure regions.

SEM analysis was performed only for some samples of the AISI 316L material and weld joint, using a Jeol JSM-6010LA scanning electron microscope.

CHAPTER 5

5. RESULTS

5.1. Introduction

Preliminary Region I and II fatigue crack growth data acquired using C(T) and SE(B) specimens machined from AISI 316L steel are also shown.This chapter presents the results for the Inconel 625 girth weld obtained following the standard ASTM E647 [2] and CPLR procedures to determine the fatigue crack growth threshold ΔK_{th}. The experimental techniques used for threshold measurement and the parameters utilized in the MTS test machine are described.

5.2. AISI 316L Stainless Steel

Examining the homogeneous 316L steel was invaluable for assessing, validating and gaining insight into the pre-compression methodologies under investigation.

The experimental results encompass crack growth rate data acquired via all the threshold determination techniques described previously. To enhance clarity and visualization, the findings are delineated first for the C(T) specimens, followed by the SE(B) geometry. Segmenting the results facilitates comparison between the different specimen types and techniques within each test campaign.

5.2.1. C(T) Specimens

Figures 53-55 compare the near-threshold crack growth rate measurements versus ΔK for the C(T) specimen using different test procedures.
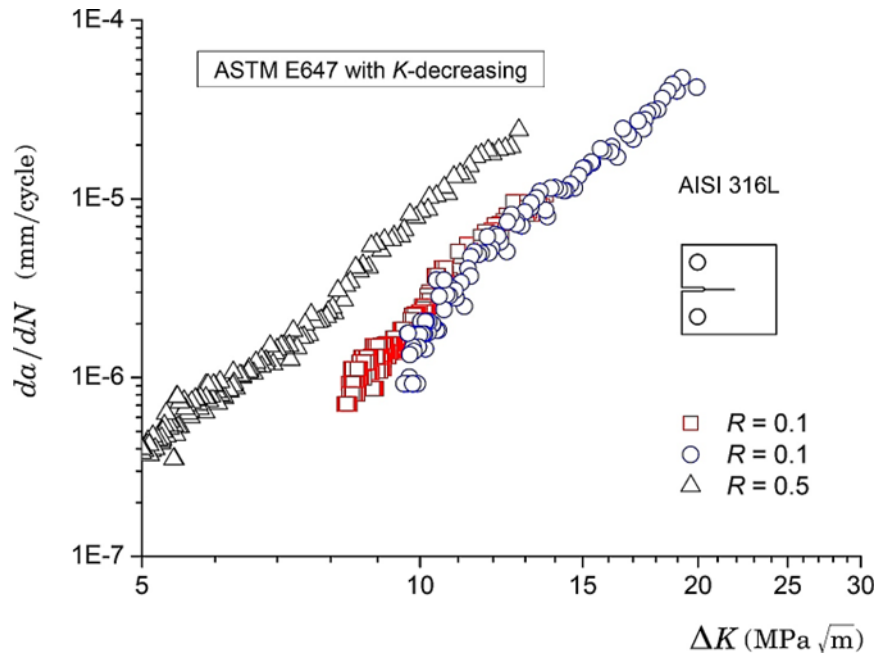
Figure 53: Near-threshold fatigue crack growth results for the C(T) specimen using the load reduction (decreasing K) procedure specified in ASTM E647 [2] at R = 0.1 and R = 0.5
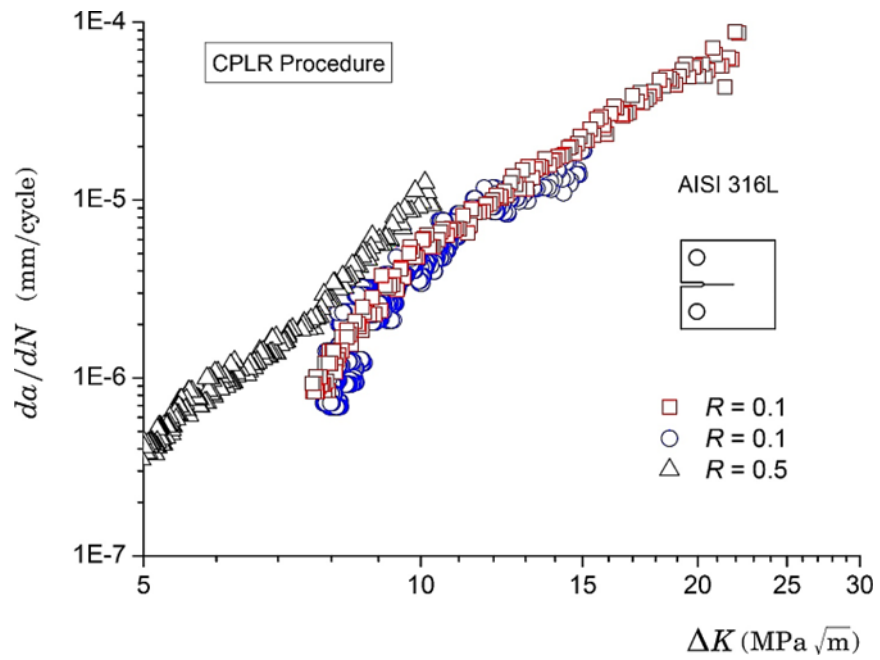
Figure 54: Near-threshold fatigue crack growth results for the C(T) specimen using the CPLR methodology at R = 0.1 and 0.5.
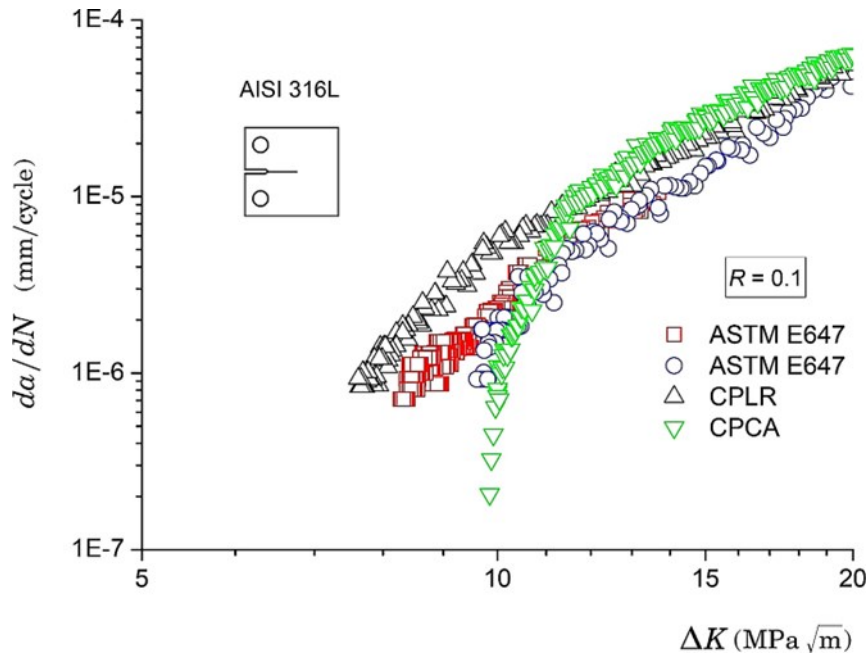
Figure 55: Comparison of near-threshold fatigue crack growth results for the C(T)

First examining Figure 53, which displays the near-threshold crack growth data measured using the load reduction procedure specified in ASTM E647 [2] for two different load ratios, R = 0.1 and 0.5. While the experimental data at R = 0.1 shows some scatter, the measured ΔK versus crack growth rate follows a common trend for both specimens tested and approaches a similar threshold value at a growth rate of 7 $\sim$ 8 $\times 10^{-7}$ mm/cycle. Further analyzing the same figure, a different behavior can be observed for the experimental results at R = 0.5, since increasing the load ratio generated a reduction in the near-threshold ΔK values. This outcome aligns with most previous published studies (see, for example, [73], [74], [75]).

Looking now at Figure 54, which shows the effect of pre-cracking in compression on the near-threshold crack growth data for the CPLR procedure, these experimental results exhibit similar characteristics as viewed in Figure 53, where utilizing a higher load ratio yields a reduction in the near-threshold ΔK value. Importantly, the fatigue crack growth rates for both test procedures (load reduction and CPLR) never reach rates below 7 $\sim$ 8 $\times 10^{-7}$ mm/cycle.

Figure 55 compares the near-threshold fatigue crack growth data for all test procedures conducted at a stress ratio of R = 0.1 (note the slightly different x-axis scale of the plot compared to previous Figures 53 and 54 to aid in evaluation and visualization of changes in threshold values). Significant features of these results include:

80

- The compressive pre-cracking load reduction technique (CPLR) provides (although only slightly) lower near-threshold $\varDelta K$ values compared to the corresponding values obtained in the ASTM E647 [2] load reduction procedure.
- The constant amplitude compressive pre-cracking procedure (CPCA) allows fatigue testing progression to much lower crack growth rates taking a increase on time.
- The CPCA procedure does not appear to significantly affect near-threshold crack propagation for the tested sample, since the resulting near-threshold rate versus $\varDelta K$ is similar to the corresponding rates for the load reduction method.

Surprisingly, this last feature contrasts markedly with the behavior displayed by the CPLR procedure, in which slightly lower near-threshold $\varDelta K$ values were obtained.

Figure 56 compares the near-threshold fatigue crack growth data for the load reduction and CPLR procedures conducted at a stress ratio of R = 0.5 (again note the slightly different x-axis scale compared to previous Figures 53 and 54 to facilitate evaluation and visualization of changes in threshold values). From these results and comparing with Figure 55, it can be stated that when utilizing a higher load ratio, the difference in the obtained near-threshold $\varDelta K$ values for the load reduction and CPLR methodologies approaches closer, becoming practically identical. This behavior may be associated with a reduced crack closure effect when using higher load ratios.
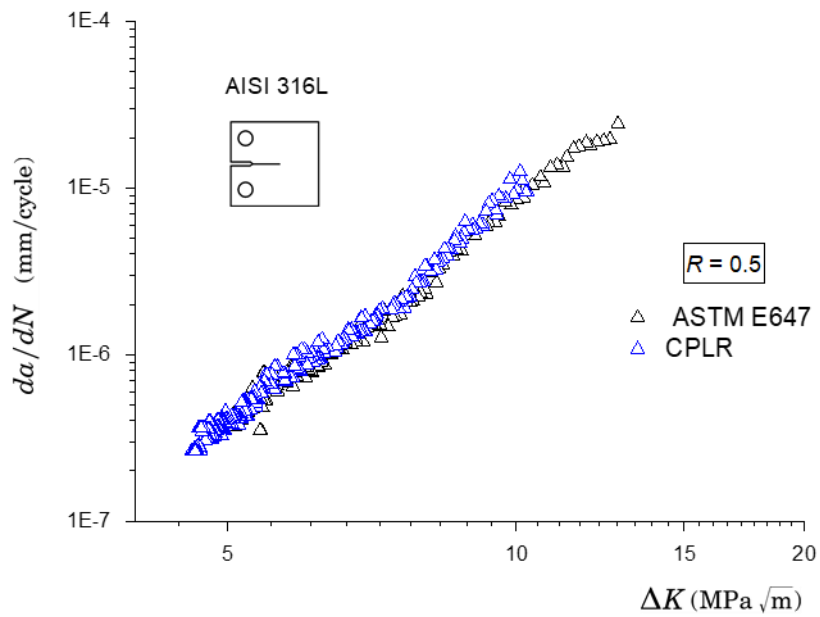
Figure 56: Comparison of near-threshold fatigue crack growth results for the C(T) specimen using the ASTM E647 and CPLR procedures at R = 0.5.
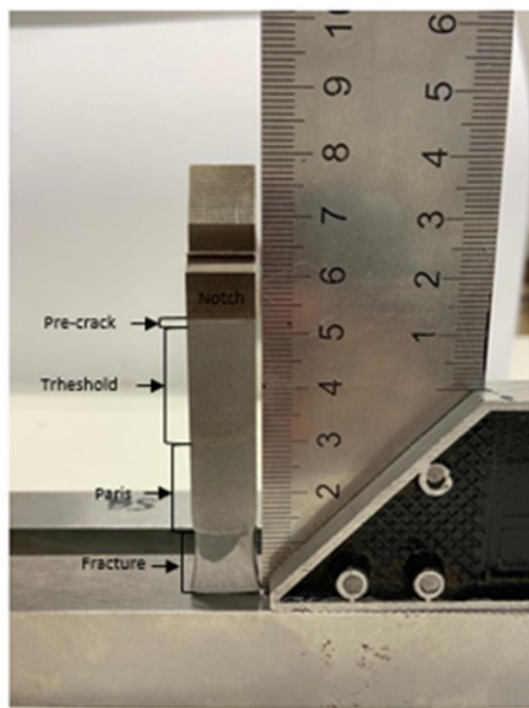
CP01 – *Threshold + Paris*

Figure 57: Region I and II for C(T) specimens.

In Figure 57 crack propagation is observed in a C(T) test specimen in which the 2 regions could be performed.

5.2.2. SE(B) Specimens

This section examines the evaluation of near-threshold crack growth rates versus $\mathit{\Delta K}$ for the SE(B) geometry using different test procedures in conjunction with varied specimen geometries, characterized by two different spans, S/W = 4 and 8. As noted previously, the increased span bend configuration of S/W = 8 is a non-standard specimen that can potentially improve the assessment of near-threshold $\mathit{\Delta K}$ values.

The use of this type of testing, 3-point bend with an increased span, can be useful in various engineering applications related to fatigue life assessments of structural components when there are severe limitations on material availability, as in the case of this project for typical circumferential pipeline and riser welds, including subsea risers and injection lines, with wall thicknesses in the range of 12 ~ 19 mm. In these cases, it is the relatively small pipe thickness that dictates the extraction of SE(B) specimens, which are preferably taken with a square cross-section in the pipe longitudinal direction [76] since increasing the specimen span raises the crack tip constraint (triaxiality), thereby mitigating effects of plastic deformation on fracture behavior that often arises when testing smaller cracked specimens.

Figures 58 (a, b) display the crack propagation data near the threshold for the ASTM E647 and CPLR procedures at the stress ratio, R = 0.1, for the SE(B) configurations and for S/W = 4 and S/W = 8.

Analyzing Figure 58(a) it is possible to say that, surprisingly, the fatigue crack growth behavior for the specimen geometry with S/W = 4 persists, in which the near threshold crack propagation rate measurements versus $\mathit{\Delta K}$ derived from the CPLR procedure are shifted to the right in the case of the CPLR method compared to the conventional load reduction procedure.
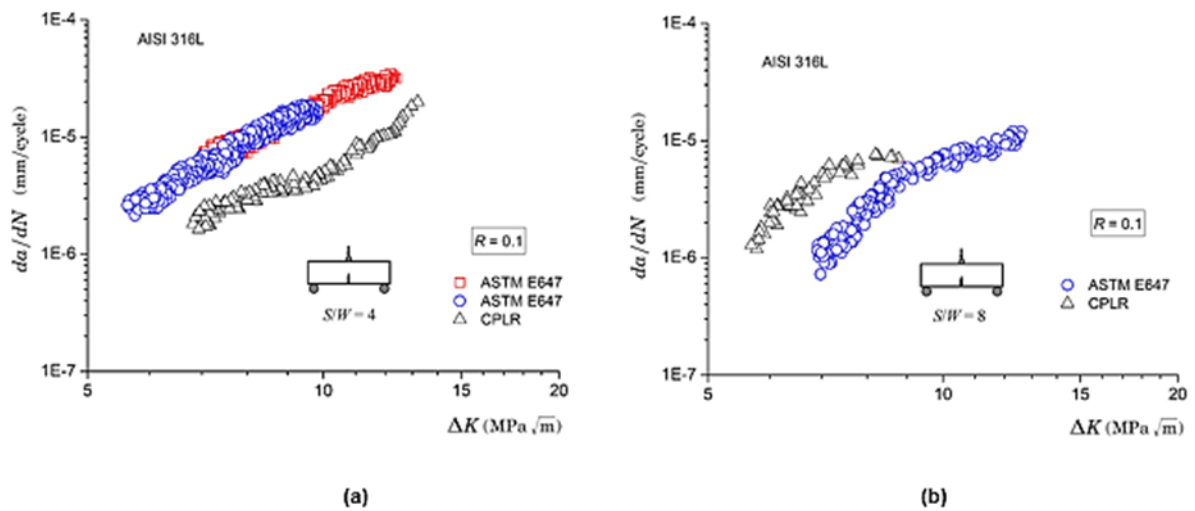
Figure 58: Comparison of fatigue crack propagation test results near the threshold for SE(B) specimens using ASTM E647 and CPLR procedures, for R=0.1: (a) S/W = 4 and (b) S/W = 8.

Now analyzing Figure 58(b), it is possible to observe that, for the SE(B) configuration with S/W = 8, a different picture now emerges, since the near threshold regime for this sample configuration for higher stress ratios is much better described. Therefore, the CPLR procedure provides lower ΔK values for fixed crack propagation rates, thus producing lower ΔK_{th} values.

The previously obtained fatigue threshold results can be reformulated into a more compelling presentation, in which the use of small specimens to measure near threshold fatigue data becomes more evident. Figures 59 and 60 provide selected da/dN vs. ΔK data for the C(T) specimen and for the SE(B) configuration with S/W = 8 derived from the conventional load reduction procedure (ASTM E647) and CPLR method. For the fatigue crack propagation data comparison between the compact and bending specimen to be made, the C(T) specimen will serve as reference.
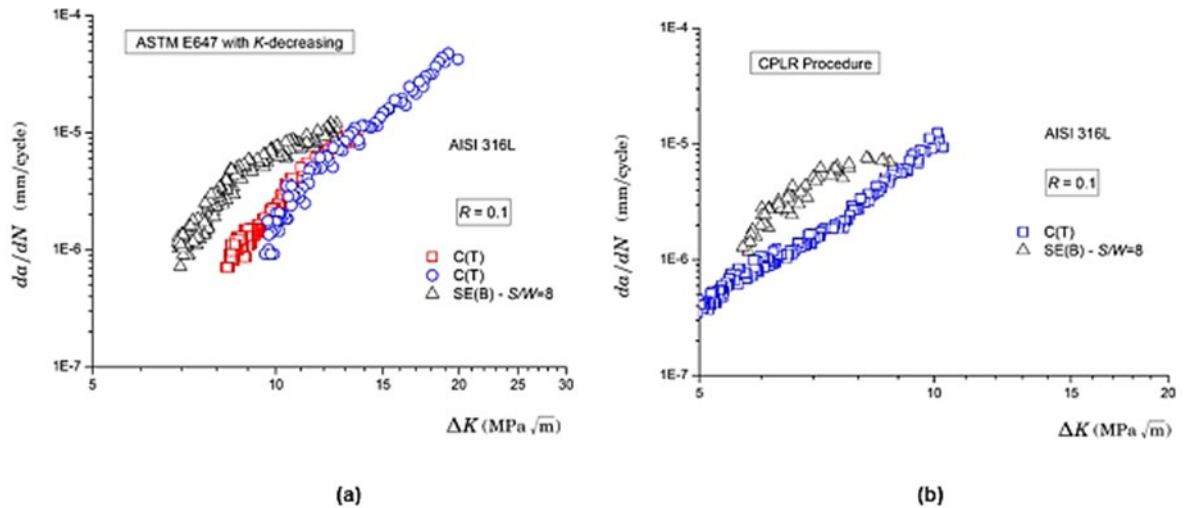
Figure 59: Comparison of fatigue crack propagation test results near the threshold using ASTM E647 and CPLR procedures, for R=0.1 and for C(T) specimens and for the SE(B) geometry with $S/W = 8$.
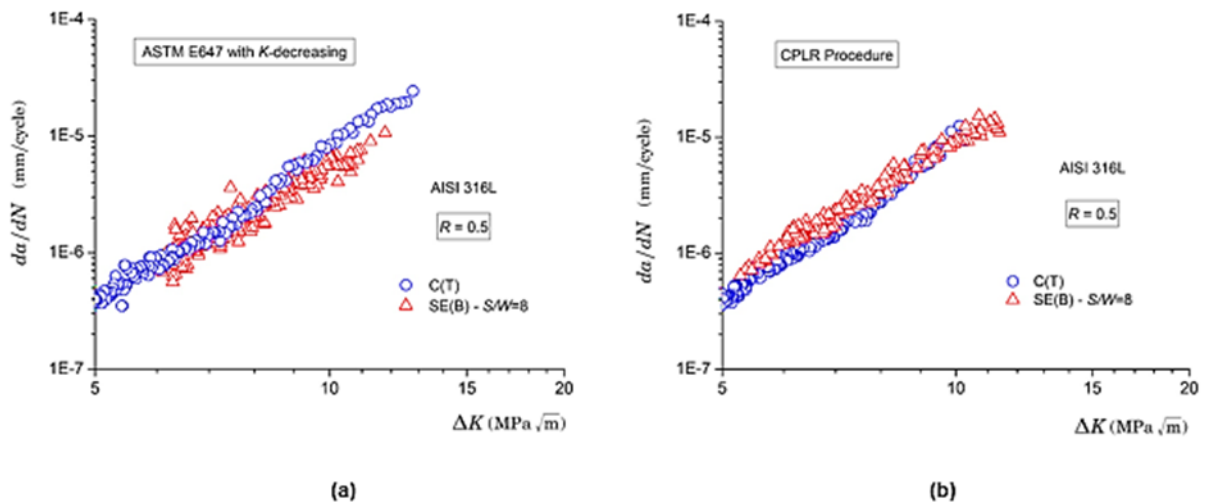
Figure 60: Comparison of fatigue crack propagation test results near the threshold using ASTM E647 and CPLR procedures, for R=0.5 and for C(T) specimens and for the SE(B) geometry with $S/W = 8$.

Let's focus first on the near threshold crack propagation data for the stress ratio, R = 0.1 shown in Figure 59 (a, b). Analyzing this figure, it can be said that the CPLR procedure shifts the da/dN vs. ΔK curves to the right, thus reducing the estimated ΔK_{th} values. Notably, observe that the near threshold crack propagation data for the SE(B) geometry is consistently slightly higher than the corresponding data for the C(T) specimens, that is, for a fixed value of ΔK, the corresponding crack propagation rates are higher. In addition, it is possible to observe, however, that the minimum crack

propagation rates for the SE(B) configuration are greater than 10^{-6} mm/cycle, which makes it essentially impossible to determine a reliable ΔK_{th} value, according to the ASTM E647 [2] or ISO 12108 [57] standard criteria.

Now, let's focus on the da/dN vs. ΔK data for the stress ratio, R = 0.5 shown in Figure 60 (a and b). Analyzing this figure, it can be said there are strong similarities in both test procedures between the near threshold crack propagation data for the C(T) specimen and the SE(B) configuration with $S/W = 8$. The overall trend of slightly shifting near threshold crack propagation rates versus ΔK to the left when the CPLR method is employed still remains, but the effect of pre-cracking in compression on the FCG results is relatively weak. However, the fatigue crack propagation response shown in these plots provides a particularly interesting outcome, as the use of small SE(B) specimens with higher span characterizes well the near threshold ΔK values instead of using larger C(T) geometries.

The assessment of the near threshold value of the stress intensity factor, ΔK_{th}, is also interesting. Standard procedures, including specifically the one in ASTM E647 [2], characterize an operational definition for ΔK_{th} by first determining the best linear fit of $log(da/dN)$ vs. $log(\Delta K)$ data over experimental crack propagation rate values in the range between 10^{-7} mm/cycle and 10^{-6} mm/cycle and then, based on the best linear fit relationship and associated fitting parameters, it is possible to determine ΔK_{th} as the ΔK value corresponding to a crack propagation rate of $da/dN = 10^{-7}$ mm/cycle.

Although the methodology facilitates the evaluation of a representative ΔK_{th} value in a relatively simple manner, it can be potentially affected by the quality of the near threshold crack propagation data, particularly if the obtained results have a high amount of data scatter, or a deviation from the linear relationship between $log(da/dN)$ and $log(\Delta K)$ and other potentially anomalous behaviors. In fact, this is exactly the case for the results obtained for the SE(B) specimen with $S/W = 4$ tested at stress ratios R = 0.1 and 0.5 and for the SE(B) geometry with $S/W = 8$ tested at R = 0.1, as can be seen in Figures 57 and 58, respectively. Thus, clearly, an alternative and yet simple procedure to assess the significant ΔK_{th} value more adequately is necessary, especially in the case of smaller specimens, for which the quality of the near threshold crack propagation data in the range of 10^{-7} mm/cycle and 10^{-6} mm/cycle is not guaranteed.

To resolve this issue, Figures 61 and 62 display the best linear fit of log(da/dN) vs. $log(\Delta K)$ data for the representative C(T) specimen tested at R = 0.5 using the conventional load reduction procedure (ASTM E647) and the CPLR method in different ranges of experimental crack propagation rate values: (a) 10^{-7} mm/cycle and 10^{-6} mm/cycle and (b) 10^{-6} mm/cycle and 10^{-5} mm/cycle.

It is worth noting that according to the ASTM standard, the near threshold ranges of the stress intensity factor are evaluated by determining the best linear fit of the $log(da/dN)$ vs. $log(\Delta K)$ data, as per equation 6. The fitting range includes data between 10^{-7} mm/cycle and 10^{-6} mm/cycle for the ASTM standard.

$$\log_{10} \Delta K = P_1 . \log_{10} da/dN + P_0, \quad (6)$$

Where P_0 and P_1 are fitting parameters.

(a)   (b)
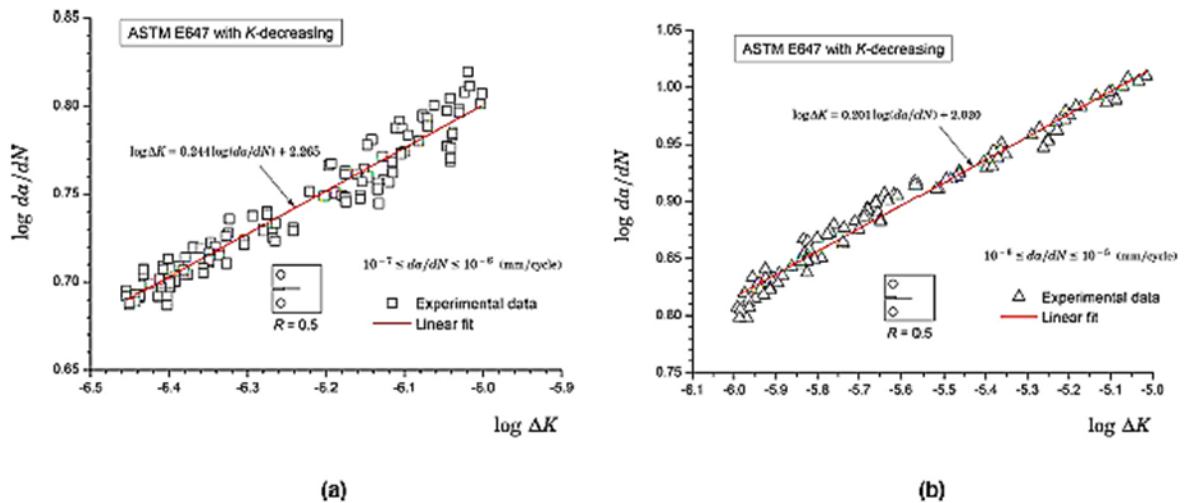
Figure 61: Best linear fitting relationship of $log(da/dN)$ vs. $log(\Delta K)$ data for representative C(T) specimen tested using the conventional decreasing K method (ASTM E647): (a) Experimental data in the range of 10^{-7} mm/cycle and 10^{-6} mm/cycle. (b) Experimental data in the range of 10^{-6} mm/cycle and 10^{-7} mm/cycle.
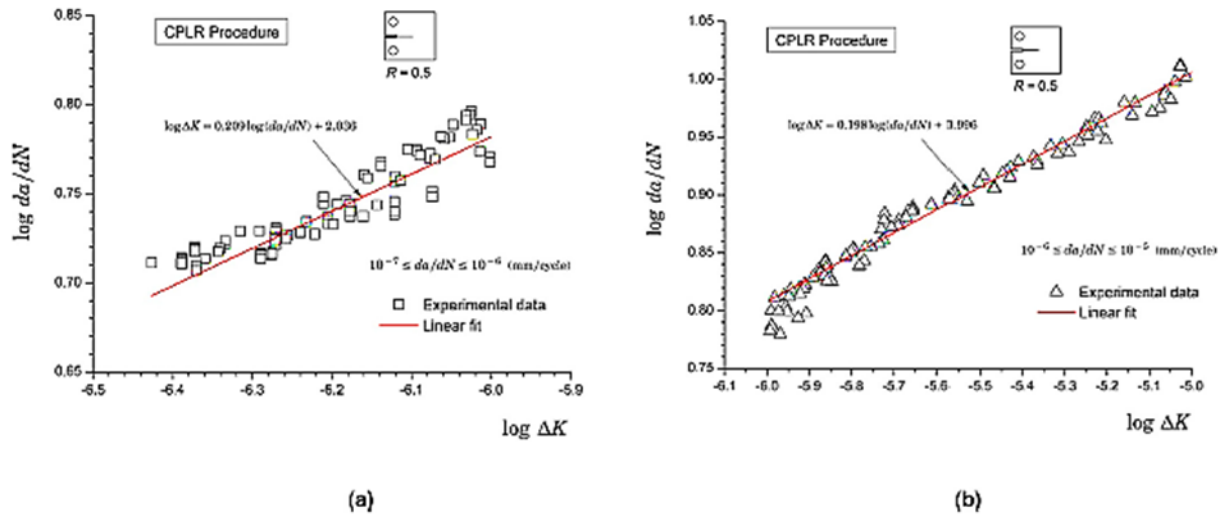
Figure 62: Linear relationship of best fit for the $log\ da/dN$ vs. $log\varDelta K$ data for representative test specimen C(T) using the CPLR methodology: (a) Experimental data in the range of 10^{-7} mm⁄cycle and 10^{-6} mm⁄cycle. (b) Experimental data in the range of 10^{-6} mm

The fitting lines and corresponding first-degree equations are provided on the graphs to assist in evaluating the linear relationship of fatigue crack propagation data. Note that the axis scales are slightly different in Figures 61(b) and 62(b) to accommodate differences in the data range.

As the C(T) geometry yielded the most satisfactory values for da/dN vs. $\varDelta K$, better describing fatigue behavior near the threshold in this study, these analyses may provide the basis for a more effective assessment procedure for $\varDelta K_{th}$, which is reasonably less sensitive to the quality of crack propagation data near the threshold in the range of very low crack propagation rate values.

Figures 61 and 62 clearly show that the adopted data range, over which the best-fit straight line is determined, has a decreasing effect on the slope of the linear relationship between the $log(da/dN)$ vs. $log(\varDelta K)$ data and consequently, on the estimated value of $\varDelta K_{th}$ corresponding to a crack propagation rate of $da/dN = 10^{-7}$ mm/cycle, regardless of the testing procedure. Table 8 displays the $\varDelta K_{th}$ values derived from both data ranges and provides the degree of agreement (quality of fit) between the linear fit model and the experimental data, characterized by the coefficient of determination, R^2.

It is worth noting that although the use of experimental data in the range of 10^{-6} mm/cycle and 10^{-7} mm/cycle yields a more conservative $\varDelta K_{th}$ value compared to the other data range used, the differences are relatively small, as shown in Table 8. Additionally, it can be observed that the estimated $\varDelta K_{th}$ value is essentially insensitive to the adopted testing procedure (decreasing K method or CPLR methodology).

Table 8: ΔK_{th} values derived from the best-fit straight line of $log(da/dN)$ vs $log(\varDelta K)$ data over different ranges of experimental crack growth rate values for the C(T) specimens and SE(B) geometries with S/W = 4 and 8 tested at R = 0.5.

Specimen Geometry	Range of da/dN	Methodology	$\Delta K_{th,\text{ASTM}}$ (MPa.m$^{1/2}$)	R^2
C(T)	$10^{-6} \leq da/dN \leq 10^{-5}$	ASTM E647	4.1	0.98
		CPLR	4.1	0.97
	$10^{-7} \leq da/dN \leq 10^{-6}$	ASTM E647	3.6	0.93
		CPLR	3.7	0.93
SE(B) – S/W = 4	$10^{-6} \leq da/dN \leq 10^{-5}$	ASTM E647	3.2	0.91
		CPLR	3.0	0.96
SE(B) – S/W = 8	$10^{-6} \leq da/dN \leq 10^{-5}$	ASTM E647	3.2	0.94
		CPLR	3.0	0.97

The results in Table 8 provide the motivation for determining the threshold stress intensity factor value for the SE(B) specimens analyzed here. Using the best-fit straight line of the $log(da/dN)$ vs $log(\varDelta K)$ data for the crack growth rate values in the range of 10^{-6} mm/cycle and 10^{-5} mm/cycle, a representative ΔK_{th} value corresponding to a crack growth rate of $da/dN = 10^{-7}$ mm/cycle is then obtained.

Table 8 also includes the $\varDelta K_{th}$ values for the selected SE(B) geometry with S/W = 4 and 8 for both test procedures. These results, when combined with the previous near-threshold fatigue behavior, indicate that the ΔK_{th} values exhibit almost no sensitivity to the adopted test procedure and implementation of the compressive pre-cracking

technique, even in the case of the relatively small bend configurations employed in the present experimental investigation.

Figures 63, 64 and 65 display, respectively, the fracture surface appearance for the C(T) and SE(B) specimens, the latter for S/W = 4 and S/W = 8, after the fatigue crack growth testing for the ASTM E647 and CPLR procedures at R = 0.1 and R = 0.5.

As can be observed in Figure 63 (b, d), the compressive pre-cracking technique in 4-point bending was effective, since the load value was adjusted to generate the precrack that naturally arrests at $2x10^6$ cycles. After fatigue precracking of all specimens, the crack growth region for threshold determination can be seen. Here, it is important to mention that the fatigue crack growth occurred through equiaxed austenite grains. The final region is the fracture, in which all specimens were broken in liquid nitrogen.

(a)   (b)   (c)   (d)
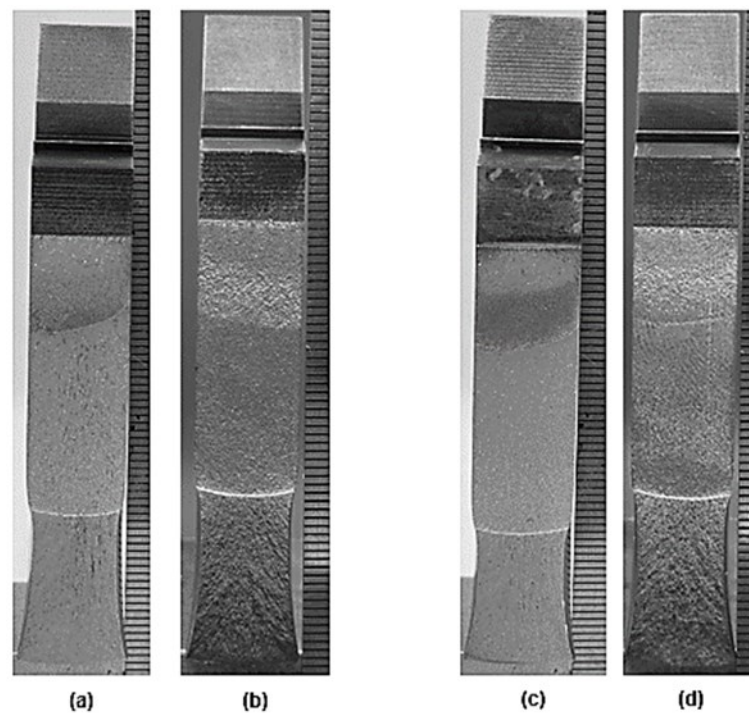
Figure 63: Fracture surface appearance for the AISI 316L material: C(T) specimens: (a) ASTM E647 – R=0.1, (b) ASTM E647 – R=0.5, (c) CPLR – R=0.1 and (d) CPLR – R=0.5.
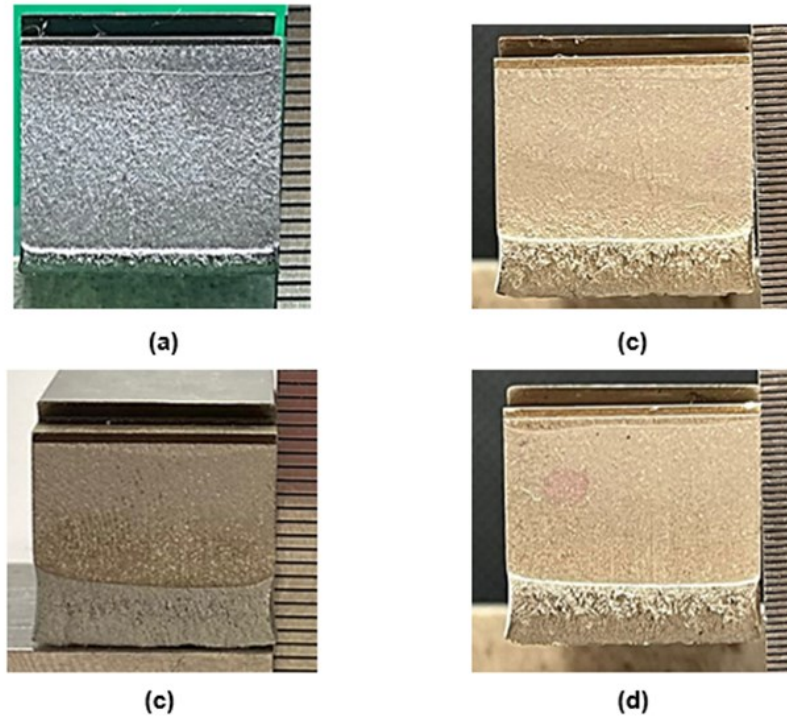
Figure 64: Fracture surface appearance for the AISI 316L material: SE(B) specimens with *S/W* = 4: (a) ASTM E647 – R=0.1 (Sp03), (b) ASTM E647 – R=0.5 (Sp27), (c) CPLR – R=0.1 (Sp11) and (d) CPLR – R=0.5 (Sp26).
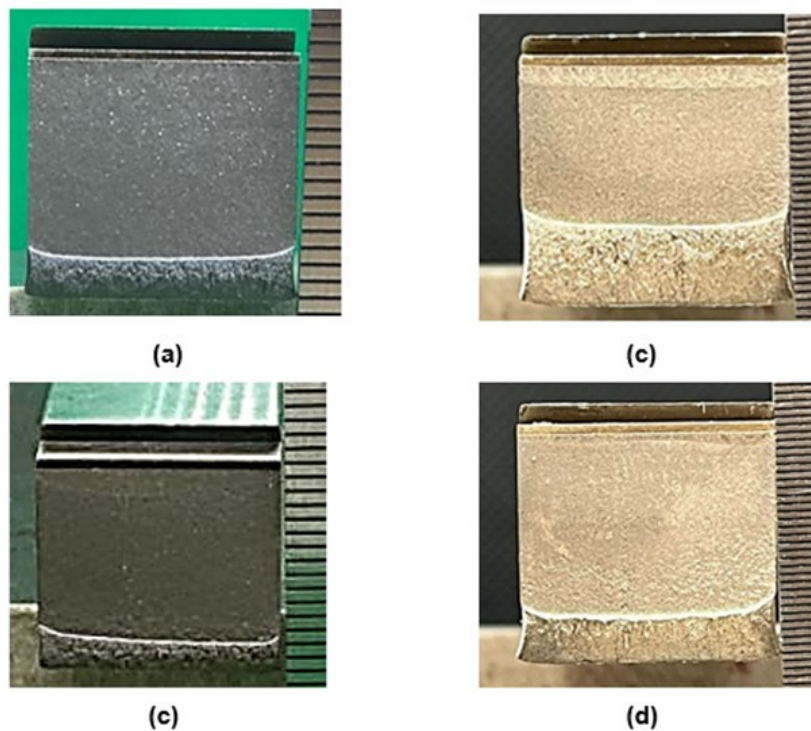
Figure 65: Fracture surface appearance for the AISI 316L material: SE(B) specimens with *S/W* = 8: (a) ASTM E647 – R=0.1 (Sp18), (b) ASTM E647 – R=0.5 (Sp23), (c) CPLR – R=0.1 (Sp15) and (d) CPLR – R=0.5 (Sp25).

To evaluate the fracture surface of the samples shown in Figures 64 and 65. Figure 66 presents a schematic of how the scanning electron microscopy (SEM) analyses were performed for each fracture region.
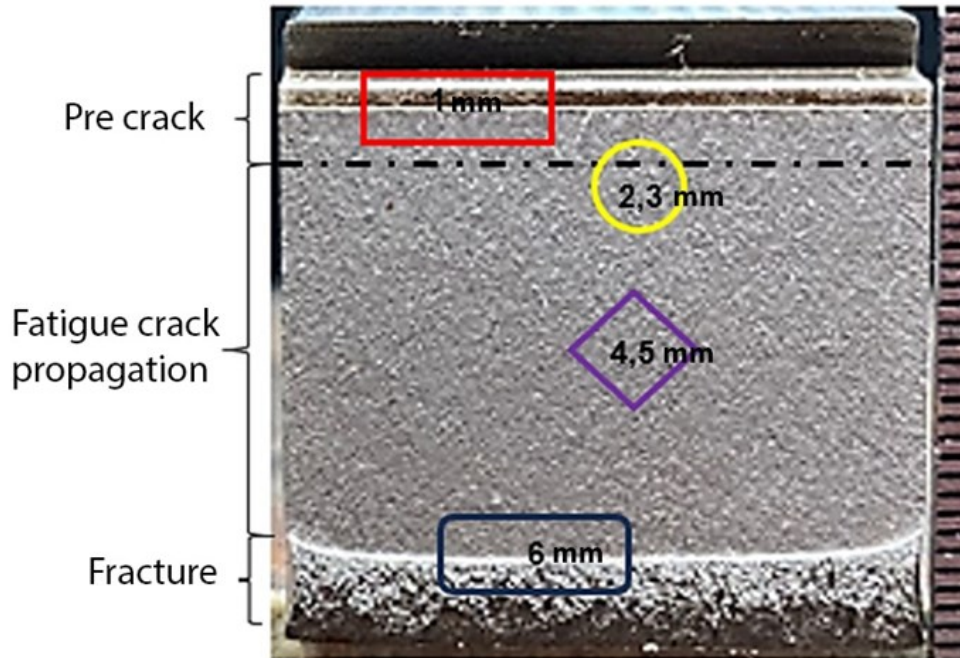
Figure 66: Schematic illustration of the fracture surface of a specimen, depicting the regions where SEM analyses were performed.

Figure 66, the following legend applies:

- Region 1: Image showing the notch and measured precrack size - Depiction (a), 15x magnification.
- Regions 2,3: Images displaying the crack propagation front, several millimeters beyond the precrack - Representation (b), 50x magnification and (c), 200x magnification.
- Regions 4,5: Images showing the crack propagation front, near the specimen mid-section - Depiction (d), 200x magnification and (e), 500x magnification.
- Region 6: Image exhibiting the threshold test end (test arrest) and start of brittle fracture (liquid nitrogen break) - Representation (f), 50x magnification.

Figures 67 to 74 display, in that order, the SEM images for the AISI 316L SE(B) specimens, under the following conditions:

- Sp03 – ASTM E647 procedure – S/W = 4 and R = 0.1;
- Sp27 – ASTM E647 procedure – S/W = 4 and R = 0.5;
- Sp18 – ASTM E647 procedure – S/W = 8 and R = 0.1;
- Sp23 – ASTM E647 procedure – S/W = 8 and R = 0.5;
- Sp11 – CPLR procedure – S/W = 4 and R = 0.1;
- Sp26 – CPLR procedure – S/W = 4 and R = 0.5;
- Sp15 – CPLR procedure – S/W = 8 and R = 0.1;
- Sp25 – CPLR procedure – S/W = 8 and R = 0.5.
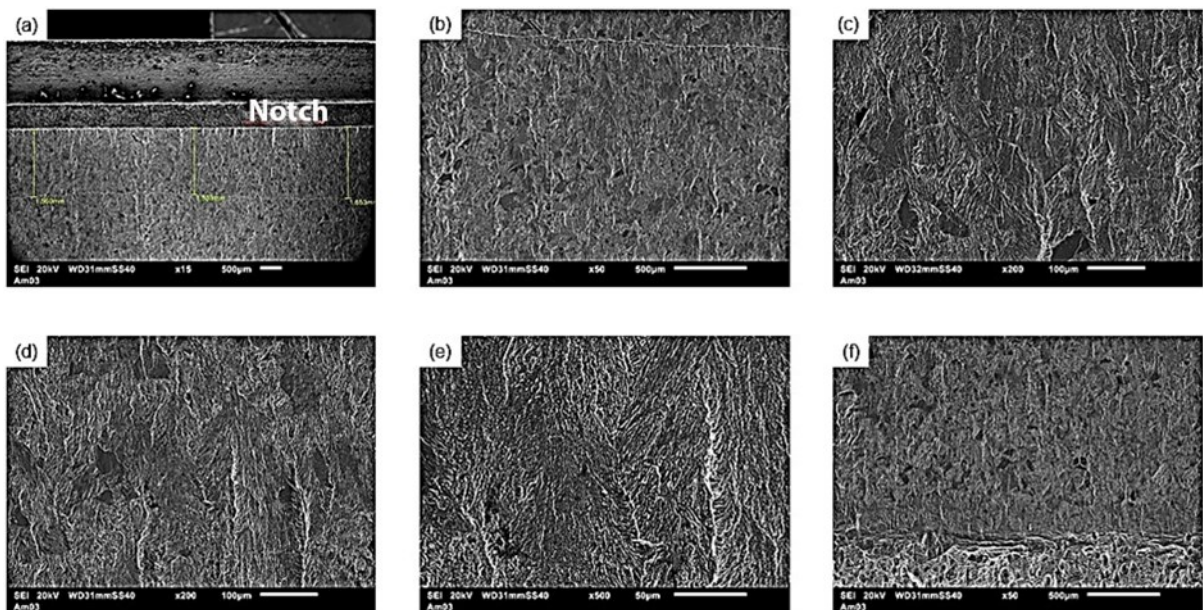
Figure 67: SEM images, at various magnifications, of the fracture surface of sample Sp03: ASTM E647 – S/W = 4 and R = 0.1.
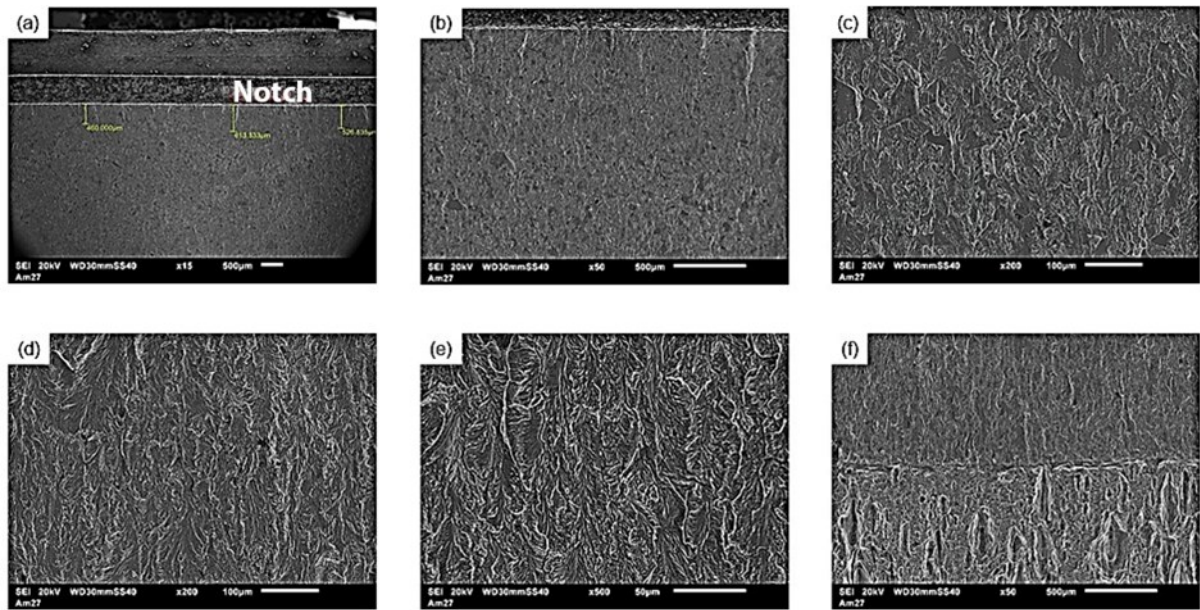
Figure 68: SEM images, at various magnifications, of the fracture surface of sample Sp27: ASTM E647 − S/W = 4 and R = 0.5.
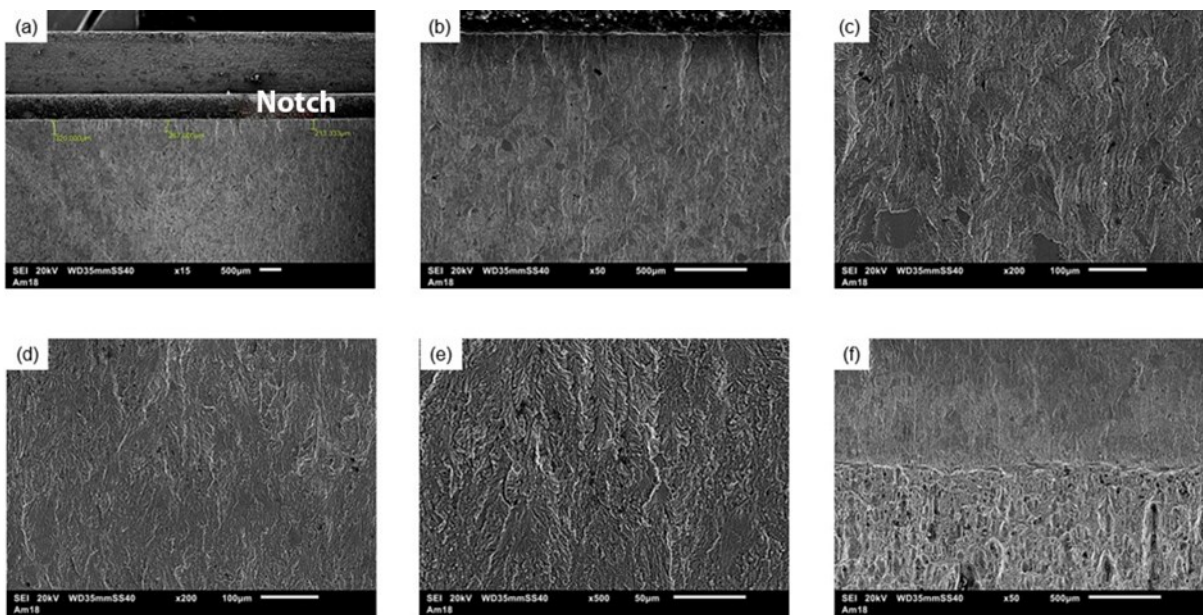
Figure 69: SEM images, at various magnifications, of the fracture surface of sample Sp18: ASTM E647 − S/W = 8 and R = 0.1.
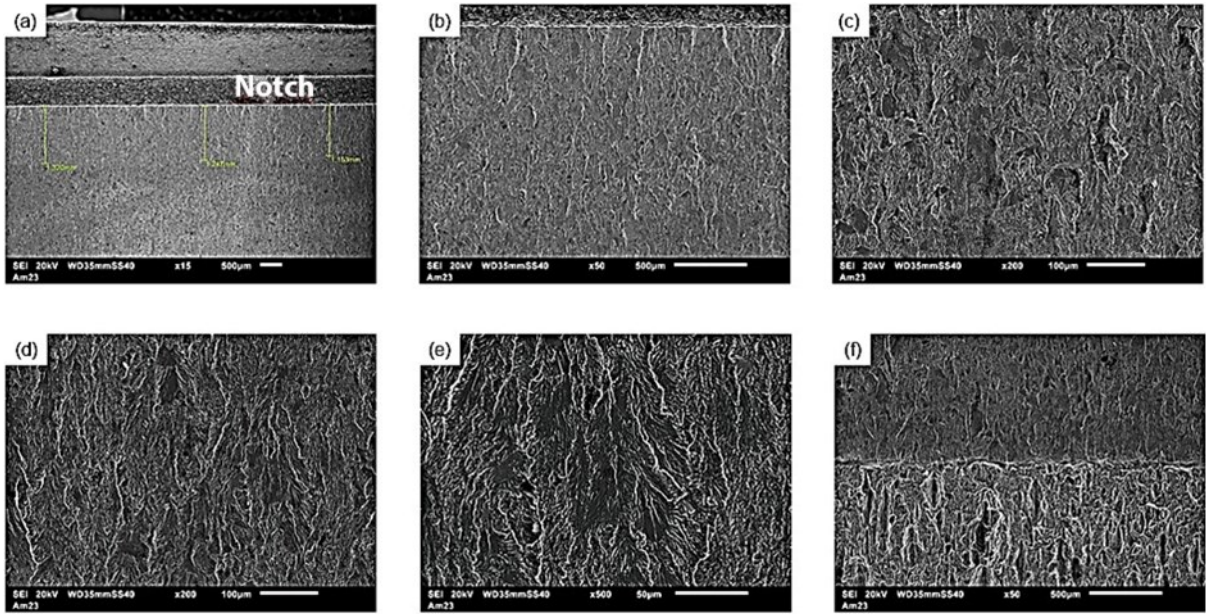
Figure 70: SEM images, at various magnifications, of the fracture surface of sample Sp23: ASTM E647 – S/W = 8 and R = 0.5.
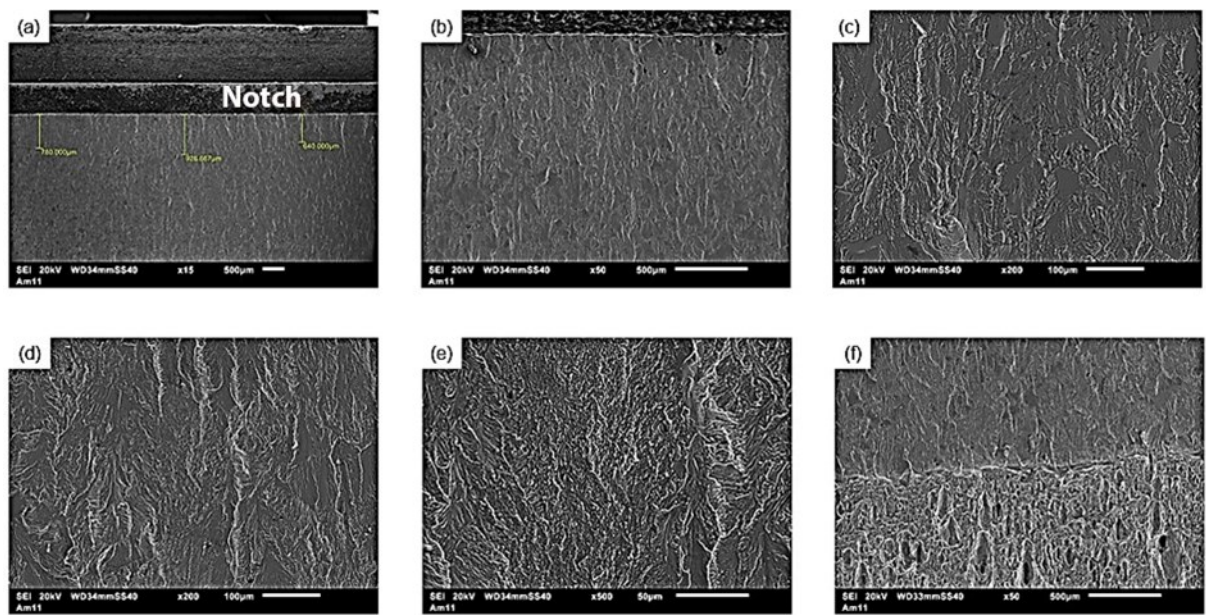
Figure 71: SEM images, at various magnifications, of the fracture surface of sample Sp11: CPLR – S/W = 4 and R = 0.1.
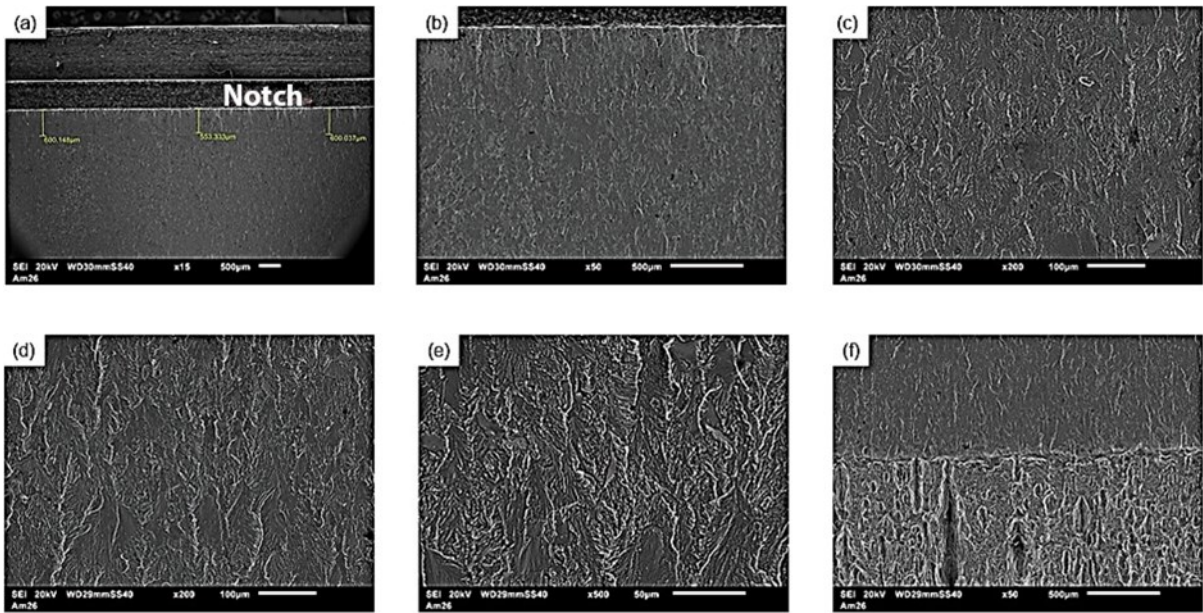
Figure 72: SEM images, at various magnifications, of the fracture surface of sample Sp26: CPLR – S/W = 4 and R = 0.5.
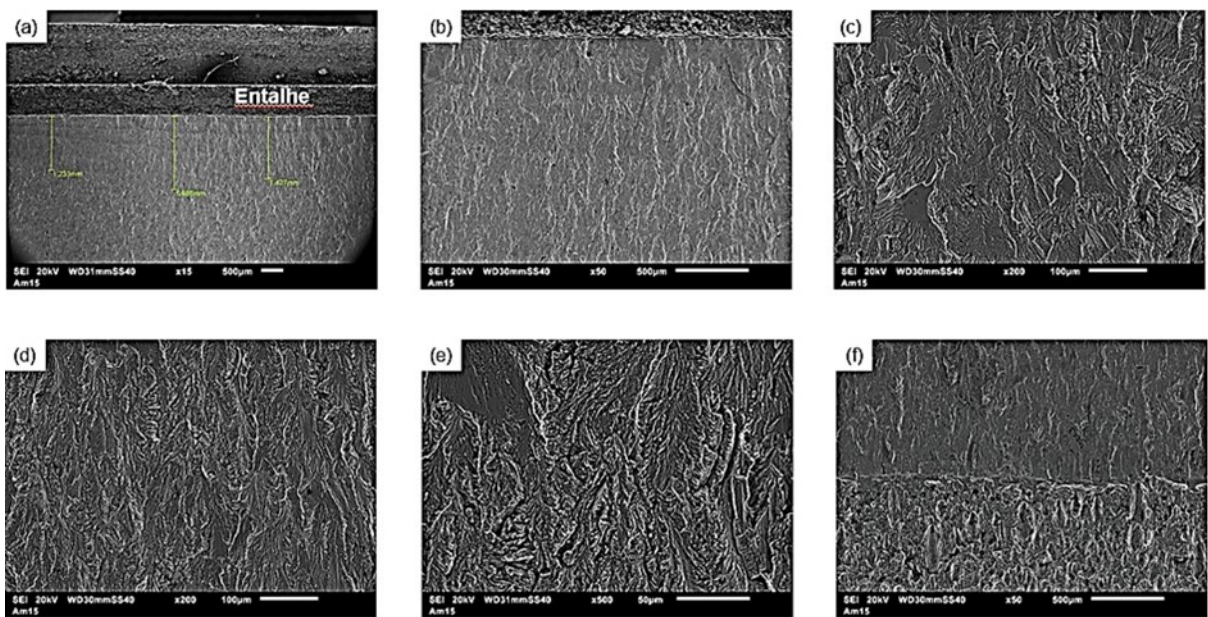
Figure 73: SEM images, at various magnifications, of the fracture surface of sample Sp15: CPLR – S/W = 8 and R = 0.1.
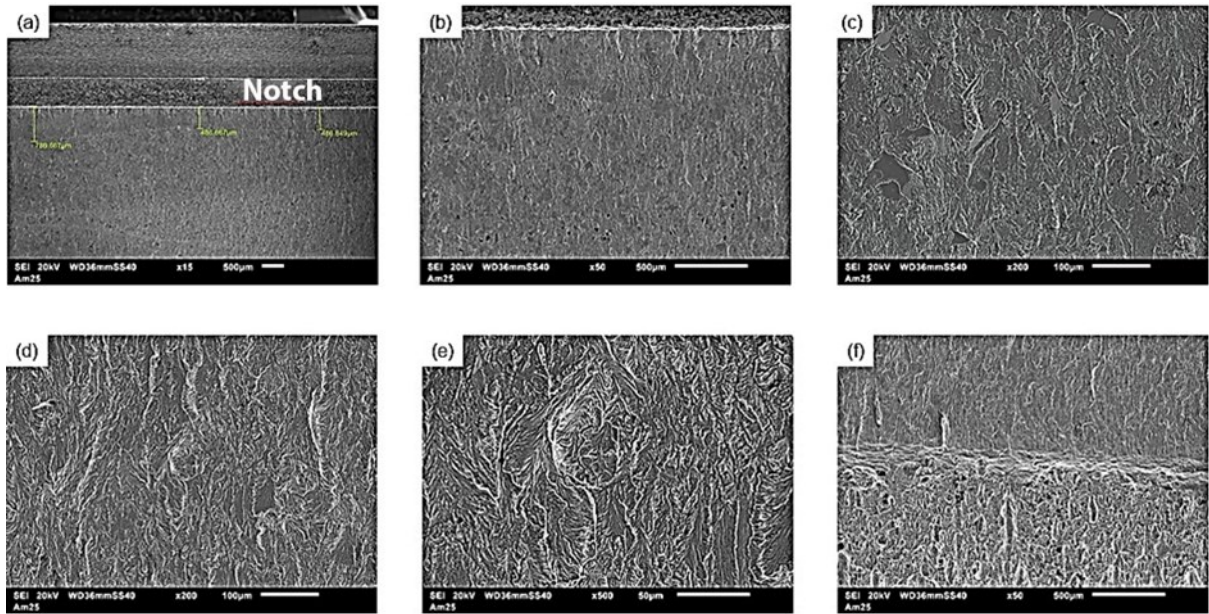
Figure 74: SEM images, at various magnifications, of the fracture surface of sample Sp25: CPLR – S/W = 8 and R = 0.5.

Based on the SEM analyses (Figures 67 to 74), it can be confirmed, as previously mentioned, that the technique of inducing the pre-crack in compression bending in 4 points was successfully executed, as the crack initiated and propagated. Additionally, after fatigue pre-cracking (3 or 4-point bending) of all specimens, it is possible to observe the crack propagation region for determining the threshold. This region, starting after pre-cracking and ending before brittle fracture, exhibits a ductile fracture appearance with stable crack growth. It is worth noting again that the crack growth occurred through equiaxial austenite grains. Finally, the last region shows a brittle fracture appearance, considering that all specimens were broken in liquid nitrogen.

5.3. INCONEL 625 Girth Weld

Figure 75 presents the results of the fatigue crack propagation tests for threshold determination on the SE(B) geometry (Notch located in the weld reinforcement) (R=0.5, S/W=8) per ASTM E647. Three repeat specimens were tested under this condition.

Figure 75: Results of the fatigue crack propagation tests from region I of the *da/dN vs ΔK* curve for the SE(B) geometry, *S/W* = 8, R = 0.5 and ASTM E647 methodology.

As can be seen in Figure 76, the test results show that in Region I the fatigue crack growth rate data for the girth weld has higher *ΔK* values when using the CPLR methodology, which may be due to crack closure effects. Three repeat specimens were tested using SE(B) geometry (R=0.5, *S/W*=8).
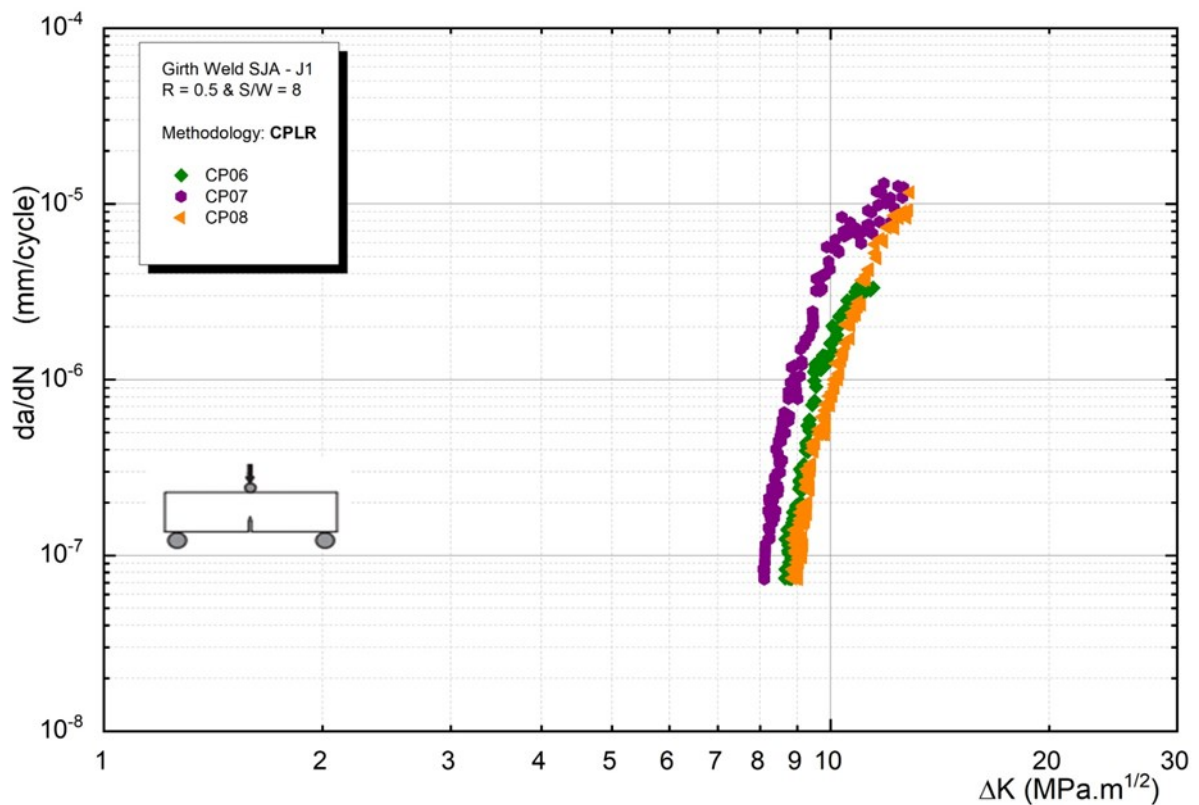
Figure 76: Region I fatigue crack growth results for the SE(B) specimen (*S/W*=8, R=0.5) tested via the CPLR methodology.

Figure 77 presents a comparison between the ASTM E647 and CPLR methodologies under the same conditions of R=0.5 and *S/W*=8. Analyzing the threshold determination fatigue crack growth results in Figure 77, unlike observations for the austenitic stainless steel AISI 316L, the CPLR pre-compression technique demonstrated no improvements over the standard ASTM E647 methodology for this case.

The compression technique only marginally reduced residual stresses at the notch front. A more likely contributor to the observed fatigue crack growth behavior is the heterogeneous material through which propagation occurs. Specifically, the ferritic-pearlitic API 5L Grade X65 base metal exhibits markedly different microstructural features and mechanical properties compared to the predominantly austenitic, nickel-chromium based corrosion resistant alloy (CRA) weld. The hardness mismatch between base and weld metals further accentuates this discontinuity. As fatigue cracks traverse these dissimilar zones, variation in local yield strength, work hardening behavior and slip character induces non-uniform crack tip stresses and deformation.

This drives crack path deviation and deflection at the fusion boundary, altering the effective driving force ΔK required for sustained propagation. The complex fatigue crack-microstructure interactions across base and weld materials potentially explain the test results.
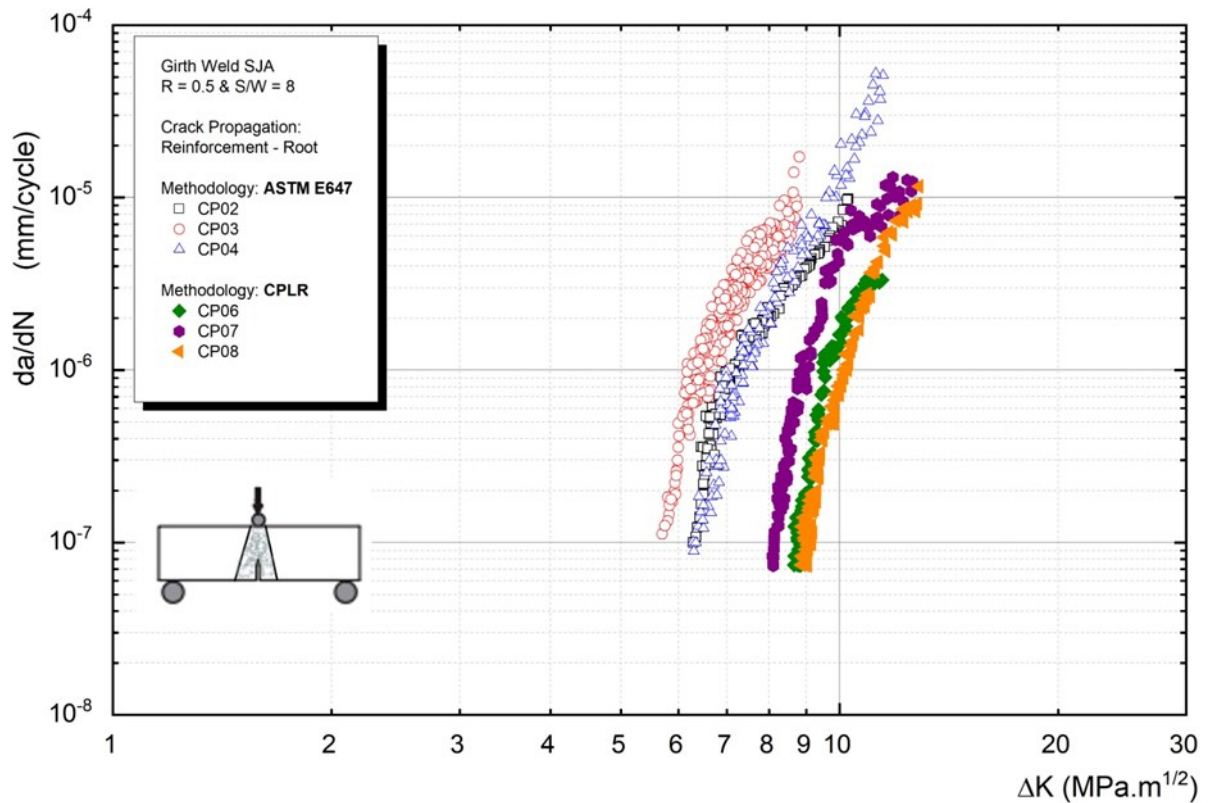
Figure 77: Comparison of the fatigue crack propagation test results from Region I of the *da/dN vs ΔK* curve for the SE(B) geometry (Notch located at the weld reinforcement), *S/W*=8, R=0.5 for the ASTM E647 and CPLR methodologies.

Tests were also conducted for both methodologies (ASTM E647 and CPLR) with SE(B) geometry, positioning the notch at the weld root. The results, as observed in Figure 78, show a similar behavior and ΔK value to those obtained with the notch located at the weld reinforcement. During these tests, it was noted that initiating fatigue threshold measurements required starting with a value close to the limit. This is because, due to the geometry and crack growth orientation, the crack propagates more rapidly, consuming the entire ligament and not reaching the rates established by ASTM E647 standard.
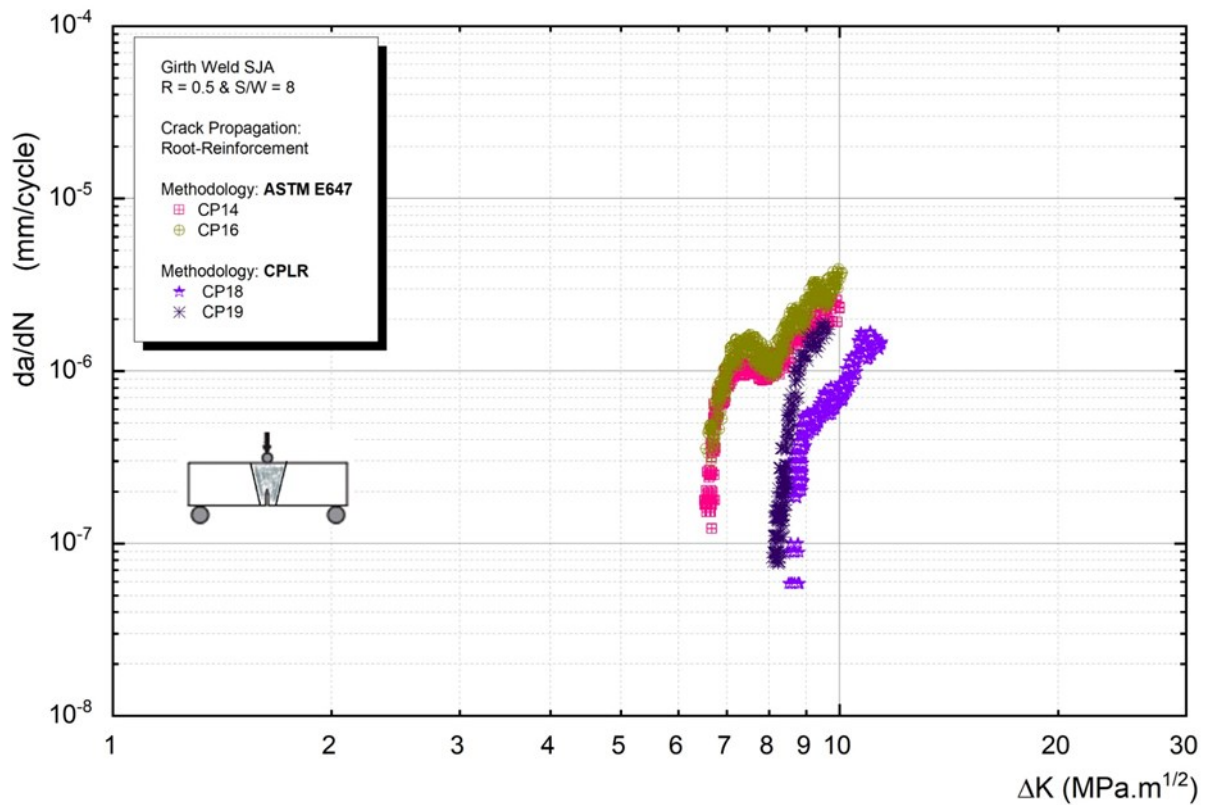
Figure 78: Comparison of the fatigue crack propagation test results from Region I of the *da/dN vs ΔK* curve for the SE(B) geometry (Notch located at the weld root), *S/W*=8, R=0.5 for the ASTM E647 and CPLR methodologies.

Table 8 presents the ΔK_{th} values corresponding to various analyzed conditions for the weld joint material. It's important to note that the technical, or operational, definition of this parameter aligns with finite crack propagation rates equal to *da/dN*, ASTM = 10^{-7} mm/cycle, as specified in the ASTM E647 [2] standard. In accordance with the ASTM standard, the threshold stress intensity factor ranges are determined by establishing the best linear fit of the *log(da/dN) vs. log(ΔK)* data, as outlined in Equation (5). The fitting range encompasses data falling between 10^{-7} mm/cycle and 10^{-6} mm/cycle for the ASTM standard.

Table 9: ΔK_{th} Values from the best linear fit of $log(da/dN)$ $vs.$ $log(\Delta K)$ data for the girth weld material results of the two methodologies.

Methodology	Specimens	$\Delta K_{th,\text{ASTM}}$ (MPa.m$^{1/2}$)	R^2
ASTM E647	CP02	5,9	0,98
	CP03	4,4	0,98
	CP04	6,3	0,97
CPLR	CP06	8,8	0,97
	CP07	8,2	0,98
	CP08	8,9	0,98

As previously mentioned, upon analyzing the results in Table 9, it can be stated that the most conservative outcomes for the threshold value (ΔK_{th}) were achieved using the load reduction methodology (decreasing K) proposed by the ASTM E647 standard, in comparison to the CPLR methodology.

As is well known, a common procedure for relieving stresses in welds is the annealing heat treatment, which was applied to four specimens to carry out both methodologies and assess if better results could be obtained. Figure 79 presents the results for the methodology using ASTM E647 under the same conditions, including SE(B) geometry, R = 0.5 and S/W = 8, making a comparison with the results obtained without heat treatment.

The Figure 80 provides a comparison between the results using the CPLR methodology with and without heat treatment. The comparison provides a clear understanding of how this thermal process influences the fatigue behavior of the specimens, particularly in the context of machining.
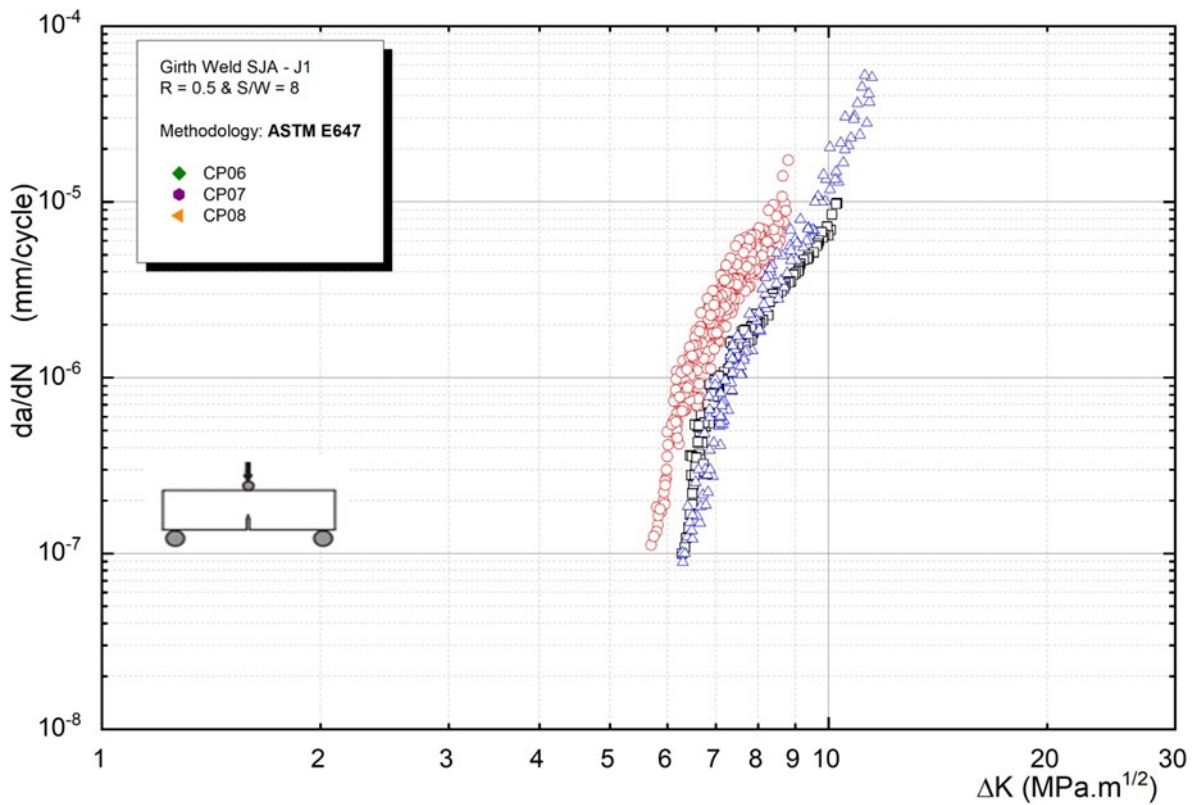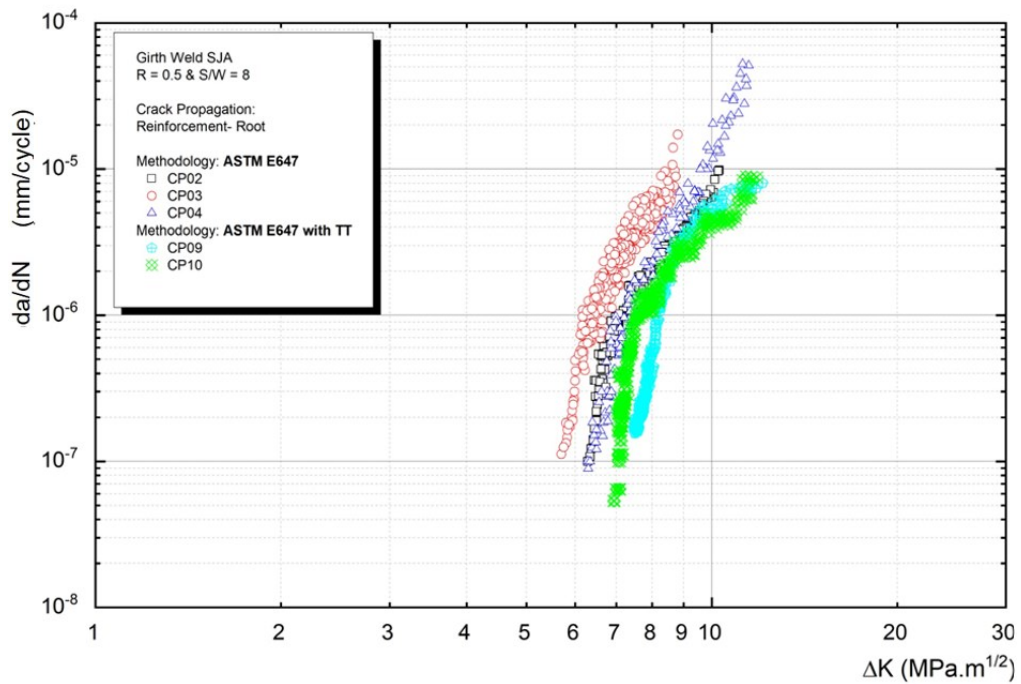
Figure 79: Results of fatigue crack propagation tests in the Region I of the *da/dN vs. ΔK* curve for SE(B) geometry, *S/W* = 8, R = 0.5 and ASTM E647 methodology. The tests were conducted on specimens with and without stress relief heat treatment.
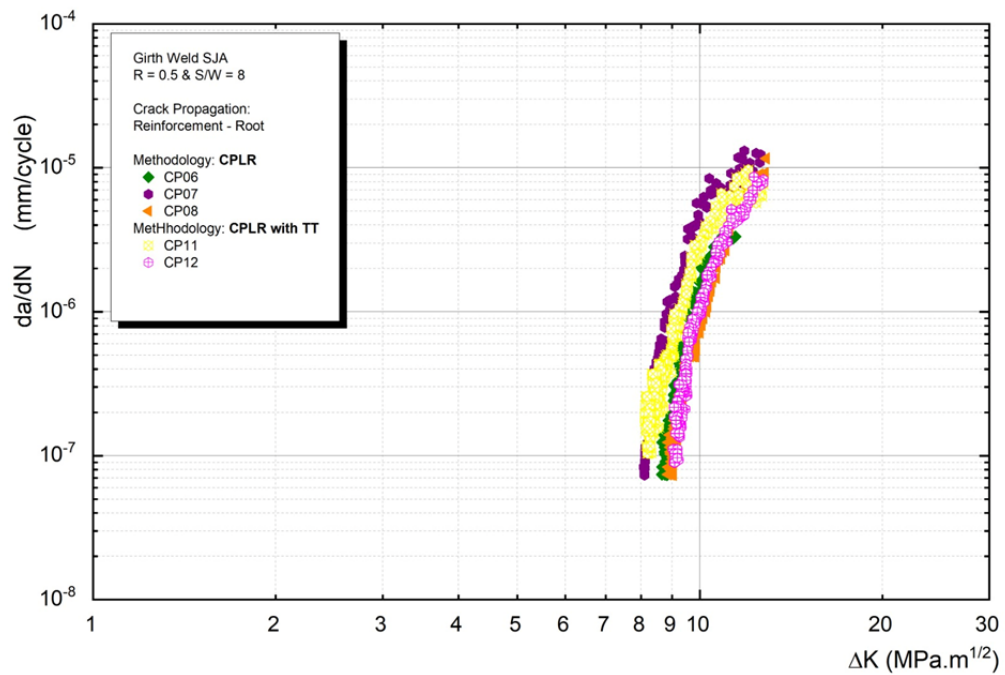
Figure 80: Results of fatigue crack propagation tests in the Region I of the *da/dN vs. ΔK* curve for SE(B) geometry, *S/W* = 8, R = 0.5 and CPLR methodology. The tests were conducted on specimens with and without stress relief heat treatment.

Analyzing Figure 79 and 80 allows us to conclude that, regardless of the analyzed condition (with or without heat treatment), the ASTM E647 methodology proves to be more conservative when compared to the CPLR technique. This is evident as it shows lower threshold values.

In Figures 81 (a-d), the fracture features of SE(B) specimens are evident after the fatigue crack propagation test, utilizing both methodologies and considering the two analyzed conditions. As depicted in Figures 81 (c-d), the four-point bending pre-compression technique proved effective, with load values adjusted to induce a pre-crack that naturally arrests after 2×10^6 cycles. Following the fatigue pre-compression of the specimens, the crack propagation region is discernible for determining the threshold. It is crucial to emphasize once more that fatigue crack propagation occurred within a dissimilar welded region, characterized by significant variations in microstructural features. The final phase is the fracture, wherein all specimens underwent breakage in liquid nitrogen.
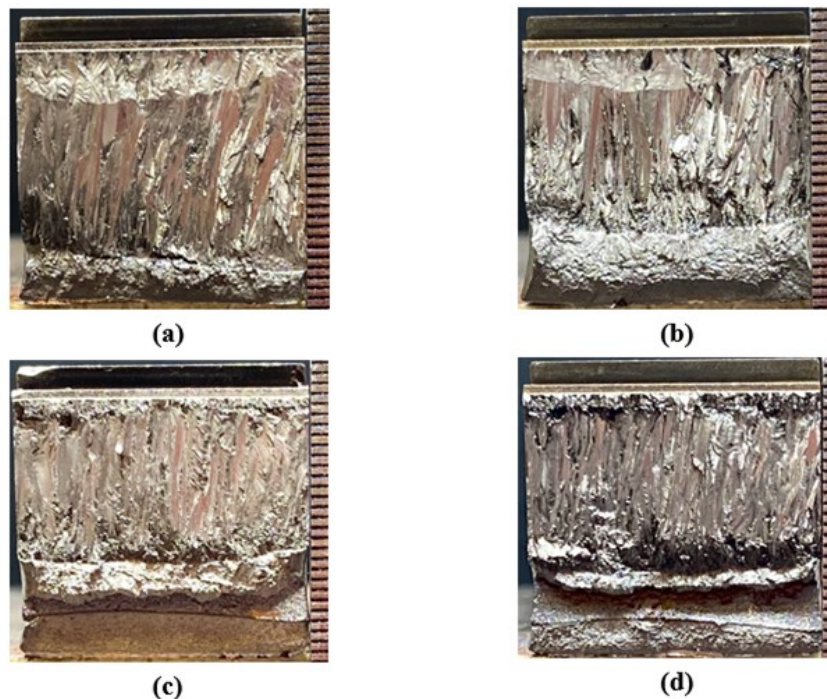
Figure 81: Fracture surface appearance for SE(B) specimens, with S/W = 8 and R = 0.5 of the Girth Weld (a) ASTM E647 – machined (CP03), b) ASTM E647 – after heat treatment (CP10), c) CPLR – machined (CP07) and d) CPLR – after heat treatment (CP12).

To assess the fracture surface of the samples shown in Figure 68, the same scheme as in Figure 66 was employed, illustrating how the analyses were conducted using

scanning electron microscopy (SEM) for each fracture region. It is important to note that the regions analyzed in the welded joint follow the same legend as reported for the AISI 316L material.

Therefore, Figures 82 to 85 sequentially present SEM images for the SE(B) specimens of the welded joint under the following conditions:

- CP03 – ASTM E647 Procedure – S/W = 8 and R = 0.5;
- CP07 – CPLR Procedure – S/W = 8 and R = 0.5;
- CP10 – ASTM E647 Procedure with Heat Treatment – S/W = 8 and R = 0.5;
- CP12 – ASTM E647 Procedure with Heat Treatment – S/W = 8 and R = 0.5.
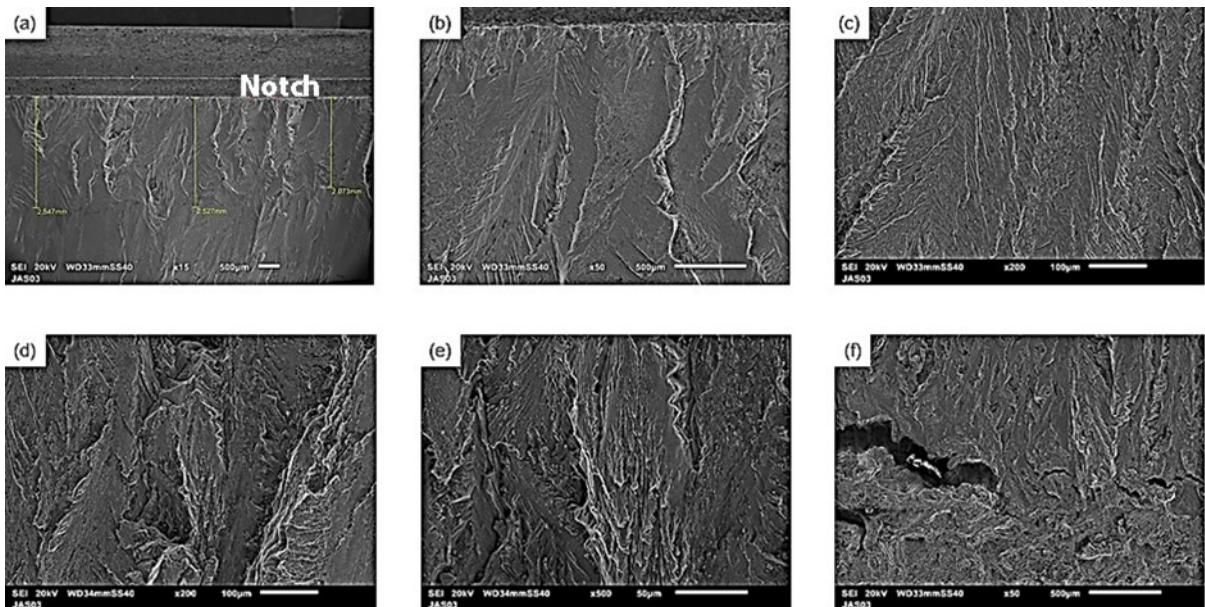
Figure 82: SEM images, at various magnifications, of the fracture surface of sample CP03: ASTM E647 – S/W = 8 and R = 0.5.
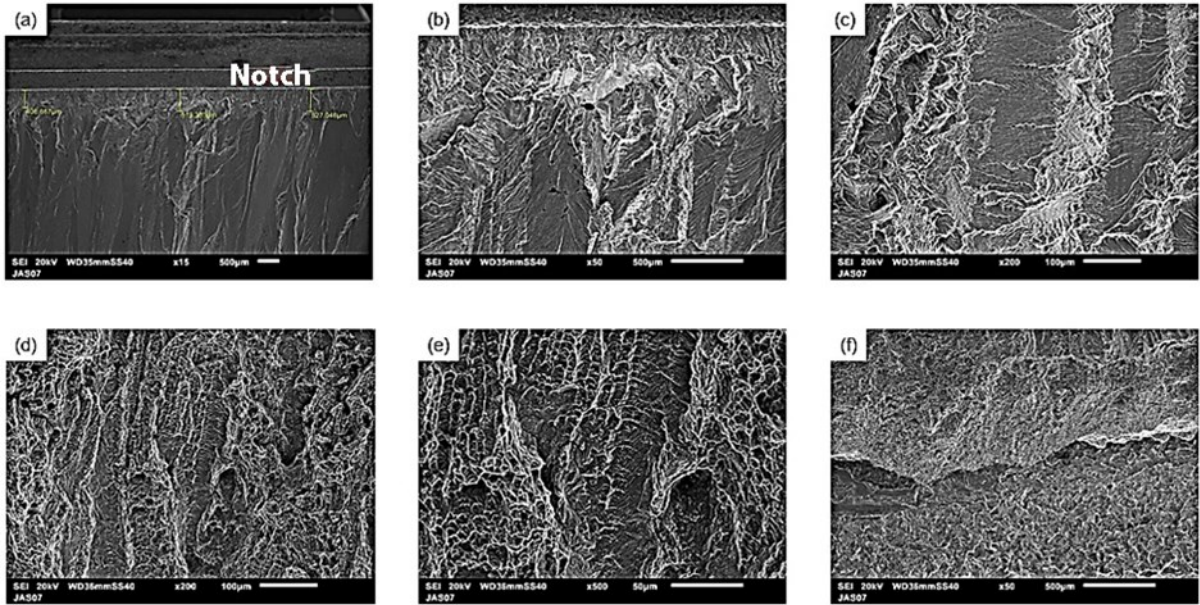
Figure 83: SEM images, at various magnifications, of the fracture surface of sample CP07: CPLR – S/W = 8 and R = 0.5.
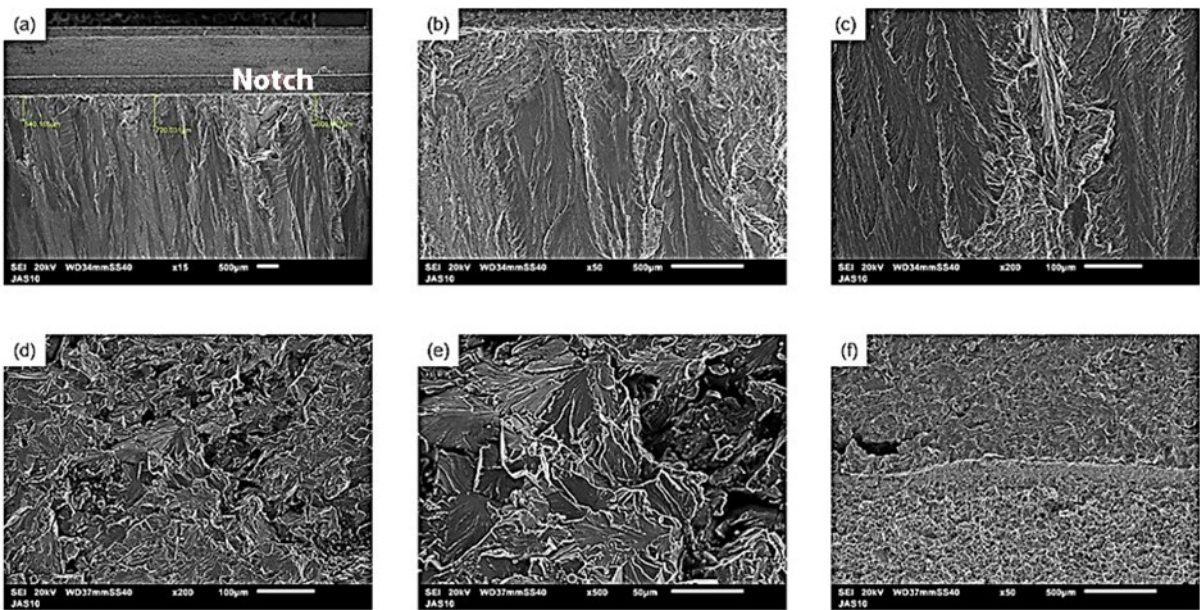
Figure 84: SEM images, at various magnifications, of the fracture surface of sample CP10: ASTM E647 with stress relief heat treatment – S/W = 8 and R = 0.5.
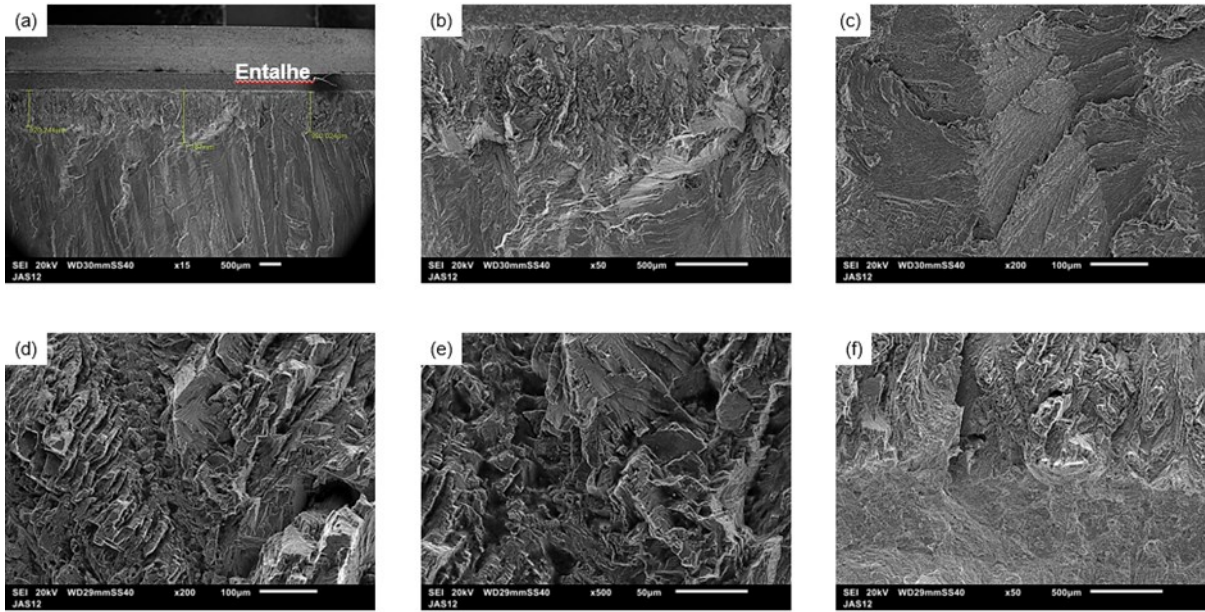
Figure 85: SEM images, at various magnifications, of the fracture surface of sample CP12: CPLR with stress relief heat treatment – S/W = 8 and R = 0.5.

CHAPTER 6

6. SUMMARY AND CONCLUSION

6.1. Summary and conclusion

6.2. AISI 316L Stainless Steel

Extensive fatigue crack growth testing on the AISI 316L austenitic stainless steel demonstrated that compression precracking methods affect threshold (ΔK_{th}) measurements, especially with interaction between specimen geometry and load ratio (R). Key conclusions include:

1. Standard C(T) specimens provided consistent near-threshold crack growth data for all R-ratios and precrack methods. CPLR compression generated lower ΔK_{th} values than ASTM E647 load reduction, primarily at low R=0.1. The CPCA technique was generally ineffective using C(T) samples.

2. Small SE(B) bending specimens exhibited pronounced geometry dependence for near-threshold crack growth rates at R=0.1 and standard S/W=4 span, likely due to substantial crack tip plasticity relative to uncracked ligament which corrupts measurements. Increasing span to non-standard S/W=8 improved behavior.

3. Compression precracking more prominently impacts near-threshold fatigue crack growth at low R=0.1 versus higher R=0.5 for the 316L stainless steel.

4. While material constraints often mandate small SE(B) specimens for circumferential pipeline girth welds, using increased span with higher R-ratios enables accurate near-threshold determination.

5. Considering complexity, CPC provides only marginal ΔK_{th} reductions over ASTM E647 load reduction for 316L, making standardized approaches likely preferable.

6.3. INCONEL 625 Girth Weld

Dissimilar to observations for homogeneous 316L stainless steel under analogous testing conditions, the CPLR compression precracking technique conferred no fatigue crack growth threshold (ΔK_{th}) benefit over ASTM E647 standard K-reduction for the API 5L Grade X65 pipe girth weld examined. Employing small SE(B) specimens (14 mm. width, R=0.5, S/W=8) without and with 350°C 2-hour stress relief, the innate microstructural and mechanical variation across the pipe-weld interface likely

supersedes any residual stress relief from compression in governing crack propagation resistance.

Given the specific V-groove parameters, thermal cycles, filler deposits and number of weld passes characterized, together with the specimen dimensions and loading rates examined, the ASTM E647 methodology delivered more conservative (lower) fatigue resistance estimates. Thus, for standardized dissimilar metal circumferential weld testing, the complexity of compression precracking is presently unjustified.

6.4. Future Works

While this study establishes fatigue crack growth data using compression-based load reduction on a dissimilar metal girth weld, ample potential exists to expand understanding of how compressive crack opening mitigates closure phenomena. Microscale crack tip plasticity should be quantified through focused meshing and simulation of the complex stress fields arising at the API 5L X65 weld interface. Obtaining the as-welded residual stress state via contour methods or neutral diffraction would enable validating closure predictions and identifying prime locations for compressive augmentation.

Systematic application of the optimized CPLR approach by situating small SE(B) specimens at the critical triple point offers an efficient means of capturing microstructure-sensitive crack growth resistance. Low load ratio testing may accentuate the dwell crack growth susceptibility. Fractographic examination provides microstructure-level validation. If properties ultimately prove suitable, demonstrating full-scale transferability would further enable this methodology to underpin fitness-for-service and remnant life assessments over widespread moderate-toughness steal pipeline girth welds.

7. REFERENCES

[1]   I. Lotsberg, *Fatigue design of marine structures*. New York NY: Cambridge University Press, 2016.

[2]   ASTM International, "ASTM E647-15 - Standard Test Method for Measurement of Fatigue Crack Growth Rates," *ASTM Book of Standards*, vol. 03, no. July, pp. 1–49, 2016, doi: 10.1520/E0647-15E01.2.

[3]   H. K.-I. J. of P. V. and Piping and undefined 1976, "A review of factors affecting toughness in welded steels," *Elsevier*, Accessed: Feb. 20, 2022. [Online].

[4]   American Welding Society, *American Welding Society, Welding Handbook: Welding Technology,* 8th Editio., vol. 1, no. 57. Miami: 1987, 2002.

[5]   S. R. Lampman, "ASM Handbook: Volume 19, Fatigue and Fracture," *ASM International*, vol. 19, no. 9, pp. 557–565, 1996.

[6]   H. O. F. Ralph I. Stephens, Ali Fatemi, Robert R. Stephens, *Metal Fatigue in Engineering, 2nd Edition*. Wiley, 2000.

[7]   S. Suresh, *Fatigue of materials*. 1998. Accessed: Feb. 20, 2022. [Online].

[8]   N. E. Dowling, *Mechanical behavior of materials : engineering methods for deformation, fracture, and fatigue*. Prentice Hall, 1999.

[9]   T. L. Anderson, *Fracture Mechanics: Fundaments and Applications*, 3rd ed. Boca Raton: CRC PRESS, 2005.

[10]   "Clad pipes." Accessed: Nov. 13, 2023. [Online]. Available: https://www.butting.com/en/clad-pipes

[11]   L. Smith, "Engineering with Clad Steel Engineering with CLAD STEEL Engineering with CLAD STEEL 2nd Edition," 2012.

[12]   "OTC 2012: Subsea 7 delivers innovative riser buoy support for Petrobras project | Offshore." Accessed: Mar. 13, 2024. [Online].

[13]   "DNV-ST-F101 Submarine pipeline systems - DNV." Accessed: Nov. 13, 2023. [Online].

[14]   A. Hilberink, "Mechanical Behaviour of Lined Pipe." 2011. Accessed: Nov. 13, 2023. [Online].

[15]   G. Heigl, V. Pavlyk, I. Aretov, and S. McCann, "A new method of producing mechanically lined pipe including large diameters," *OTC Brasil 2015: The Atlantic: From East to West - An Ocean of Innovation*, pp. 349–358, 2015, doi: 10.4043/26100-MS.

[16] J. F. Sathler, "AVALIAÇÃO DO COMPORTAMENTO MECÂNICO DE TUBOS DE PRFV COM DIFERENTES ENVELHECIMENTOS À DIFERENTES TAXAS DE DEFORMAÇÃO," 2017.

[17] S. P, C. ME, P. M, and Cladtek, "Mechanically Lined Pipe MLP with Improved Fatigue Resistance," *Offshore Technhology Conference*, 2019.

[18] T. Tkaczyk and A. Pépin TechnipFMC, "PROPOSED RECOMMENDED PRACTICE FOR ECA OF TRIPLE-POINT FLAWS IN MECHANICALLY LINED PIPES PAPER NUMBER: 34."

[19] M. D. Sangid, "The physics of fatigue crack initiation," *Int J Fatigue*, vol. 57, pp. 58–72, 2013, doi: 10.1016/j.ijfatigue.2012.10.009.

[20] Y. Khin and W. Beng, "A PHENOMENOLOGICAL AND MECHANISTIC STUDY OF FATIGUE UNDER COMPLEX LOADING HISTORIES," 2003.

[21] W. Schlitz, "A HISTORY OF FATIGUEt," ~ *Pergamon Engineering Fracture Mechanics*, vol. 54, no. 2, pp. 263–300, 1996.

[22] D. J. Wulpi, "Understanding How Components Fail," Nov. 2013, doi: 10.31399/ASM.TB.UHCF3.9781627082709.

[23] W. D. Callister and D. G. Rethwisch, "Materials science and engineering : an introduction", Accessed: Nov. 20, 2023. [Online].

[24] T. S. Sudarshan, T. S. Srivatsan, and D. P. Harvey, "Fatigue processes in metals—role of aqueous environments," *Eng Fract Mech*, vol. 36, no. 6, pp. 827–852, Jan. 1990, doi: 10.1016/0013-7944(90)90262-F.

[25] G. Ellwood. Dieter and D. J. Bacon, "Mechanical metallurgy," p. 751, 1988.

[26] T. V. Duggan and J. Byrne, "Fatigue as a design criterion," *Fatigue as a Design Criterion*, 1977, doi: 10.1007/978-1-349-03222-8.

[27] "Fatigue Physics - Metal Fatigue Life Prediction." Accessed: Mar. 13, 2024. [Online]. Available: https://fatigue-life.com/fatigue-physics/

[28] J. Barsom, "Fatigue-crack propagation in steels of various yield strengths," 1971, Accessed: Feb. 28, 2022. [Online].

[29] "ASM Handbook ," 2008, Accessed: Nov. 20, 2023. [Online]. Available: https://www.asminternational.org/books-and-handbooks/results/-/journal_content/56/10192/05115G/PUBLICATION/

[30] J. A. G. Plata, L. H. C. Bonazzi, D. F. B. Sarzosa, and C. Ruggieri, "Effect of compression precracking on the near threshold fatigue crack propagation in an AISI 316L stainless steel," *Int J Fatigue*, vol. 170, p. 107553, 2023, doi: 10.1016/j.ijfatigue.2023.107553.

[31]   B. Craig, L. S.-N. I. T. Series, and undefined 2011, "Corrosion Resistant Alloys (CRAs) in the oil and gas industry," *nickelinstitute.orgBD Craig, L SmithNickel Institute Technical Series, 2011•nickelinstitute.org*, 2011, Accessed: Nov. 20, 2023. [Online].

[32]   T. A. D. ANM-115, "Damage tolerance and fatigue evaluation of structure," *Federal Aviation Regulations*, 2011, [Online].

[33]   W. Elber, "FATIGUE CRACK CLOSURE UNDER CYCLIC TENSION".

[34]   K. H, K. N, S. JAK, H. K, and Y. T., "Fatigue crack extension in four-point bending test for steels imitated heat affected zone," *J Soc Mater Sci, Jpn*, vol. 64, no. 4, pp. 323–9, 2015.

[35]   A. Hadrboletz, B. Weiss, and R. Stickler, "'The Significance of the Fatigue Threshold for Metallic Materials' Localized Damage IV," *Computational Mechanics Publications, Southampton*, 1996.

[36]   J. Schijve, "Fatigue crack closure, observations and technical significance," *American Society for Testing and Materials*, vol. 982, pp. 5–34, 1986, [Online].

[37]   D. F. Sarzosa Burgos, "Avaliação da vida à fadiga em materiais homogêneos e juntas soldadas incluindo efeitos de fechamento de trinca.," Apr. 2013, doi: 10.11606/T.3.2012.TDE-04062013-153636.

[38]   "E399 Standard Test Method for Linear-Elastic Plane-Strain Fracture Toughness of Metallic Materials." Accessed: May 20, 2024. [Online].

[39]   ASTM, "ASTM E1820-17 Standard Test Method for Measurement of Fracture Toughness 1", doi: 10.1520/E1820-17.

[40]   E. M. Rodrigues, A. Matias, L. B. Godefroid, F. L. Bastian, and K. S. Al-Rubaie, "Fatigue crack growth resistance and crack closure behavior in two aluminum alloys for aeronautical applications," *Materials Research*, vol. 8, no. 3, pp. 287–291, 2005, doi: 10.1590/S1516-14392005000300011.

[41]   P. Chowdhury and H. Sehitoglu, "Mechanisms of fatigue crack growth – a critical digest of theoretical developments," pp. 1–23, 2016, doi: 10.1111/ffe.12392.

[42]   D. Davidson, K. Chan, R. McClung, and S. Hudak, "4.05 - Small Fatigue Cracks," *Comprehensive Structural Integrity: Nine Volume Set*, vol. 1–9, pp. 129–164, Jan. 2003, doi: 10.1016/B0-08-043749-4/04073-8.

[43]   S. Hamada, T. Kinoshita, K. Morishige, K. Hayashi, T. Ishina, and H. Noguchi, "Engineering definitions of small crack and long crack at fatigue limit under tensile mean stress and a prediction method for determining the fatigue limit of a cracked Mg alloy," *Int J Fatigue*, vol. 56, pp. 86–94, 2013, doi: 10.1016/J.IJFATIGUE.2013.08.006.

[44] K. Obrtlík, J. Polák, M. Hájek, and A. Vašek, "Short fatigue crack behaviour in 316L stainless steel," *Int J Fatigue*, vol. 19, no. 6, pp. 471–475, Aug. 1997, doi: 10.1016/S0142-1123(97)00005-4.

[45] R. O. Ritchie and J. O. Peters, "Small Fatigue Cracks: Mechanics, Mechanisms and Engineering Applications," *Mater Trans*, vol. 42, no. 1, pp. 58–67, 2001, doi: 10.2320/MATERTRANS.42.58.

[46] A. de Pannemaecker, S. Fouvry, J. Y. Buffiere, and M. Brochu, "Modelling the fretting fatigue crack growth: From short crack correction strategies to microstructural approaches," *Int J Fatigue*, vol. 117, pp. 75–89, Dec. 2018, doi: 10.1016/J.IJFATIGUE.2018.07.034.

[47] K. Sadananda, M. Nani Babu, and A. K. Vasudevan, "A review of fatigue crack growth resistance in the short crack growth regime," *Materials Science and Engineering: A*, vol. 754, pp. 674–701, Apr. 2019, doi: 10.1016/J.MSEA.2019.03.102.

[48] M. Janssen, J. Zuidema, and R. Wanhill, "Fracture Mechanics : Fundamentals and Applications," Aug. 2004, doi: 10.1201/9781482265583.

[49] J. C. Newman and Y. Yamada, "Compression precracking methods to generate near-threshold fatigue-crack-growth-rate data," *Int J Fatigue*, vol. 32, no. 6, pp. 879–885, 2010, doi: 10.1016/j.ijfatigue.2009.02.030.

[50] R. P. Hubbard, "Crack Growth Under Cyclic Compression," *J. Basic Eng.*, pp. 625–630, 1969.

[51] Topper TH, Au P., A. G. F. O. R. A. Research, and D. N.-S.-S. (France), "Fatigue Test Methodology.," no. 118, 1981, Accessed: Mar. 01, 2022. [Online].

[52] P. L. R, K. F, and S. HP, "The use of fatigue specimens precracked in compression for measuring threshold values and crack growt," *ASTM J*, no. Test Eval, pp. 22–98, 1994.

[53] R. Pippan, "THE GROWTH OF SHORT CRACKS UNDER CYCLIC COMPRESSION," *Fatigue Fract Eng Mater Struct*, vol. 9, no. 5, pp. 319–328, May 1987, doi: 10.1111/J.1460-2695.1987.TB00459.X.

[54] S. C. Forth, J. C. Newman, and R. G. Forman, "On Generating Fatigue Crack Growth Thresholds Article in International Journal of Fatigue · February," *Int J Fatigue*, vol. 25, pp. 9–15, 2003, doi: 10.1016/S0142-1123(02)00066-X.

[55] J. C. Newman, "An Evaluation of the Plasticity-Induced Crack-Closure Concept and Measurement Methods," 1998.

[56] M. Carbonni, L. Patriarca, and D. Regazzi, "Determination of △Kth by compression pre-cracking in a structural steel," *J ASTM Int*, vol. 6, no. 9, Oct. 2009, doi: 10.1520/JAI102617.

[57] "ISO 12108:2012 - Metallic materials — Fatigue testing — Fatigue crack growth method." Accessed: Dec. 04, 2023. [Online]. Available: https://www.iso.org/standard/42815.html

[58] K. Minakawa and A. J. McEvily, "On crack closure in the near-threshold region," *Scripta Metallurgica*, vol. 15, no. 6, pp. 633–636, Jun. 1981, doi: 10.1016/0036-9748(81)90041-7.

[59] A. Ohta, E. Sasaki, M. Nihei, M. Kosuge, M. Kanao, and M. Inagaki, "Fatigue crack propagation rates and threshold stress intensity factors for welded joints of HT80 steel at several stress ratios," *Int J Fatigue*, vol. 4, no. 4, pp. 233–237, Oct. 1982, doi: 10.1016/0142-1123(82)90006-8.

[60] R. Pippan and A. Hohenwarter, "Fatigue crack closure: a review of the physical phenomena," *Fatigue Fract Eng Mater Struct*, vol. 40, no. 4, pp. 471–495, Apr. 2017, doi: 10.1111/FFE.12578.

[61] A. J. McEvily and R. O. Ritchie, "Crack closure and the fatigue-crack propagation threshold as a function of load ratio," *Fatigue Fract Eng Mater Struct*, vol. 21, no. 7, pp. 847–855, 1998, doi: 10.1046/J.1460-2695.1998.00069.X.

[62] H. Saeed, S. Chaudhuri, and W. De Waele, "Calibration and validation of extended back-face strain compliance for a wide range of crack lengths in SENB-4P specimens," *Procedia Structural Integrity*, vol. 42, pp. 967–976, Jan. 2022, doi: 10.1016/J.PROSTR.2022.12.122.

[63] V. S. Barbosa and C. Ruggieri, "Fracture toughness testing using non-standard bend specimens – Part I: Constraint effects and development of test procedure," *Eng Fract Mech*, vol. 195, pp. 279–296, May 2018, doi: 10.1016/j.engfracmech.2018.03.029.

[64] L. Grabowski and J. R. Yates, "The effect of specimen geometry on short-crack growth behaviour of a nickel-based superalloy," *Int J Fatigue*, vol. 14, no. 4, pp. 227–232, 1992, doi: 10.1016/0142-1123(92)90005-W.

[65] J. R. Yates, W. Zhang, and K. J. Miller, "THE INITIATION AND PROPAGATION BEHAVIOUR OF SHORT FATIGUE CRACKS IN WASPALOY SUBJECTED TO BENDING," *Fatigue Fract Eng Mater Struct*, vol. 16, no. 3, pp. 351–362, Mar. 1993, doi: 10.1111/J.1460-2695.1993.TB00092.X.

[66] J. P. Campbell and R. O. Ritchie, "Mixed-mode, high-cycle fatigue-crack growth thresholds in Ti–6Al–4V: I. A comparison of large- and short-crack behavior," *Eng Fract Mech*, vol. 67, no. 3, pp. 209–227, Oct. 2000, doi: 10.1016/S0013-7944(00)00046-1.

[67] W. Villarroel, "Designation: A 240/A 240M -04a e1 Standard Specification for Chromium and Chromium-Nickel Stainless Steel Plate, Sheet, and Strip for

Pressure Vessels and for General Applications 1," *ASTM-A240*, Jan. 2004, Accessed: Dec. 04, 2023. [Online].

[68]   American Society for Testing and Materials., "E8 Standard Test Methods for Tension Testing of Metallic Materials. ASTM E8/8M.," ASTM International. Accessed: Dec. 04, 2023. [Online].

[69]   T. L. Anderson and D. A. Osage, "API 579: a comprehensive fitness-for-service guide," *International Journal of Pressure Vessels and Piping*, vol. 77, no. 14–15, pp. 953–963, Dec. 2000, doi: 10.1016/S0308-0161(01)00018-7.

[70]   V. S. Barbosa and C. Ruggieri, "Fracture toughness testing using non-standard bend specimens – Part II: Experiments and evaluation of reference temperature for a low alloy structural steel," *Eng Fract Mech*, vol. 195, pp. 297–312, May 2018, doi: 10.1016/j.engfracmech.2018.03.028.

[71]   Alloy Plate, Sheet, and Strip., "American Society for Testing and Materials. Standard Specification for Nickel-Chromium-Molybdenum-Columbium Alloy and Nickel-Chromium-Molybdenum-Silicon. ASTM B443," *M International.*, vol. ASTM B443, no. Alloy Plate, Sheet, and Strip, 2019, doi: 10.1520/B0443.

[72]   American Society for Testing and Materials., "Sandard Specification for Nickel-Chromium-Molybdenum-Columbium Alloys (UNS N06625 and UNS N06852) and Nickel- Chromium-Molybdenum-Silicon Alloy (UNS N06219) Pipe and Tube. ASTM B444," *ASTM International*, 2018, Accessed: Jan. 02, 2024. [Online]. Available: www.astm.org,

[73]   D. L. Chen, B. Weiss, and R. Stickler, "Effect of stress ratio and loading condition on the fatigue threshold," *Int J Fatigue*, vol. 14, no. 5, pp. 325–329, Sep. 1992, doi: 10.1016/0142-1123(92)90484-T.

[74]   Z. Xiaopeng, "The effects of stress ratio on fatigue threshold," *Int J Fatigue*, vol. 12, no. 2, pp. 127–130, Mar. 1990, doi: 10.1016/0142-1123(90)90683-6.

[75]   O. Vosikovsky, "The effect of stress ratio on fatigue crack growth rates in steels," *Eng Fract Mech*, vol. 11, no. 3, pp. 595–602, Jan. 1979, doi: 10.1016/0013-7944(79)90083-3.

[76]   L. L. S. Mathias, D. F. B. Sarzosa, and C. Ruggieri, "Effects of specimen geometry and loading mode on crack growth resistance curves of a high-strength pipeline girth weld," *International Journal of Pressure Vessels and Piping*, vol. Complete, no. 111–112, pp. 106–119, Nov. 2013, doi: 10.1016/J.IJPVP.2013.06.003.

[77]   Dassault Systèmes Simulia Corp, "ABAQUS Standard ." Providence, RI, USA, 2012.

[78]   J. M. , Gere and B. J. Goodno, *Mechanics of materials. .* Cengage learning., 2012.

[79] R. C. Jr and E. Taleff, "Mechanics of materials," 2020, Accessed: Jan. 18, 2024. [Online].

APPENDIX

Appendix A *Compression Precracking Load for the 4P Bend Specimen*

This section describes the evaluation procedure to determine the compression precracking load that was applied in the fatigue threshold tests of the bend specimen using a four-point bend scheme, as previously outlined in Section 3.2. First, the cyclic stress-strain behavior of the AISI 316L material used in the fatigue tests was experimentally measured by testing a standard tensile specimens with 12.5 mm diameter extracted from the longitudinal plate direction at room temperature (T = 20°C). The tensile specimen is subjected to repeated blocks of incrementally increasing and decreasing strains as shown in Figure 86 (a). The test is conducted under strain control with a rate of 0.001 (mm/mm)/sec. The stable hysteresis loops are measured after applying of 20 blocks of loading, see Figure 86 (b).

(a) (b)
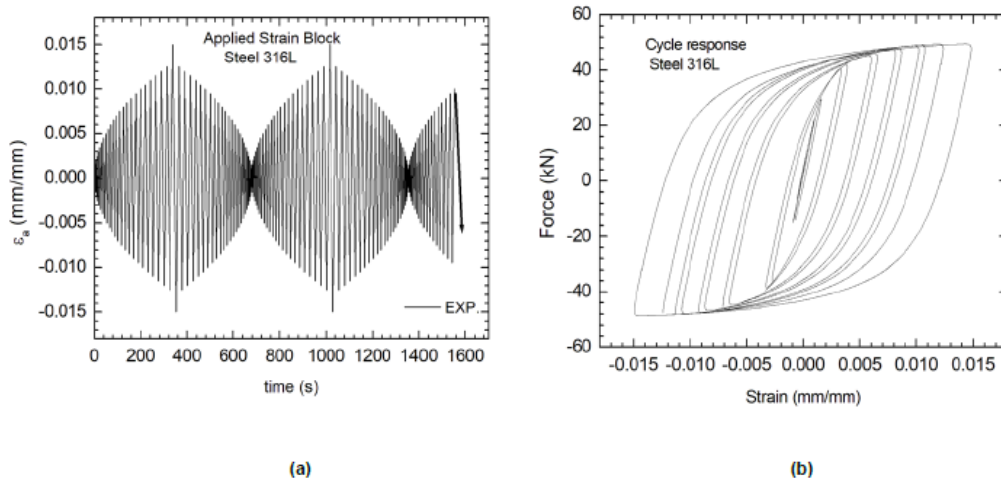
Figure 86: Experimental procedure to evaluate the cyclic stress–strain behavior of the AISI 316L material used in the fatigue tests: (a) Strain blocks used in the incremental step-test method. (b) Stable measured force versus applied strain at the last applied block

The finite element code ABAQUS [77] is employed to calibrate the kinematic hardening law and, thus, to obtain a more accurate numerical description of the cyclic response. The non-linear kinematic hardening rule is modeled by

$$\alpha = \frac{C}{\gamma}(1 - e^{-\gamma \varepsilon_p}) \quad (7)$$

where α is the backstress tensor defining the position of the center of the yield surface, ε_p defines the equivalent plastic strain, C and $\gamma$ are material constants that must be calibrated from cyclic data, respectively. The stable stress-strain hysteresis at a strain amplitude of ε_α = 0.01 was used to calibrate the numerical analysis. To improve the simulation of the hysteresis loops, three decomposed hardening rules (α_k; k = 1;2;3) are used during the calibration process. Each rule is used to better fit the experimental response at the beginning, transient nonlinear portion and final linear response.

The calibrated parameters are reported in Table 10. Figure 87 (a, b) demonstrates the good agreement between the calibrated numerical results and the experimental response for different strain amplitudes, as characterized by ε_α = 0.01 and ε_α = 0.015.

Table 10: Kinematic material constants for the tested steel 316L.

k-th Backstress	C_k	γ_k
1	10919	112.3
2	38714	672.1
3	20815	3829.5
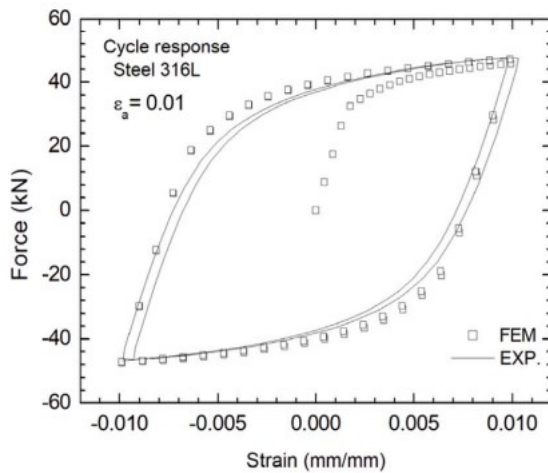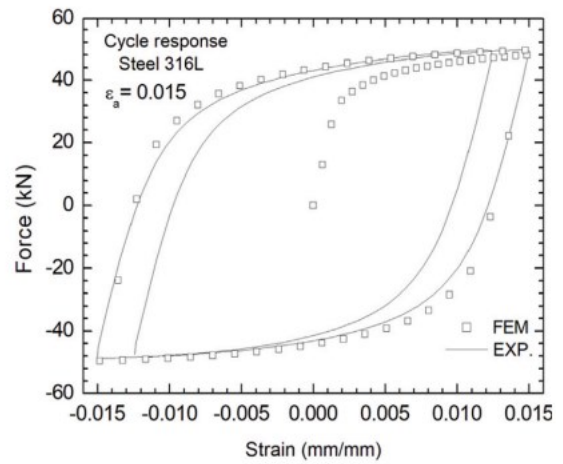
(a)   (b)

Figure 87: Comparison between experimental and numerical description of a stable force vs. strain cycle: (a) ε_α = 0.01. (b) ε_α = 0.015.

Figure 88: 3D finite element model of the SE(B) specimen under four-point bending employed to evaluate the compression precracking load.
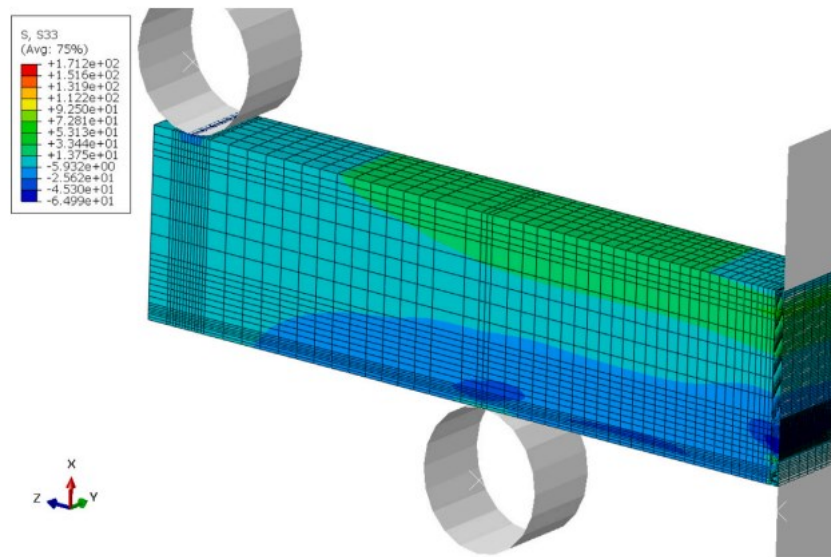
Numerical analyses were performed on 3-D models of the SE(B) fracture specimens shown previously in Figure 89 (b) under four-point bending. Due to symmetry, only one-quarter of the geometry is simulated by imposing appropriate constraints on the symmetry planes. Figure 88 shows the finite element model which consists of 41,816 nodes and 36,834 8-node (brick) elements arranged into 21 variable thickness layers defined over the half thickness (*B/2*) to accommodate strong *Y* variations in the stress distribution along the crack front (observe that the *Y* coordinate corresponds to the thickness direction in the numerical model, such that the opening normal stresses are in the Z-direction of the global system). To describe crack extension during cyclic loading, the finite element mesh ahead of crack tip and along the remaining crack ligament for this configuration contains a row of squared "cell" elements, each cell with planar size of 0.005 x 0.005 mm. The numerical model of the SE(B) specimen was subjected to a cyclic load between P_{min} = -12 kN and P_{max} = -1.2 kN. After two loading cycles, the constraints imposed on the crack plane nodes were released to allow the crack to grow by an amount of Δ_α = 0.05 mm. This process is repeated until the total crack extension reaches $\Delta_{\alpha total}$ = 0.4 mm.

Figure 89 (a, b) shows the distribution of residual stresses versus crack tip distance at the maximum load level, P_{max}, for the first cycle of loading and for increased amounts of crack growth.
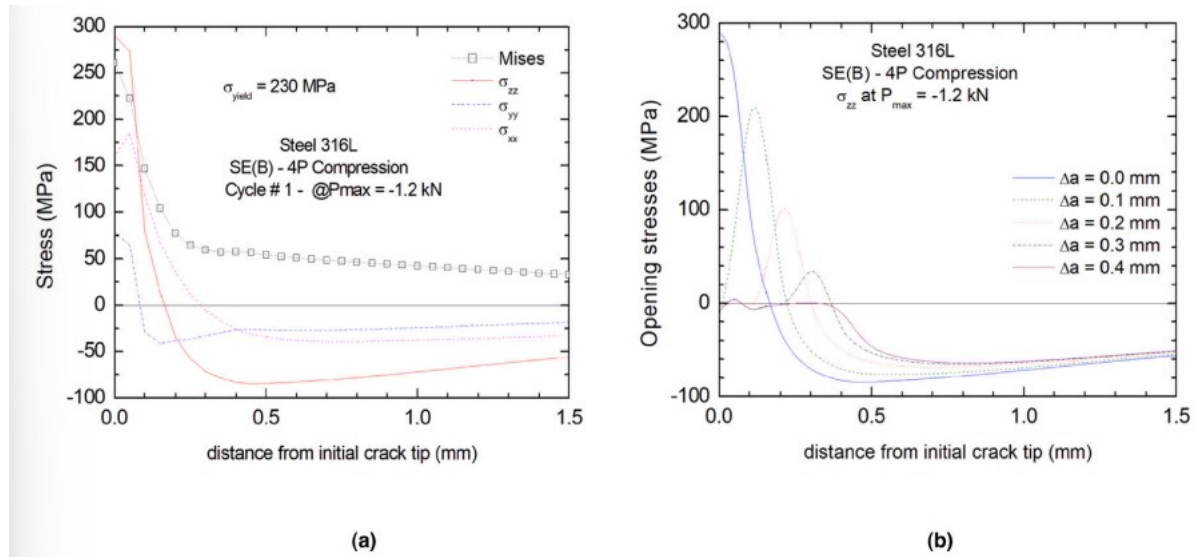
Figure 89: Comparison between experimental and numerical description of a stable force vs. strain cycle: (a) ε_α = 0.01. (b) ε_α = 0.015.

First, direct attention at the stress distribution ahead of crack tip for the first cycle of loading displayed in Figure 89 (a). As can be seen, even though both tensile and compressive residual stresses are present, a relatively strong tensile residual stress field at the end of the first cycle is dominant over a large portion ahead the crack tip. Here, the size of the tensile stress field is in the range of $\approx$ 0.1 ~ 0.2 mm, where the compressive stress field dominates over a much larger size ahead of crack tip. Now focus on the stress distribution with increased crack extension shown in Figure 89 (b).

As the crack propagates, the residual stresses are relaxed with peak values decreasing rapidly. After a crack extension of Δ_α = 0.4 mm, the numerical results reveal that there is no longer a tensile zone ahead of the crack tip, thereby indicating that the driving force is reduced as the crack propagates during the compression precracking test. At some point in the test, the crack naturally stops because there are no more tensile stresses ahead of the current crack tip. Thus, the selected loads, P_{min} = -12 kN and P_{max} = -1.2 kN, are considered the adequate values for conducting the compression precracking under four-point bending for the SE(B) specimens under consideration.

Appendix B Fracture toughness testing using non-standard bend specimens

Barbosa & Ruggieri's work addresses the development of a fracture toughness test procedure using standard and non-standard SE(B) specimens, including non-standard 4-point bend configurations. In the present study, extensive plane-strain finite element analyses are conducted on non-standard bend geometries with varying specimen span over width ratio (S/W) and loaded under 3-point and 4-point bending Figure 90(a, b).

Increasing the span-to-width ratio (S/W) from 4 to 8 for SE(B) bend specimens results in improved fracture toughness measurement for several reasons:

- Higher S/W ratios increase crack tip constraint levels. This mitigates undesirable constraint loss that can occur in smaller bend specimens, leading to more accurate toughness values.

- With more constraint, SE(B) specimens better replicate the high triaxiality conditions experienced by cracks in real structures. This makes the toughness measurement more relevant for fitness-for-service assessments.

- Due to reduced shear stresses from increased bending, there is less interaction between the crack tip plastic zone and global plasticity at higher S/W ratios. This minimizes artificial reductions in toughness.

- Larger bend specimens experience higher stretch zone demands prior to fracture. This provides a greater material sampling volume ahead of the crack front for cleavage processes.

- Statistical variations in microstructural flaws have less influence on fracture when a larger ligament is tested. Results are more representative of the material's true toughness.

- Specimens with S/W=8 exhibit toughness closer to standard 1T C(T) samples. This improves measurement consistency between specimen types.

In summary, increasing the S/W ratio reduces common artifacts that lead to unconservative toughness measurements in compact specimens. The higher constraint SE(B) geometry provides fracture data that is more intrinsic to the material and relevant for structural integrity assessments.

Another convenient bend test configuration, albeit not yet standardized in fracture toughness test procedures, which has gained increased interest is the 4-point bend geometry displayed in Figure 90 (b) in which D represents the inner span. Here, the flexural bend test fixture produces a uniform moment between the two inner loading rollers in the specimen (and associated zero shear stress) as can be easily verified by using simple beam flexure theory [78], [79]. To support standardization efforts for fracture toughness testing using this specimen geometry, the present analyses also cover specimen configurations in the range $4 \leqslant S/W \leqslant 8$.
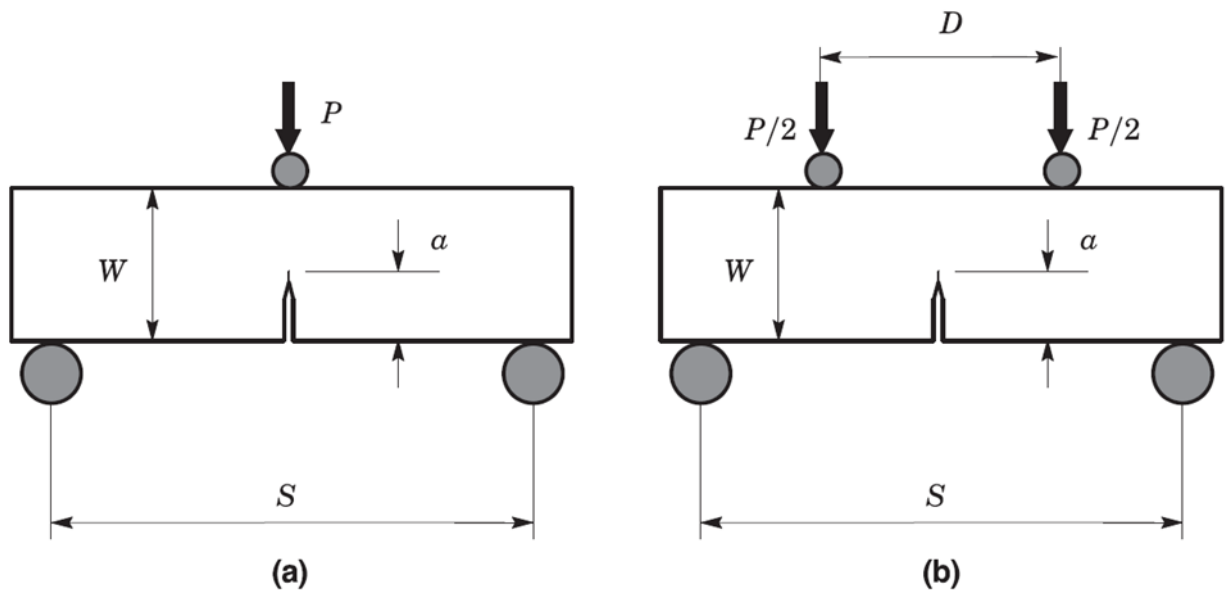

Figure 90: Conventional bending loading geometries adopted in the present work: (a) 3-point SE(B) specimen. (b) 4-point bend specimen.

Barbosa & Ruggieri investigated the impact of loading mode and specimen span on load carrying capacity, analyzing typical load-displacement curves. Notably, the results revealed a significant influence of specimen geometry and span size, with bend specimens featuring increased span demonstrating reduced applied load compared to standard counterparts. Furthermore, the role of loading mode appeared to play a lesser role in load carrying capacity for specific geometries. The evaluation of fracture toughness values (J_c) involved the use of η-solutions and results indicated that deeply-cracked SE(B) specimens exceeded specified deformation limits. In contrast, PCVN configurations showed lower M-values at fracture, with some values approaching the specified limit.
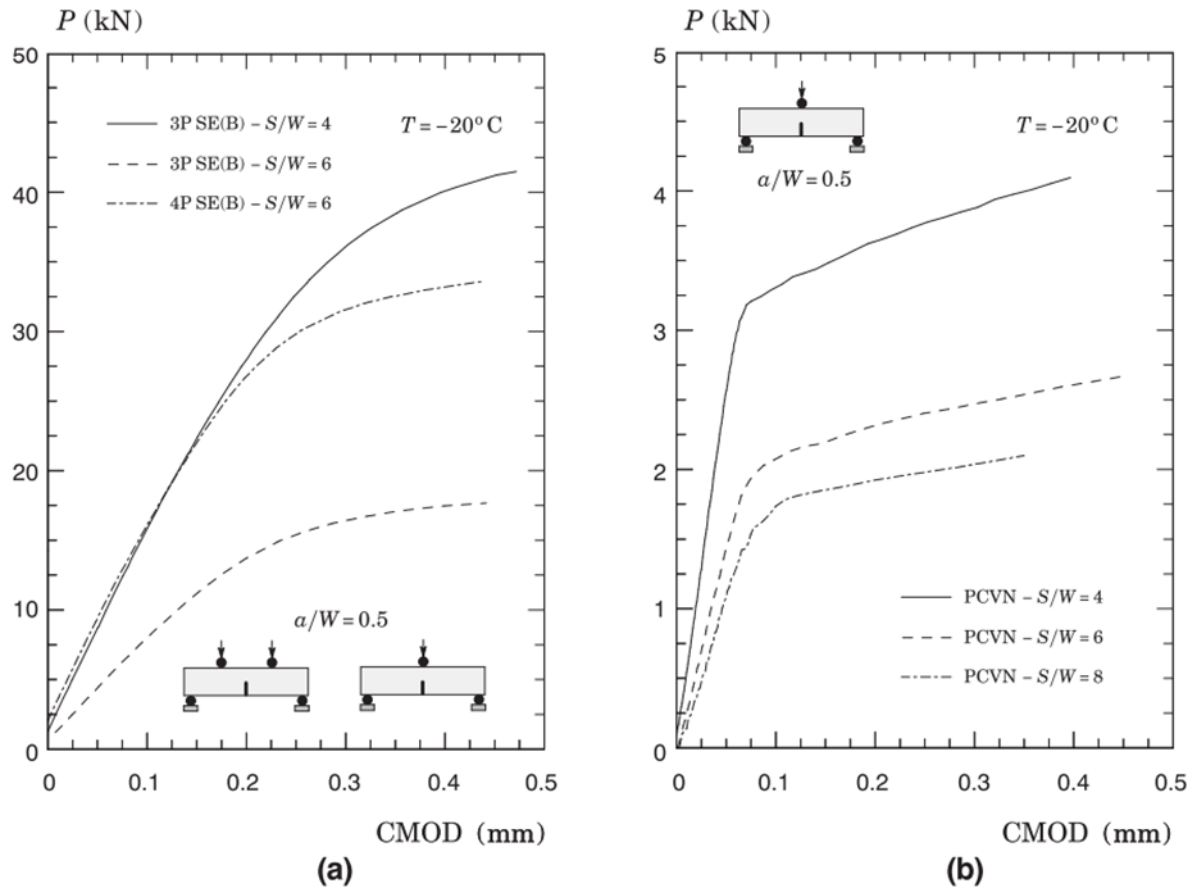
Figure 91: Representative load-displacement response for the tested geometries with varying specimen span: (a) 3-point and 4-point SE(B) specimens with a W/ 0. = 5. (b) PCVN configurations.

Notably, the examination of typical load-displacement curves (CMOD) in the Figure 91 revealed intriguing insights. The results emphasized the profound influence of specimen geometry and span size on the observed outcomes. Specifically, bend specimens with increased span exhibited a noteworthy reduction in applied load when compared to their standard counterparts (*S/W* = 4). Interestingly, it was found that loading mode played a relatively minor role in determining the load carrying capacity, particularly evident in the case of the 4P bend geometry with *S/W* = 6.